

CAUSES OF SOLAR ERUPTIONS: A COMPARATIVE STUDY OF
SUPER-ACTIVE AND LOW-ACTIVE ACTIVE REGIONS

by

Suman Dhakal
A Dissertation
Submitted to the
Graduate Faculty
of
George Mason University
In Partial fulfillment of
The Requirements for the Degree
of
Doctor of Philosophy
Physics

Committee:

_____ Dr. Jie Zhang, Committee Chair
_____ Dr. Nat Gopalswamy, Committee Member
_____ Dr. Robert Weigel, Committee Member
_____ Dr. Erdal Yiğit, Committee Member
_____ Dr. Paul So, Department Chairperson
_____ Dr. Donna M. Fox, Associate dean,
Office of Student Affairs & special
Programs, College of Science
_____ Dr. Fernando R. Miralles-Wilhelm, Dean,
College of Science

Date: _____ Fall Semester 2021
George Mason University
Fairfax, VA

Causes of Solar Eruptions: A Comparative Study of Super-Active and Low-Active Active
Regions

A dissertation submitted in partial fulfillment of the requirements for the degree of
Doctor of Philosophy at George Mason University

By

Suman Dhakal
Master of Science
Tribhuvan University, 2013
Bachelor of Science
Birendra Multiple Campus, 2007

Director: Dr. Jie Zhang, Professor
Department of Department of Physics and Astronomy

Fall Semester 2021
George Mason University
Fairfax, VA

Copyright © 2021 by Suman Dhakal
All Rights Reserved

Dedication

I dedicate this dissertation to my respectful parents, caring siblings, and beloved wife. They always encouraged and supported me in this journey. Without their constant support, this thesis paper was not possible.

Acknowledgments

I would like to thank the following people who made this possible. First and foremost I would like to thank my esteemed supervisor, Dr. Jie Zhang, for his motivation, continuous support, and patience. His guidance and insight have made this whole graduate experience possible. I would like to thank my dissertation committee: Dr. Nat Gopalswamy, Dr. Robert Weigel, and Dr. Erdal Yiğit for giving me their time and effort. Finally, I would like to express my deepest gratitude to my parents, wife, family and friends for their love, concern and encouragement. I could not have done without the support of my family, friends, and instructors.

Table of Contents

	Page
List of Tables	vii
List of Figures	ix
Abstract	xix
1 Introduction	1
1.1 Active Regions	2
1.1.1 Magnetic Origin of Active Regions	4
1.1.2 Evolution of Active Regions	6
1.2 Origin of Solar Eruptions	8
1.3 Topics Covered in the Thesis	11
1.3.1 What Determines the Flare Productivity of ARs	11
1.3.2 Successive Solar Eruptions From the Same Location	12
1.3.3 Origin of Compound Eruption	13
1.3.4 Outline of Dissertation	13
2 Data and Active Region Catalog	14
2.1 The Solar Dynamic Observatory	14
2.1.1 The Helioseismic and Magnetic Imager	15
2.1.2 The Atmospheric Imaging Assembly	19
2.2 Active Region Catalog	24
3 Evolutionary Differences between Super-Active and Low-Active Active Regions: A Statistical Analysis	31
3.1 Data and Methodology	33
3.2 Selection of ARs for Comparative Study	36
3.3 Differences between SAARs and LAARs	38
3.3.1 Evolution of AR with Small Sunspot Area and Low FI: AR 11430	39
3.3.2 Evolution of AR with Large Sunspot Area and Low FI: AR 12108	44
3.3.3 Evolution of AR with Large Sunspot Area and High FI: AR 11515	44
3.3.4 Evolution of AR with Small Sunspot area and High FI: AR 11928	49
3.4 Quantification of Flare Drivers: Magnetic Field Parameters	52

3.5	Results and Discussion	61
4	What Causes Homologous Eruptions?	65
4.1	Observations of Homologous Eruptions	67
4.2	Evolution of AR 11429 Leading to Homologous Eruptions	72
4.2.1	Evolution of the Photospheric Magnetic Field	72
4.2.2	Pre-eruptive Structures in the Corona	75
4.2.3	Initiation of the Eruption	81
4.3	Discussion and Conclusion	84
5	An atypical scenario: Compound Eruptions	88
5.1	Observations of the Compound Eruption	89
5.1.1	The Precursor Phase	90
5.1.2	The Impulsive Phase	91
5.2	Observations of the Pre-Eruption Evolution	96
5.2.1	Evolution of the Photospheric Magnetic Field	96
5.2.2	Evolution of the Pre-eruption Structure in the Corona	98
5.2.3	Observations of the Double-Decker Configuration	101
5.2.4	Coronal Magnetic Field Inferred from NLFFF Extrapolation	104
5.3	Discussion and Conclusion	107
6	Summary and Future Plans	111
6.1	Summary	111
6.2	Future Plans	113
	Bibliography	115

List of Tables

Table	Page
2.1 The HMI instrument characteristics. Table is taken from Schou et al. (2012).	19
2.2 The AIA instrument characteristics. Table is taken from Lemen et al. (2012).	23
2.3 The primary ions for each passband observed by AIA. Table is taken from Lemen et al. (2012).	24
2.4 Yearly variation of Active Region number and flares. *sunspot area in millionths of the solar hemisphere (MSH).	28
3.1 Magnetic field parameters formulae.	34
3.2 Active regions (ARs) from super-active ARs (SAARs) group. The first row shows the NOAA AR number. The second row shows the flare index (FI) of each ARs. The third row shows the maximum sunspot size (SS) achieved by each ARs. The fourth row shows the number of days (DO) each AR was observed on the solar disk. ARs having small (large) sunspot areas are in green (yellow).	37
3.3 Active regions (ARs) from low-active ARs (LAARs) group. The first row shows the NOAA AR number. The second row shows the flare index (FI) of each ARs. The third row shows the maximum sunspot size (SS) achieved by each ARs. The fourth row shows the number of days (DO) each AR observed on the solar disk. ARs having small (large) sunspot areas are in green (yellow).	37
3.4 Table showing the changes in the area and sunspot type during the period flares were recorded from the AR 11430. The second column is showing the changes in the area of the sunspot. The third, fourth, and fifth columns are showing the number of X, M, and C-class of flares produced by the ARs on each day respectively. The last column is showing the change in the sunspot configuration during the evolution.	42

3.5	Table showing the changes in the area and sunspot type during the period flares were recorded from the AR 12108. The second column is showing the changes in the area of the sunspot. The third, fourth, and fifth columns are showing the number of X, M, and C-class of flares produced by the ARs on each day respectively. The last column shows the change in the sunspot configuration during the evolution.	45
3.6	Table showing the changes in the area and sunspot type during the period flares were recorded from the AR 11515. The second column is showing the changes in the area of the sunspot. The third, fourth, and fifth columns are showing the number of X, M, and C-class of flares produced by the ARs on each day respectively. The last column is showing the changes in the sunspot configuration during the evolution.	48
3.7	Table showing the changes in the area and sunspot type during the period flares were recorded from the AR 11928. The second column is showing the changes in the area of the sunspot. The third, fourth, and fifth columns are showing the number of X, M, and C-class of flares produced by the ARs on each day respectively. The last column is showing the changes in the sunspot configuration during the evolution.	51
3.8	Average value of magnetic field parameters. First column shows the NOAA AR number. Second column shows the flare index within 60° of the central meridian. Third column shows the average value of unsigned magnetic flux (USF). Fourth column shows the net flux (NF). Fifth column shows the current density (J_z). Sixth column shows the current helicity (H_c). Seventh column shows the degree of current neutralization (NC). Eighth column shows the length of strong-gradient polarity inversion line (PIL). Ninth column shows the R-value.	58
3.9	Correlation between flare indices (FIs) and magnetic field parameters. . . .	61
4.1	Three homologous solar eruptions from AR 11429. ^a Initiation time of the solar eruption ^b flare location ^c peak time of GOES X-ray flux ^d first LASCO C2 appearance ^e linear speed of CME in LASCO C2, obtained from https://cdaw.gsfc.nasa.gov/CME_list/UNIVERSAL/2012_03/univ2012_03.html	68

List of Figures

Figure	Page
1.1 A simple bipolar AR. The left panel shows the sunspots in the HMI continuum on the southern hemisphere. The right panel shows the line-of-sight magnetogram for the corresponding sunspot. The leading (following) pole has positive (negative) magnetic flux and it is tilted towards the equator.	3
1.2 The cartoon representation of the Babcock-Leighton dynamo model. The red inner sphere indicates the radiative core and the blue mesh the surface of the Sun. Top panels show the conversion of poloidal into toroidal magnetic field, due to shearing of the poloidal field by differential solar rotation, and the emergence of magnetic fields as sunspots. Middle panels show the rise of additional sunspots, spreading of decaying spots, and generation of new surface global poloidal magnetic fields. Bottom panels show the transportation of surface flux towards poles, by meridional flow, and then down to bottom to flip the sign of poloidal field and to start a new solar cycle. Figure is taken from https://www2.hao.ucar.edu/hao-science/sun-dynamo-0	5
1.3 The cartoon model of the emerging magnetic flux tube. The sunspot is formed by the coalescence of many flux loops. The horizontal arrows show the separation of opposite magnetic fluxes during the emergence. Figure is taken from Zwaan (1987).	7
1.4 The cartoon model of the erupting flux rope and the different observed phenomena during the solar eruption. Figure is taken from Forbes (2000).	10
2.1 A model of SDO satellite with AIA, EVE, HMI, high-gain antennas, and solar arrays. The thrusters and main engine are located on the backside of the satellite. Figure is taken from Pesnell et al. (2012).	15
2.2 Schematic of HMI optical layout. Figure is taken from Schou et al. (2012).	16

2.3	Example of HMI tuning-position profiles obtained through the wavelength-dependence calibration procedure. Colored lines show the six tuning position with respect to the Fe I solar line with no doppler shifting at the disk center. The line spacing of the tuning positions is 76 mÅ. Figure is taken from Schou et al. (2012).	20
2.4	Plot of the total unsigned flux (USFLUX) calculated on an area containing NOAA ARs 11785, 11787, 11788 with CEA B _z data from SDO/HMI (blue and green curves). Also shown is the number of high confidence pixels (yellow and red curves). Note the appearance of 12-hour periodicities or undulations in the magnetic flux and the total number of high-confidence pixels due to systematic effects. The broad peaks in total unsigned flux are due to increased noise in the magnetic field measurements away from disk center (~ 60 from central meridian). Figure is adapted from Hoeksema et al. 2014. . .	21
2.5	The layout of the bandpasses in each of the four AIA telescope. Telescope 2 has an aperture blade to select between wavelength channels. The other telescopes rely on filters in filter wheels to select between channels. The top half of telescope number 3 has a MgF ₂ window with a coating centered at 1600 Å. Figure is taken from Lemen et al. (2012).	22
2.6	A cross sectional view of telescope number 2 of AIA. All four telescopes of the AIA have their own guide telescope to stabilize the image on the CCD. Figure is taken from Lemen et al. (2012).	22
2.7	Temperature response functions for the six EUV passbands of AIA. These are dominated by iron emission lines, calculated from the effective-area functions and assuming the CHIANTI model for the solar emissivity. Figure is taken from Lemen et al. (2012).	25
2.8	The number of ARs and flares from the Sun during the period of 2010-2015.	27
2.9	Plots of sunspot area versus flare-index. The left panel shows the scatter plot for all the ARs in the catalog. The right panel shows the scatter plot for the AR satisfying the selection criteria. ARs selected for the comparative study are circled in red.	30

3.1	<p>Snapshots showing the ARs, in B_{los} of HMI, with large sunspot area. The positive (negative) magnetic fluxes are shown in white (black). The left panels show the ARs with large flare productivity (SAARs). The right panels show the ARs with small flare productivity (LAARs). The location of C, M, and X-class flares (during the entire observational period) is shown in brown, blue, and red asterisks. The green lines show the location of the strong-gradient polarity inversion line.</p>	40
3.2	<p>Snapshots showing the ARs, in B_{los} of HMI, with small sunspot area. The positive (negative) magnetic fluxes are shown in white (black). The left panels show the ARs with large flare productivity (SAARs). The right panels show the ARs with small flare productivity (LAARs). The location of C, M, and X-class flares (during the entire observational period) is shown in brown, blue, and red asterisks. The green lines show the location of the strong-gradient polarity inversion line.</p>	41
3.3	<p>Evolution of AR 11430 as observed in the HMI line-of-sight magnetogram in the period of six days. Positive (negative) flux is shown in white (black). Locations of C-class flares are shown in brown asterisks.</p>	42
3.4	<p>Photospheric magnetic field evolution of AR 11430 in the 3D map obtained through the time-image stacking method (discussed in 3.1). The red (blue) structure shows the contour of negative (positive) magnetic flux ($B \geq 800$ G) of the AR between 2012 March 6 - 12. The green, cyan, and yellow arrows show the direction of the west limb, the north pole, and time respectively. The moving magnetic poles have a slanted shape. The white arrows show the motion of newly emerging magnetic fluxes and their interaction with existing magnetic fluxes. The overall magnetic configuration of the AR is simple throughout the evolution.</p>	43
3.5	<p>Evolution of AR 12108 as observed in the HMI line-of-sight magnetogram in the period of six days. Positive (negative) flux is shown in white (black). Locations of C-class flares are shown in brown asterisks.</p>	46

3.6	The photospheric magnetic field evolution of AR 12108 between 2014 July 3 - 11. The contour of negative (positive) magnetic flux ($ B \geq 800$ G) is shown in red (blue). The green, cyan, and yellow arrows show the direction of the west limb, the north pole, and time respectively. Opposite magnetic poles are far from each other throughout the evolution.	47
3.7	Evolution of AR 11515 as observed in the HMI line-of-sight magnetogram in the period of nine days. Positive (negative) flux is shown in white (black). Locations of C-class and M-class flares are shown in brown asterisks and green asterisks respectively.	49
3.8	The photospheric magnetic field evolution of AR 11515 between 2012 June 28 - July 6. The contour of negative (positive) magnetic flux ($ B \geq 800$ G) is shown in red (blue). The green, cyan, and yellow arrows show the direction of the west limb, the north pole, and time respectively. The mixed polarities in the middle show the interaction between opposite magnetic fluxes.	50
3.9	Evolution of AR 11928 as observed in the HMI line-of-sight magnetogram in the period of six days. Positive (negative) flux is shown in white (black). Locations of C-class and M-class flares are shown in brown and green asterisks respectively.	51
3.10	The photospheric magnetic field evolution of AR 11928 between 2013 December 16 - 22. The contour of negative (positive) magnetic flux ($ B \geq 800$ G) is shown in red (blue). The green, cyan, and yellow arrows show the direction of the west limb, the north pole, and time respectively. The mixed polarities in the middle show the interaction between opposite magnetic fluxes.	52
3.11	Evolution of magnetic field parameters in AR 11430. The first panel, at the top, shows the time-profile of total unsigned, positive, and negative magnetic flux in black, blue, and red respectively. The vertical grey lines show the time of C-class flares from the AR. The second panel shows the total current in black and the degree of net current neutralization in positive (negative) polarity in blue (red). The third panel shows the current helicity in black. The last panel shows the length of strong-gradient polarity inversion line (sgPIL) and R-value in solid black line and black asterisks respectively.	53
3.12	Evolution of magnetic field parameters in AR 12108. This is similar to Figure 3.11.	55

3.13	Evolution of magnetic field parameters in AR 11515. This is similar to Figure 3.11.	56
3.14	Evolution of magnetic field parameters in AR 11928. This is similar to Figure 3.11.	59
3.15	Scatter plots between magnetic field parameters and flare index (FI). The correlation coefficient between FI and parameters is on the upper right corner of each panels. The left, middle, and right upper panels show plots for total unsigned magnetic flux, current density, and current helicity respectively. The left, middle, and right lower panels show plots for deviation from degree of current neutrality, length of sgPIL, and R-value respectively.	60
3.16	Cartoon models showing the changes in the magnetic configuration due to new magnetic flux emergence. Top panels show the case of interaction between like magnetic fluxes of emerging and existing magnetic poles. The overall magnetic configuration would be simple and flare productivity would not change in this scenario. Middle and lower panels show the cases of interaction between unlike magnetic fluxes of emerging and existing magnetic poles. The overall magnetic configuration would be complex and intense flares would originate in this scenario.	63
4.1	Three homologous eruptions from NOAA AR 11429. (a-c) time profiles of GOES soft X-ray intensity flux during the three eruptions. The maximum flux in these profiles corresponds to X1.3, M6.3, M8.4 flares, respectively. The red dotted line in (a) shows the contamination in the X-ray profile due to an earlier eruption. (d-f) Overlay of the flare ribbons (in blue) observed in AIA 1600 Å on HMI LOS-magnetogram. (g-i) Difference images of AIA 193 Å showing the EUV dimming associated with each eruption. The white box represents the FOV of the magnetograms shown in (d-f).	70
4.2	Homologous CMEs seen from three different view points. Left panels: the COR2 images from SECCHI/STEREO-B. Middle panels: the C2 images from LASCO/SOHO. Right panels: the COR2 images from SECCHI/STEREO-A.	71
4.3	Time evolution of the magnetic-flux in the AR 11429 during March 4-13. The total unsigned magnetic flux is plotted in black, the total negative magnetic flux is plotted in red and the total positive flux is plotted in blue. Dashed vertical lines marks the time of three homologous solar eruptions.	73

4.4	Evolution of the photospheric magnetic field in NOAA AR 11429. Images are taken from the line-of-sight magnetograms of SDO/HMI and shown in a cylindrical equal-area heliographic projection. Left panels: the strong-gradient polarity inversion lines in green asterisks are overplotted on the HMI LOS-magnetogram. The red and cyan boxes, in (a), represent the northeast (NE) and southwest (SW) sub-regions respectively, and white arrows show the location of new flux emergence. The pink line in (d) shows the distance between the centroid of positive (P-SW) and negative (N-SW) polarity in the SW sub-region. Middle panels: the direction of motion of positive (negative) flux are overplotted on the HMI LOS-magnetogram in blue (red) arrows. Right panels: the direction of the horizontal component of magnetic fields are overplotted on the HMI LOS-magnetogram in brown arrows.	76
4.5	Convergence of opposite magnetic polarity and magnetic flux cancellation in the southwest sub-region of the AR 11429. Convergence rate is examined by monitoring the distance between the centroid of positive and negative magnetic polarity and is shown in black asterisks. The time profile of negative flux in the SW sub-region is in red. The vertical dashed lines refer to the time of three solar eruptions from the AR.	77
4.6	Evolution of non-potential parameters in AR 11429. Top panel: Degree of net current neutralization in positive (negative) polarity in blue (red). A higher value of around 1.8 suggest non-neutralized currents in the AR flux system and instability. The length of sheared PILs is also plotted in grey. Middle panel: the time rate of helicity flux is plotted in blue. Normalized accumulated helicity (time-integrated helicity flux normalized with square of the flux) is plotted in red. Bottom panel: energy flux injection (poynting flux) and its accumulated quantity in blue and red respectively.	78
4.7	Filament observed in the AIA 304 Å. The left panel shows the survived filament under the post-flare arcade of the eruption on 2012 March 7. The right panel shows the survived filament under the post-flare arcade of the eruption on 2012 March 9.	79
4.8	Filament of identical shape, in H α images from BBSO, were present persistently during the evolution of the AR 11429. White arrow in (a) points to the filament in southwest sub-region of the AR.	80

4.9	Observation of pre-eruptive coronal structure. Left panels: the hot-channel structures (HCS) before each eruptions in AIA 131 Å. The brighter part of the HCS is outlined by orange asterisk. Middle panels: the temperature map obtained using the DEM method. Right panels: the sigmoidal hot coronal structures in X-ray images. (c) and (f) images are from <i>Hinode</i> /XRT, and (i) is from <i>GOES</i> /SXI.	80
4.10	Magnetic structure modeled by NLFFF extrapolation. Left (right) panels show the top (side) view of magnetic field lines rendered on the HMI LOS-magnetograms before each eruption. The sheared and twisted field lines, along the southwest polarity inversion line (SW-PIL), are shown in blue-red lines. The green lines show the overlying magnetic field in the corona. . . .	81
4.11	Confined flare during the precursor phase of each eruption. The contours of flare ribbons during the precursor phase activity, as observed in AIA 1600 Å, are overplotted on the HMI LOS-magnetogram in blue. The red contours in (a) show the flare ribbons from an earlier eruption. The orange asterisks indicate the outline of the hot-channel structure observed in AIA 131 Å. . .	82
4.12	The magnetic topology at different evolutionary epochs of the AR 11429. (a) HMI LOS-magnetogram on March 9, red arrow shows the area where positive magnetic flux is almost surrounded by negative flux. (b-f) show the vertical slice of logarithm squashing factor Q ($\text{Log}(Q) > 5$) at the location of the green line in (a). Left panels show similar magnetic topology before each eruption.	83
4.13	Contours of critical decay index ($n \geq 1.5$) for the AR 11429. The contours are overplotted on HMI LOS-magnetogram and different colors represent the heights at which decay index is calculated.	84
5.1	The three phases of the compound-eruption. The black curve shows the SXR time-profile observed by GOES. The colored lines show the intensity plot for different AIA passbands. The vertical-dashed lines indicate the beginning and ending of the impulsive phase. The two peaks in the impulsive phase are pointed by two black arrows.	90

5.2	The precursor phase of the compound eruption. The left four images show the change of the hot structure in AIA 131 Å during the precursor phase. The right four panels show the flare-ribbon evolution during the pre-flare phase in 1600 Å (blue contours), plotted over HMI/LOS magnetograms (gray scale).	92
5.3	Evolution of the compound eruption during the impulsive phase. The left four panels are showing the running difference images for the AIA 131 Å and the right four panels are showing the flare-ribbon evolution, over-plotted over magnetogram, in AIA 1600 Å in blue. The erupting HCSA and HCSB are shown in green and red asterisks respectively. The blue line in panel (a) is the position of the slice used for the study of kinematic evolution of two erupting structures.	93
5.4	Kinematic evolution of erupting structures. (a) The time-stacking plot obtained from the running difference of AIA 131 Å images (the position of the slice is shown in the Figure 5.3(a)). The green asterisks mark the positions of the outer edge of the erupting HCSA and the red asterisks mark the position of the outer edge of the erupting HCSB of DD configuration. The two erupting structures are clearly resolved. (b) The black curve is the GOES SXR profile and blue curve is showing the normalized AIA 304 Å intensity. The green curve is showing the velocity variation of HCSA during the impulsive phase, it has two acceleration phases. The curve in yellow is the derivative of GOES flux. The vertical line is showing the starting time of the second acceleration phase of HCSA and it corresponds to the second increase in the intensity of the AIA 304 Å.	95
5.5	The CME resulted from the compound eruption observed from three different points of view. The three panels from left to right show COR2 image from SECCHI/STEREO-B, C2 image from LASCO/SOHO and COR2 images from SECCHI/STEREO-A, respectively.	96

5.6	Evolution of the photospheric magnetic field in NOAA AR 11429. Images are taken from the LOS magnetograms of SDO/HMI and are shown in CEA heliographic projection. Green lines are the strong-gradient polarity inversion line (PIL). Top panel (a) shows the entire AR, white and black boxes show the NE and SW sub-region respectively. Panels (b)-(g) show the evolution of the magnetic configuration in the SW part of the AR. Red lines, in panel (a) and (g), show the distance between the centroid of two strong bipoles. The yellow circle in panel (b) is the location of prominent flux cancellation. The orange arrow in panel (c) is the direction of motion of negative flux.	97
5.7	Evolution of the coronal hot-structure before the eruption in NOAA AR 11429. AIA 131 Å passband data are shown in red-white, and the HMI data are shown in white (positive flux) and black (negative flux). In panels (b) and (e) the coronal hot-structures are also traced with dark lines.	99
5.8	Two erupting filaments/prominences in a double-decker configuration. The upper filament (A) is marked with green asterisks and the lower filament (B) with red asterisks. The upper three panels show the filaments at different time in <i>STEREO-A</i> EUVI 171 Å. The lower three panels show the two filaments in <i>SDO</i> AIA 304 Å.	100
5.9	Images illustrating the two hot-channel structures of the double-decker configuration in the SW region of the AR 11429. Panels (a) and (b) show the temperature map obtained with a DEM method. Panels (c) and (d) show the images in AIA 94 Å. Panels (e) and (f) show two hot coronal structures in X-ray images from GOES/SXI. The green and red asterisks show the high-lying and low-lying structures respectively.	102
5.10	Magnetic field configuration in the AR 11429 at 15:58 UT on March-10, 2012, immediately before the eruption. The background shows the Bz component of the vector magnetogram with positive (negative) flux in white (black). Panel (a) also shows the direction of horizontal magnetic field at the photosphere in red and green. Panel (b) shows selected magnetic field lines in the AR above the photosphere obtained from the NLFFF extrapolation. Sheared magnetic field lines along the NE-PIL is shown in brown. The sheared and twisted magnetic field lines, along the SW-PIL, is shown in red. The white lines show the overlying magnetic field in the corona.	105

- 5.11 Evolution of coronal current density (obtained from the NLFFF extrapolation) in the AR 11429. Panels (a)-(c) show the normalized-integrated current density along the LOS in red-white and the Bz component in the background. Panels (d)-(f) show the vertical slice of the current density along the blue line (top left panel). During the evolution, the current density changed from more diffused to more concentric around the location of the hot channel. . . 105
- 5.12 The three erupting scenarios of the double-decker (DD) configuration. 1) The upper three panels depict the case where only the upper-branch of the DD erupts. 2) The middle three panels show the merging of the two branches of DD, which erupts together. 3) The lower three panels show the eruption of the two branches of the DD separately and their interaction after the eruption.107

Abstract

CAUSES OF SOLAR ERUPTIONS: A COMPARATIVE STUDY OF SUPER-ACTIVE AND LOW-ACTIVE ACTIVE REGIONS

Suman Dhakal, PhD

George Mason University, 2021

Dissertation Director: Dr. Jie Zhang

Solar Active Regions (ARs) are the areas of strong magnetic flux of opposite polarities. These are the main source-location of solar eruptions. By solar eruptions, we mean the explosive events that rapidly release energy from the magnetized solar corona resulting in flares and Coronal Mass Ejections (CMEs). During solar eruptions, a tremendous amount of plasma and energy is released from the Sun, which can produce space weather disturbances and disrupt our space missions, satellites, radio communications, and even power grids on the Earth. The understanding of the origin of solar eruptions and their propagation through interplanetary space is crucial to mitigate the damages they could produce. However, a proper understanding of the physical mechanisms leading to eruptions is still lacking, and consequently a reliable and accurate forecast is not possible yet. This dissertation, using advanced observations from AIA and HMI instruments onboard the SDO spacecraft, addresses many important issues regarding the origin of solar eruptions.

First, this dissertation investigates how the evolution of ARs leads to different flare productivity. This study illustrates that though the magnetic flux emergence is important, it alone is not sufficient to increase the flare productivity of an AR. The new emergence can lead to either the interaction of like or opposite magnetic fluxes of non-conjugate pairs

(magnetic poles not emerging together as a conjugate pair, as in a bipolar configuration). In the former case, the overall magnetic configuration remains simple and the flare productivity of AR does not change with emergence. In the latter case, the convergence of opposite magnetic fluxes of non-conjugate pairs results in a complex magnetic configuration with long polarity inversion line (PIL). This study suggests that the long-term shearing motion and flux cancellation, along the PIL of non-conjugate pair, produce multiple intense flares. In addition, the dissertation also analyzes the magnetic field parameters including total magnetic flux, net flux, current density, current helicity, degree of current neutralization, length of strong-gradient PIL (sgPIL), and R-value to quantify the flare drivers. Our study found the weakest correlation (0.6) between flare index (FI) and total flux content of ARs. This demonstrates that the size of the AR does not necessarily determine the flare productivity. The correlation between the FI and sgPIL/ R-value was the strongest (0.8). Such a high correlation suggests that the ARs having long PIL for a longer evolutionary period have a higher probability of producing many intense flares.

Second, the dissertation provides, for the first time, the evidence that shearing motion and flux cancellation play a major role in repetitive similar solar eruptions (homologous eruptions) at different evolutionary phases of an AR. Our study shows that after an eruption, the continuation of shearing motion and flux cancellation not only store magnetic helicity and energy but also form an identically-shaped erupting structure along the same PIL. The present study also demonstrates that the homologous eruptions can have similar signatures in the pre-flare phase due to similar magnetic topology. ARs can have a similar magnetic topology for a long period due to slow changes in the magnetic configuration or the formation of similar magnetic structures. Our study supports the idea of the formation and existence of pre-eruptive magnetic flux ropes.

Third, the dissertation describes an atypical solar eruption, where two closely connected magnetic structures erupted consecutively within twelve minutes. This study provides a unique opportunity to reveal the formation process, initiation, and evolution of complex eruptive structures in solar ARs. This study shows that long-term continuation of shearing

motion and magnetic flux cancellation form a new low-lying magnetic structure below the existing high-lying structure. These magnetic structures are arranged along the same PIL in a double-decker configuration. The high-lying magnetic structure becomes unstable and erupts first, appearing as an expanding hot channel seen at extreme ultraviolet wavelengths. About 12 minutes later, the low-lying structure also starts to erupt and moves faster compared to the high-lying one. As a result, the two erupting structures interact and merge with each other, appearing as a single CME in the outer corona. The dissertation shows that the successive destabilization of two separate but closely spaced magnetic structures, possibly in the form of magnetic flux ropes, leads to a compound solar eruption. Further, the dissertation describes the different scenarios by which the two branches of a double-decker configuration can erupt.

In short, this dissertation work has made significant progress toward our understanding of the origin of solar eruptions. The work on the flare productivity of various types of ARs will improve the prediction of the occurrence of solar flares when combined with machine learning techniques. The upcoming 4-meter Daniel K. Inoue Solar Telescope (DKIST) observations will provide an ultimate verification on the importance of flux cancellation in producing solar eruptions as suggested in this study.

Chapter 1: Introduction

The Sun is our nearest star. This hot ball not only emits heat and light but also plasma continuously as solar wind. The solar wind filling the interstellar medium, far beyond the orbits of planets, creates a bubble known as the heliosphere. The high conductivity of the plasma also carries the solar magnetic field, which is frozen-in into the solar wind. The magnetic field is wound up in the form of Archimedian spirals by the solar rotation. Both solar wind and the frozen-in magnetic field undergo long-term systematic changes in properties during the solar cycle and short-term changes in properties during the transient disturbances related to explosive solar events. The variable conditions on the Sun and in the interplanetary space that can affect the technology's performance used on the Earth and in space is termed as space weather. Different solar activities could disturb the ambient solar wind condition and lead to space weather phenomena. Solar eruptions, in the form of flares and coronal mass ejections (CMEs), are the main drivers of space weather disturbances. Solar eruptions originating at the Sun, traveling through the interplanetary space could interact with our space missions. Normally, the Earth is protected from the impact of ambient solar wind due to its magnetic fields. Nevertheless, the disturbances from flares and CMEs can affect space missions, space-based telecommunications, broadcasting, weather services and navigation, and in extreme cases the ground-based power grids through induced currents. As our dependency on technology is increasing, the understanding of the origin and propagation of solar eruptions through interplanetary space is becoming critical. On the Sun, Active Regions (ARs) are the main center of solar eruptions, thus the study of ARs is inevitably important to understand and predict solar eruptions.

1.1 Active Regions

ARs are the region on the Sun with strong magnetic flux concentrations. They are considered “Active” as they are the main sources of a variety of solar activities like X-ray loops, small-scale brightenings, jets, large flares, and CMEs. They were first identified as dark patches, called sunspots, in the visible light on the photosphere. Large sunspots can be seen by unaided eyes and were reported to be observed long before the invention of telescopes (see, Vaquero 2007). Through the Zeeman effect, Hale (1908) had shown the existence of magnetic field in sunspots for the first time. Sunspots are the regions where strong magnetic fields cross the photosphere and go all the way to the solar corona. The strong magnetic fields in sunspots prevent the convection of plasma and thus heat from the surrounding regions, which makes the spots cooler and darker than the neighboring quiet Sun. The central part of a sunspot is dark umbra which is surrounded by a slightly light-dark penumbra (see Figure 1.1). The magnetic field strength on umbra can vary from 1700-3700 **G** and therefore it is relatively 1000-1900 **K** cooler than the quiet Sun. The magnetic field strength decreases to 700-1000 **G** at the edge of the penumbra and is about 250-400 **K** cooler than the quiet Sun (see, Livingston 2002; Solanki 2003). Though the observation of ARs started in visible light as sunspot on the photosphere, with the advancement of technology they are observed in a wide range of wavelengths and at different solar atmospheric layers. For example, an AR appears as dark spots on the photosphere in visible light and the same AR appears as a bright loop system in the corona in EUV and X-ray lights. Thus in a comprehensive sense ARs can be defined as, in the words of van Driel-Gesztelyi & Green (2015), “Active regions are the totality of observable phenomena in a 3D volume represented by the extension of the magnetic field from the photosphere to the corona, revealed by emissions over a wide range of wavelength from radio to **X**-rays and γ -rays (only during flares) accompanying and following the emergence of strong twisted magnetic flux ($\text{kG}, \geq 10^{20}$ Mx) through the photosphere into the chromosphere and corona”. This definition treats ARs as a whole set

of observable phenomena within a 3D volume, where magnetic fields extend from the photosphere to the corona. However, the National Oceanic and Atmospheric Administration (NOAA) still uses the sunspot to identify and number ARs.

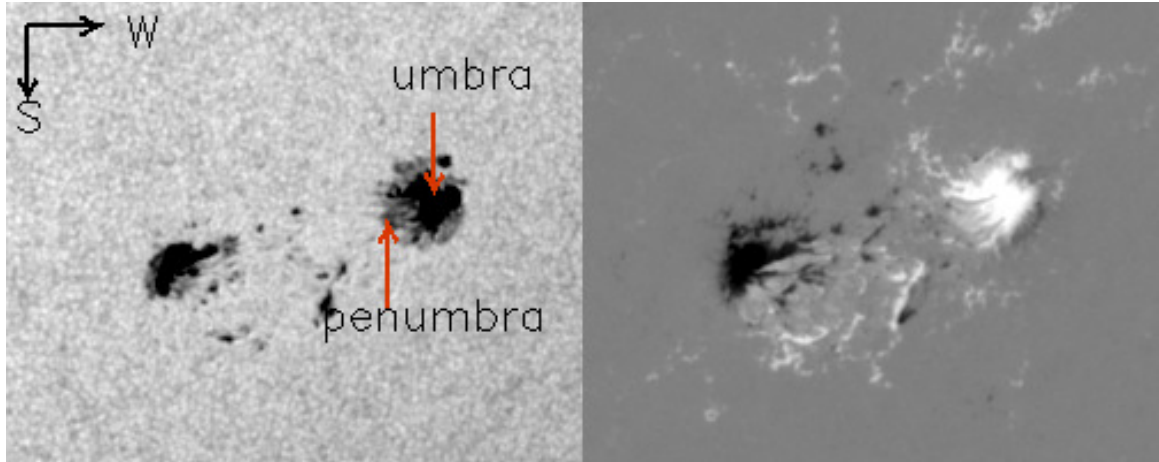


Figure 1.1: A simple bipolar AR. The left panel shows the sunspots in the HMI continuum on the southern hemisphere. The right panel shows the line-of-sight magnetogram for the corresponding sunspot. The leading (following) pole has positive (negative) magnetic flux and it is tilted towards the equator.

The number and locations of ARs, on the Sun, vary with the solar cycle. During solar maxima more than 10 sunspots/ARs could be visible and during the solar minima from none to few ARs could be visible on the solar surface (Solanki, 2003). Carrington (1858) found that the locations of the emerging sunspots are not random, they emerge inside the activity belt. The sunspots appear in higher latitudes (as high as 40°) at the beginning of a solar cycle and the locations of the new sunspots move towards the equator with the progress of the solar cycle. For a typical bi-polar AR, there are two sunspots. The magnetic pole towards the west (east) is known as the leading (following) pole. Generally, a tilt exists between the leading and the following pole, this is known as Joy's law. The leading pole tends to be nearer to the equator than the following pole (see Figure 1.1). The

tilt of ARs, with respect to the equator, increases with the latitude (Hale et al. 1919). All bipolar regions have the same arrangement of the polarities in a given hemisphere, with the opposite sense in the other hemisphere (known as Hale’s law; Hale et al. 1919). The sign of the leading pole changes in the beginning of each solar cycle. On the basis of the magnetic polarities of sunspots, they can be divided into the following types: i) α spots: Single spots or group of small spots with the same magnetic polarity. These are also known as unipolar sunspots and are generally associated with decaying ARs. ii) β spots: Two spots with opposite polarity. These are also known as bipolar spots. iii) γ spots: Multiple spots of positive and negative polarities which can not be simply classified as a bipolar sunspots due to their irregularities. iv) δ spots: These are complex sunspots, where the umbrae of opposite magnetic polarities lie in the same penumbra. An AR comes under any of these sunspot types or their combination like α/β , β/γ , and $\beta/\gamma/\delta$.

1.1.1 Magnetic Origin of Active Regions

Magnetic fields in the Sun are believed to originate at the tachocline layer through the dynamo process. The tachocline layer is the layer between the radiative and the convective zones, where differential solar rotation starts to happen. Observational properties such as Hale’s law, Joy’s law, and ~ 11 years solar cycle indicate that the solar magnetic fields are globally organized and their spatial and temporal evolution are systematic. The Babcock-Leighton dynamo model (first proposed by Babcock 1961) explains the solar cycle and global magnetic-evolution as a large-scale cycle between poloidal and toroidal magnetic fields (see Figure 1.2).

Sometimes, magnetic strands from the toroidal band could rise and travel through the convection zone to emerge as AR at the photosphere. MHD simulation and thin flux tube models are used to understand the rise of the magnetic flux as AR. The thin flux tube model assumes that the flux tube is very long compared to the cross-section size of the flux tube. The horizontal flux tubes are stored in the overshoot layer, at the base of the convection zone (van Ballegoijen 1982). Hydrostatic equilibrium of the flux tube requires that the

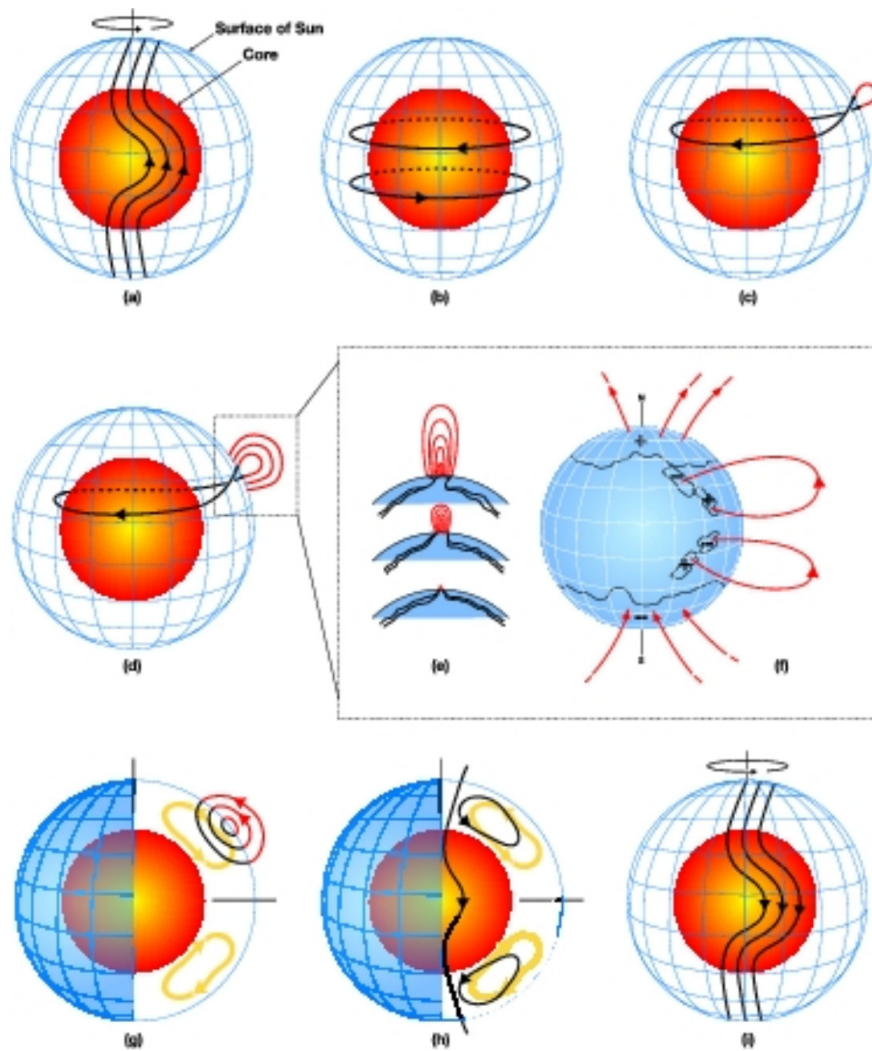


Figure 1.2: The cartoon representation of the Babcock-Leighton dynamo model. The red inner sphere indicates the radiative core and the blue mesh the surface of the Sun. Top panels show the conversion of poloidal into toroidal magnetic field, due to shearing of the poloidal field by differential solar rotation, and the emergence of magnetic fields as sunspots. Middle panels show the rise of additional sunspots, spreading of decaying spots, and generation of new surface global poloidal magnetic fields. Bottom panels show the transportation of surface flux towards poles, by meridional flow, and then down to bottom to flip the sign of poloidal field and to start a new solar cycle. Figure is taken from <https://www2.hao.ucar.edu/hao-science/sun-dynamo-0>.

external gas pressure (p_e) on the tube is balanced by the sum of the magnetic pressure (p_m) and internal gas pressure (p_i) of the tube i.e. $p_e = p_m + p_i$. As magnetic pressure

is a positive quantity, the above condition implies $p_i < p_e$. For a flux tube in the state of thermal equilibrium, lower gas pressure leads to the condition of lower plasma density inside the tube. The plasma density difference between inside and outside of the flux tube exerts a buoyant force (magnetic buoyancy) on the flux tube and rises it (Parker, 1955). The rising flux tube tends to rotate clockwise (anticlockwise) in the northern (southern) hemisphere due to the Coriolis force on its apex. This rotation makes the leading polarity to tilt more towards the equator (D’Silva & Choudhuri, 1993). As the flux tube approaches the photosphere, the rising velocity decreases and begins to pile up beneath the photosphere. The magnetic flux can rise through the photosphere only if it has sufficient magnetic field strength or twist (Archontis et al. 2004; Murray et al. 2006). During the emergence the magnetic tension makes the plasma of the two magnetic polarities to move in east-west direction, which produces the shear pattern along the polarity inversion line (Fan, 2001). As the magnetic polarities move away from each other, the atmospheric magnetic field lines are stretched, thus reducing the twist in these field lines.

1.1.2 Evolution of Active Regions

The journey of an AR starts with the emergence of bipolar flux regions and ends with the disappearance of the magnetic flux. The lifetime of an AR is defined as the time period for which it can be identified as a bipolar magnetic structure. In general, the lifetime of an AR can be divided into two phases: i) Flux emergence phase, and ii) Decay phase. The life-cycle of a complex AR may comprise of many episodes of flux emergence and decay. During the flux emergence phase, many small flux regions emerge on the photosphere. The opposite magnetic fluxes move away from each other and like fluxes regions coalesce together to form a bigger region, which can be identified as sunspots. Observations and theoretical models support the idea of the emergence of Ω -shaped flux tube from the base of the convection zone (see Figure 1.3). At the end of the emergence phase, the two magnetic poles attain a maximum separation distance. The distance separating opposite poles tends to increase with the flux content of the AR (Wang & Sheeley 1989 and Tian et al. 2003).

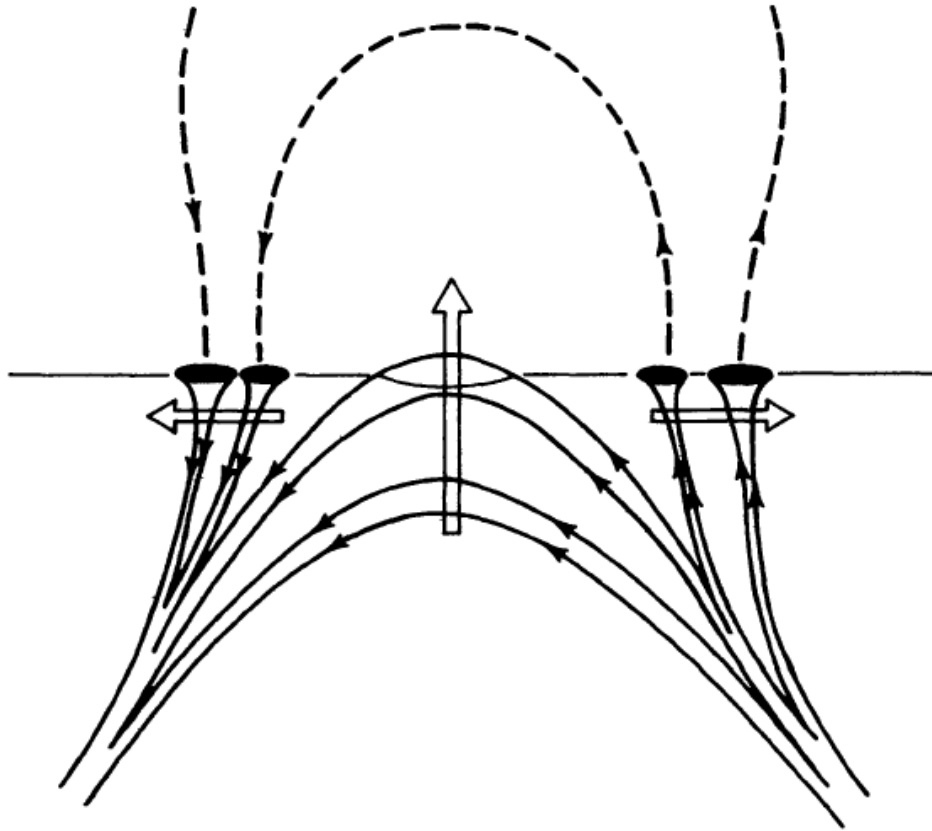


Figure 1.3: The cartoon model of the emerging magnetic flux tube. The sunspot is formed by the coalescence of many flux loops. The horizontal arrows show the separation of opposite magnetic fluxes during the emergence. Figure is taken from Zwaan (1987).

As an AR reach its maximum area, small magnetic flux regions start to detach and disperse from the sunspot and the AR starts to decay. Most of the time, the following spot is more dispersed than the leading spot. The processes by which an AR loses its magnetic flux/area might be present even before it attains maximum area, so it is possible that an AR starts decaying before it matures. Depending upon the total magnetic flux content and the area, it could take days (ephemeral ARs) to months (big ARs) for an AR to decay completely. The fragmentation of ARs is an important and necessary condition for the decay of large ARs. However, it is not clear how and why the fragmentation begins in ARs. Possible reasons for the fragmentation could be the presence of umbral dots and light

bridges, where convection flow could re-establish/ present (Borrero & Ichimoto 2011; Bumba 1965). Umbral dots are small, bright-spots in the dark umbra and light bridges are the bright line like region which split the sunspot into smaller regions. The other way of decaying could be the presence of Moving Magnetic Features (MMF; Harvey & Harvey 1973). MMFs are small and weak magnetic fluxes which move radially outwards from the AR and surround the AR as a moat of magnetic fluxes. Decaying of an AR is a necessary but not sufficient condition for having MMF. MMF could be both unipolar or bipolar in nature. Harvey & Harvey (1973) explained MMF as the separation of the flux tube from the sunspot and suggested that the MMFs can carry magnetic flux away from the spot. However, it is not definite that all of the MMFs are separated flux tubes from the sunspot and can carry magnetic flux from the AR (Zhang et al. 1992; Ryutova & Hagenaar 2007). Generally, the decaying of sunspots depends upon factors such as: the complexity of ARs, whether AR is isolated or in a group, numbers of bright dots in the umbra (see Solanki 2003 and references therein). Once AR fragmented into smaller and weaker magnetic flux region, diffusion and advection flow become effective to disperse the magnetic flux.

1.2 Origin of Solar Eruptions

Solar eruptions are the most spectacular events happening on the Sun. By solar eruption we mean flares and coronal mass ejections (CMEs). Though solar flares could be observed in the entire electromagnetic spectrum (Fletcher et al. 2011), they are generally identified as a peak in Soft X-rays (SXR) and UV brightening. CMEs are generally identified as an outward moving bright arc in coronagraphs. Around 100 ergs cm^{-3} energy is carried away during moderately large CMEs. Different forms of energy available on the Sun are kinetic ($10^{-5} \text{ ergs cm}^{-3}$), thermal (0.1 ergs cm^{-3}), gravitational (0.5 ergs cm^{-3}), and magnetic (400 ergs cm^{-3} ; see Forbes 2000). Considering the amount of energy released and the energy available on the Sun, only magnetic energy seems large enough to be the source of the energy of the solar eruptions.

When occurring together, flares and CMEs are considered the manifestation of a single energy release process, where stored magnetic free energy converts to radiative and kinetic energies (Forbes 2000). The standard model of solar eruption, also known as the CSHKP model (initially developed by Carmichael 1964; Sturrock 1966; Hirayama 1974; Kopp & Pneuman 1976), describes it as the eruption of a magnetic flux rope (MFR) through magnetic reconnection, MFR being a highly sheared and twisted magnetic field structure. It is kept in equilibrium by the overlying magnetic field lines in stable condition. Under certain conditions, it becomes unstable and starts to rise. While rising it drags the overlying magnetic field lines, making them to come close to each other in an antiparallel manner below it (see Figure 1.4). A current sheet is formed below the rising MFR, between antiparallel magnetic field lines, where magnetic reconnection results in flares and the new connection removes the overlying constraint over MFR and accelerates it. The standard model is very efficient in describing the general evolution of solar eruptions. However, it does not address many important questions like i) whether MFR needs to be present before the eruption or not, ii) how MFR formed on the Sun, and iii) what triggers the eruption.

Though in-situ observations in the solar wind indicate that all CMEs reaching 1 AU may contain MFRs (Gopalswamy et al. 2013), there is a debate regarding the existence of MFRs prior to the eruption. Certain studies support the idea of the existence of pre-eruptive MFR (e.g., Kliem & Török 2006; Zhang et al. 2012), while others suggest its formation during the eruptions (e.g., Lynch et al. 2008; Gopalswamy et al. 2017). It is important to note that an MFR is the region of low plasma density, therefore it is very difficult to detect the MFR in the corona directly. However, there are indirect evidence that may suggest the existence of MFR such as cavity and prominence (filament at solar disk), sigmoidal bright loops in X-rays (Rust & Kumar 1996; Green et al. 2007), AIA/SDO hot channel structures (Cheng et al. 2011; Zhang et al. 2012), and dips or bald patches in filament channels (Lites 2005; López Ariste et al. 2006). Non-linear-force-free-field (NLFFF) extrapolation results obtained for the photospheric boundary conditions could also indicate pre-eruptive MFRs (e.g., Chintzoglou et al. 2015).

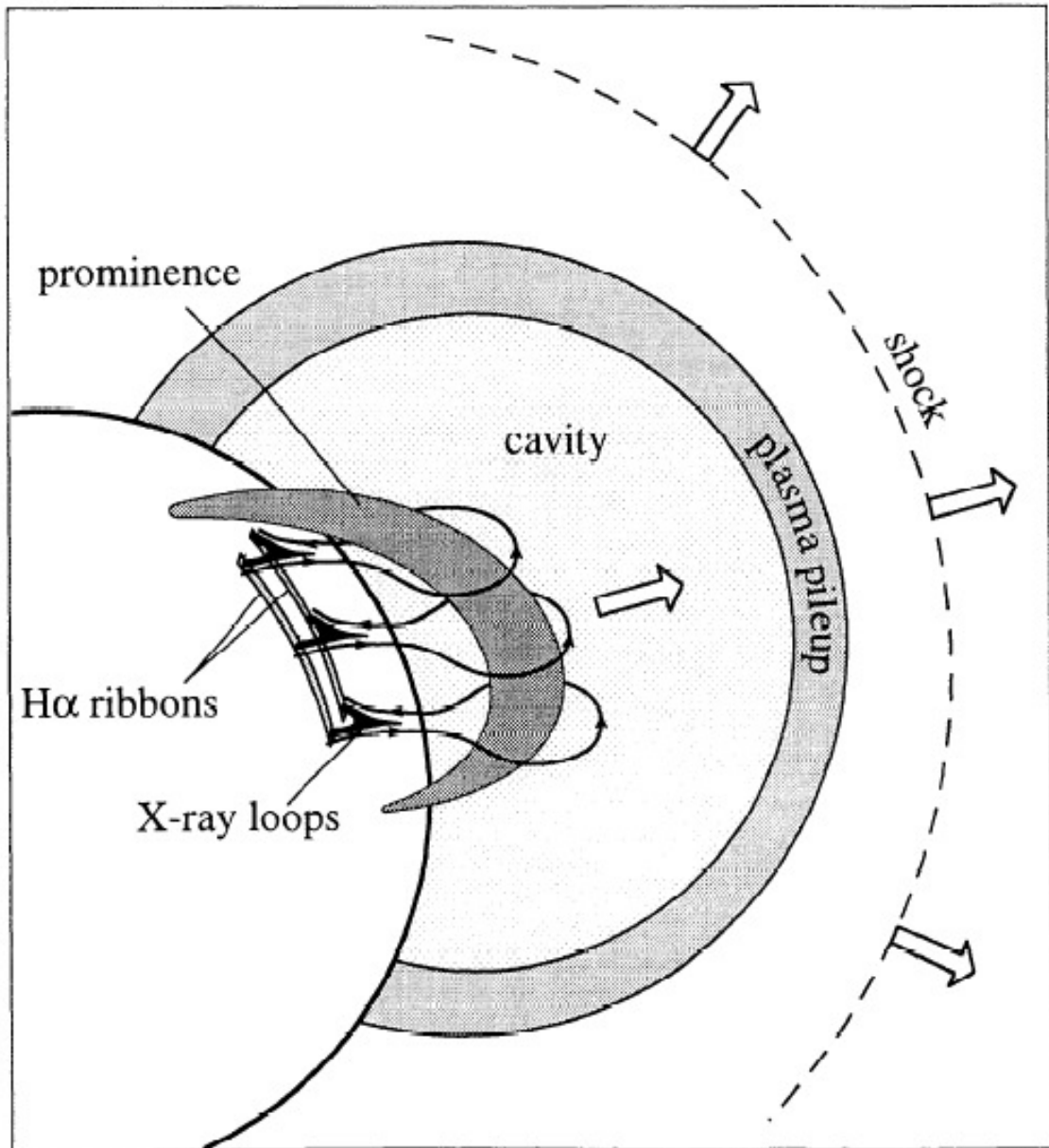


Figure 1.4: The cartoon model of the erupting flux rope and the different observed phenomena during the solar eruption. Figure is taken from Forbes (2000).

MFR can be formed by different mechanisms such as shearing motions (e.g., Amari et al. 2000, 2003; Jacobs et al. 2009), flux cancellation at polarity inversion line (PIL) (e.g., van Ballegoijen & Martens 1989; Aulanier et al. 2010; Green et al. 2011), flux emergence (e.g.,

Fan & Gibson 2003; Leake et al. 2013), and flare reconnection during an eruption (e.g., Gopalswamy et al. 2017).

An MFR in equilibrium has a downward magnetic tension force balanced with an upward magnetic pressure force. A break in equilibrium, either due to a decrease of tension force or the increase of the upward magnetic pressure force, would make the MFR to rise and initiate an eruption. There are several proposed mechanisms that can break the equilibrium and trigger eruption such as tether-cutting (e.g., Moore et al. 2001), breakout reconnection (Antiochos et al. 1999), flux emergence (Chen & Shibata 2000, and catastrophe mechanism (e.g., Török & Kliem 2005; Kliem & Török 2006).

Our understanding on the formation of pre-eruptive magnetic structure and the initiation of solar eruption has been improved a lot by the past several decades of studies. The goal of solar physicists is to have a general model to explain the diverse mechanisms of formation of erupting magnetic structures and initiation of eruptions.

1.3 Topics Covered in the Thesis

1.3.1 What Determines the Flare Productivity of ARs

Solar eruptions are magnetic in origin. On the Sun, strong magnetic fields are mostly concentrated on ARs and they are the main sources of solar flares. Flare productivity varies among ARs, certain ARs produce many intense flares while others do not produce a single intense flare. We call the ARs having high flare productivity super-active ARs (SAARs) and low flare productivity low-active ARs (LAARs). What determines the flare productivity of an AR is a debatable issue. Many proposed mechanisms can increase the flare productivity, such as continuous strong shearing motions between opposite magnetic poles (e.g., Krall et al. 1982), new flux emergence (e.g., Leka et al. 1994), and even the intrinsic property of emerging magnetic flux tube (e.g., Toriumi et al. 2014). Typically, major flares are correlated with many observational signatures such as AR's size (e.g., Yang et al. 2017), complex magnetic configurations like δ -configuration (e.g., Shi & Wang 1994),

anti-Hale magnetic configuration (e.g., Tian et al. 2002), and long polarity inversion lines (PILs; e.g., Vasantharaju et al. 2018a).

We analyzed twenty ARs, in Chapter 3, with focuses on three major topics i) why certain ARs have higher flare productivity, ii) understanding how the diverse physical processes are related to each other, and iii) quantifying the flare drivers. ARs were selected on the basis of sunspot size and flare productivity (discussed in detail in Chapter 2). Ten of the selected ARs were SAARs and the other ten were LAARs.

1.3.2 Successive Solar Eruptions From the Same Location

ARs can produce multiple solar eruptions from the same local region. Such repetitive solar eruptions are called homologous if they have the same flare foot points, similar EUV dimmings, and coronagraph appearances (Zhang & Wang 2002). Multiple eruptions within a short period or from close proximity have a higher probability to interact with each other. The interaction of CMEs plays an important role in solar energetic particle (SEP) events (Gopalswamy et al. 2002). Therefore, the study of such events is very important from the perspective of the space weather impact. Magnetic flux emergence, during the flux emergence phase, can produce homologous eruptions (e.g., Nitta & Hudson 2001). Also, shearing motion and flux cancellation, during the flux decaying phase, can produce homologous eruptions (e.g., Li et al. 2010). Past studies suggest that homologous eruptions can be triggered by similar mechanisms, such as moving magnetic features (Zhang & Wang 2002), a coronal null point magnetic configuration (e.g., DeVore & Antiochos 2008), and tether reconnection due to shearing motion (e.g., Vemareddy 2017a). Identification of triggering mechanisms would be useful to predict the successive eruptions from ARs.

Chapter 4 presents the study of three homologous eruptions from an AR. The study focuses on i) identifying the major physical processes responsible for homologous eruptions at different evolutionary phases, ii) tracking changes in magnetic topology with successive eruptions, iii) identifying the triggering mechanism.

1.3.3 Origin of Compound Eruption

Multiple MFRs may exist at the same time on the Sun. They may form at different regions on the Sun (e.g., Török et al. 2011) or at different PILs of the same AR (e.g., Chintzoglou et al. 2015). Successive eruptions of these MFRs within a short period of time are known as sympathetic eruptions. Relation between such consecutive eruptions is debatable (Biesecker & Thompson 2000). Sometimes, instead of different locations, two MFRs can form along the same PIL. In such cases, one of the MFRs lies above the other along the same PIL in a double-decker (DD) configuration (e.g., Liu et al. 2012). Observation of DD configuration is very rare, which may be because such structures are rare and/ or because of the difficulty in identifying them.

Using data from multiple instruments, observing the Sun from different viewing angles, Chapter 5 describes the study of the eruption of a DD configuration. The study focuses on i) the formation mechanism of the DD configuration, ii) the pre-eruptive arrangement of the DD system, and iii) eruption of the DD system.

1.3.4 Outline of Dissertation

Chapter 2 describes the instruments and data, primarily used in this study, and the creation of a catalog. The catalog is created for the ARs that appeared on the Sun during 2010 - 2015. Chapter 3 describes the evolutionary differences between SAARs and LAARs. Further, it also compares the evolution of magnetic field parameters among these ARs. Chapter 4 describes the origin of homologous eruptions at different evolutionary phases of an AR. These eruptions occurred from the same PIL in the interval of ~ 4 days. Chapter 5 describes how two magnetic structures can form and exist simultaneously along the same PIL. Besides formation and pre-eruptive configuration, it also describes how such a system can erupt from the Sun. Chapter 6 contains a summary and future plans.

Chapter 2: Data and Active Region Catalog

For the study of this dissertation, we primarily used the data from the Helioseismic and Magnetic Imager and the Atmospheric Imaging Assembly. Both of these are onboard the *Solar Dynamics Observatory* and are discussed in the following sections.

2.1 The Solar Dynamic Observatory

The *Solar Dynamics Observatory* (SDO) (Pesnell et al. 2012) is the first mission under NASA's Living With a Star (LWS) Program. Its main goal is to understand the solar variations that influence life on Earth and humanity's technological systems and improve the prediction capability of such variations. It was launched from Kennedy Space Center, FL USA, aboard an Atlas V 401 (AV-021) launch vehicle on 11 February 2010 at 15:23 UT. It carries three scientific instruments, the *Helioseismic and Magnetic Imager* (HMI) (Schou et al. 2012), the *Atmospheric Imaging Assembly* (AIA) (Lemen et al. 2012) and the *Extreme ultraviolet Variability Experiment* (EVE) (Woods et al. 2012; see Figure 2.1).

In order to handle its large data rate, it has been placed into an inclined geosynchronous circular orbit with an orbital inclination of 28° about the longitude of the SDO-dedicated ground station in New Mexico. A drawback of the inclined geosynchronous orbit is that twice a year the Earth comes between the Sun and SDO (Earth-shadow or eclipse seasons). The duration of eclipse season is two-three weeks, where SDO experiences a daily interruption of solar observations. In addition, there are three lunar transits per year. Nevertheless, its continuous observations of the Sun with rapid time-cadence has been very useful for the solar community to increase our understanding of our nearest star. SDO started sending science data on 1 May 2010.

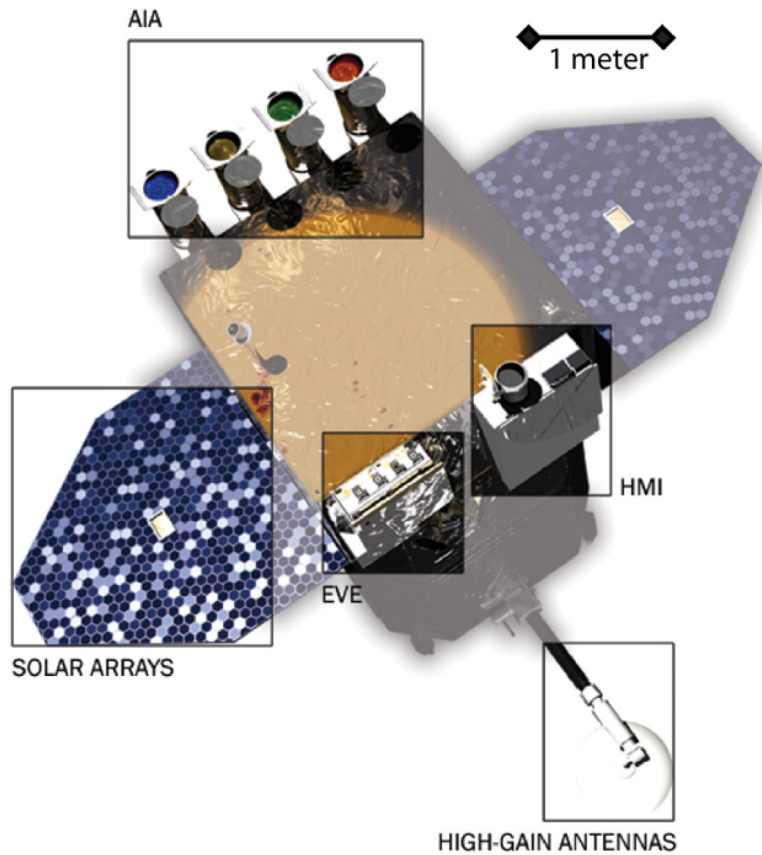


Figure 2.1: A model of SDO satellite with AIA, EVE, HMI, high-gain antennas, and solar arrays. The thrusters and main engine are located on the backside of the satellite. Figure is taken from Pesnell et al. (2012).

2.1.1 The Helioseismic and Magnetic Imager

The primary goal of the HMI is to study the origin of solar variability and to characterize and understand the Sun's interior and the various components of magnetic activity (Scherrer et al. 2012). It is designed to measure the intensity, Doppler shift, line of sight magnetic field (B_{los}), and vector magnetic field (vector magnetogram) using 6173 Å Fe absorption line at the surface of the Sun. Dopplergram and B_{los} have a cadence of 45 s and the vector magnetogram has a cadence of 720 s. All the data have spatial resolution of 1 arcsec. Like its predecessor Michelson Doppler Imager (MDI), it is a filtergraph which takes a sequence of images at different wavelengths and polarizations to derive the physical parameters.

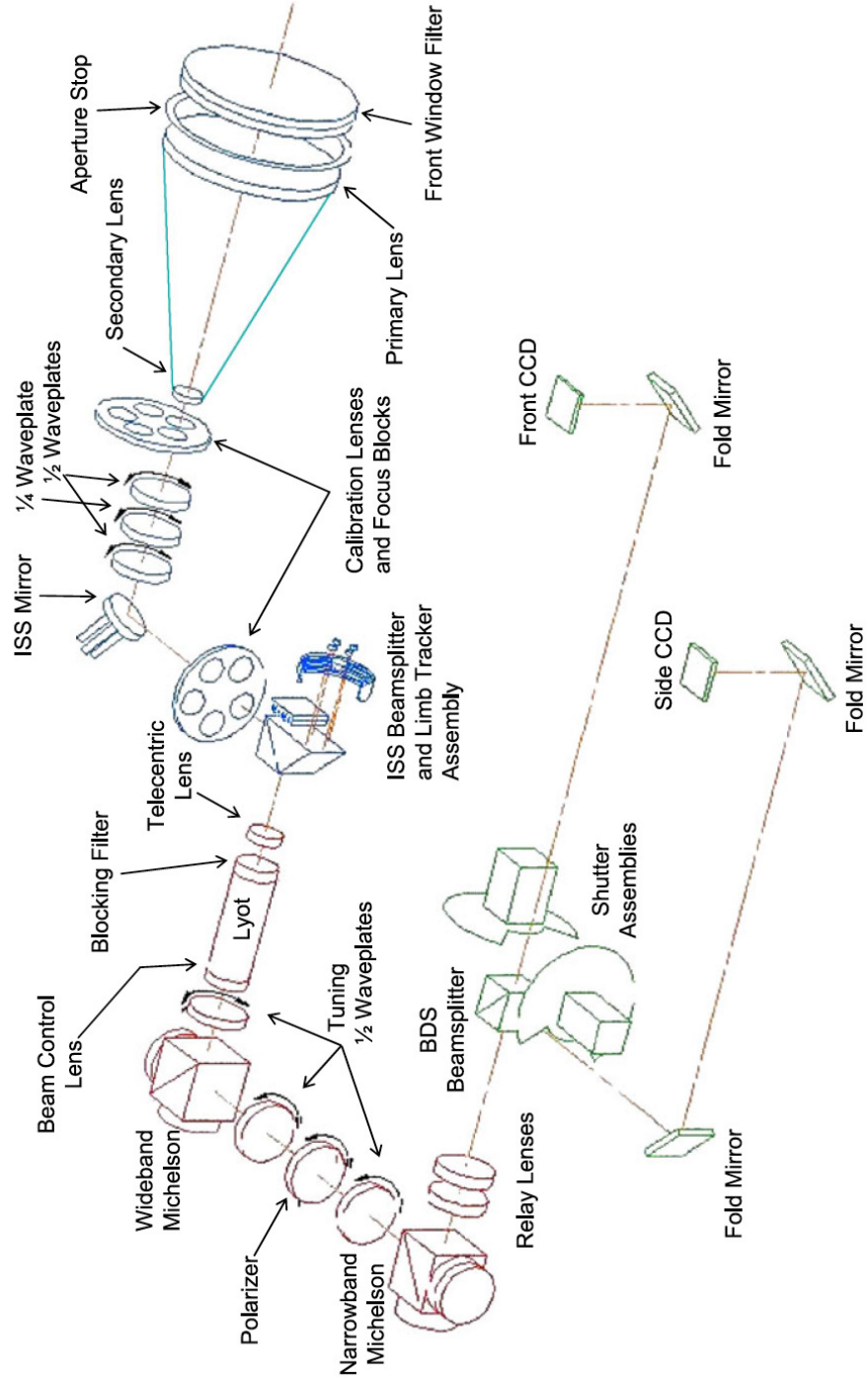


Figure 2.2: Schematic of HMI optical layout. Figure is taken from Schou et al. (2012).

The HMI instrument is made of three principal parts: an optics package, an electronic box, and a harness to connect the two. Figure 2.2 shows the schematic of the HMI optical layout. It consists of a front-window filter, a telescope, a set of waveplates for polarimetry, an image-stabilization system, a blocking filter, a five-stage Lyot filter with one tunable element, two wide-field tunable Michelson interferometers, a pair of 4096 x 4096 pixels cameras with independent shutters, and associated electronics. The key properties of the HMI are listed in Table 2.1.

Effective “sampling” of magnetically sensitive line Fe I, in order to have instantaneous full disk images at narrow passbands, is possible through the HMI filter system. The HMI filter system consists of the front window, a blocker filter, a Lyot filter with a single tunable element, and two tunable Michelson interferometers. The front window is a 50 Å bandpass filter with the primary purpose to limit the heat input to the instrument. The blocking filter is a three-period, all-dielectric, interference filter with 8 Å bandpass. It blocks the unwanted orders of the Lyot and Michelson filters and controls the heat input into the oven. The next component of HMI filter system, Lyot filter, has five elements (named E1 to E5) which have bandpass of 1:2:4:8:16 order (starting at 0.69 Å). The final filters are two wide-field, tunable Michelson interferometers with 172 mÅ and 86 mÅ passbands. The tuning of these two is done by the rotation of a combination of a half-wave plate, a polarizer, and a half-wave plate. A 76 mÅ bandpass is the final result of the rotating retarder wave plates. This can be tuned over a range of 680 mÅ around the spectral line of Fe I at rest. A model of the transmission profiles of the resulting filter is shown in Figure 2.3. All filters, except the front-window filter, are mounted in a precisely temperature-controlled oven designed to maintain a temperature stable to 0.01 C hour⁻¹.

Following the oven is the Beam Distribution System (BDS), a beam splitter that feeds two identical shutters and is mounted at a pupil image, and the CCD camera assemblies at the focal plane.

In order to reject unwanted reflections, quarter waveplates are included in a number of places. Depending on the path through the Michelsons (and counting multiple traverses of

the same element), light can traverse in total of 80 or 84 elements and can be reflected seven or nine times. The data from the CCDs are compressed and encoded and are downlinked without further processing.

The direct observables are a set of 12 narrow bandpass images of the solar disk, each of which is obtained with a different combination of wavelength tuning and polarization direction. One of the cameras measures right and left circular polarization at each wavelength at every 45 s to complete the set of 12-filtergram. These are used to produce Doppler velocity, B_{los} , and intensity map of the Sun. The second camera measures six polarization states ($I \pm V$, $I \pm Q$, and $I \pm U$) every 135 s. These combinations of polarization states are then used to produce the full Stokes vector i.e. I, Q, U, and V at a cadence of 12 minutes. Vector magnetic field and other plasma parameters are obtained from the Stokes vector by solving an inversion problem with the Milne-Eddington approximation. This approximation assumes that all physical quantities relevant to line formation are constant with optical depth (e.g., Unno 1956). Inversion of the Zeeman splitting to infer the magnetic-field component has an inherent 180° ambiguity in the component of the field perpendicular to the line-of-sight (Harvey 1969). Over the years many methods have been proposed to resolve this issue (see Metcalf et al. 2006 for an overview).

The HMI pipeline uses a variant of the minimum energy method developed by Metcalf 1994 to disambiguate the vector data (see Hoeksema et al. 2014). The HMI observables are routinely calculated through the HMI data pipeline system at Stanford University (Hoeksema et al. 2014) and are publicly available at <http://hmi.stanford.edu/magnetic/> in different mappings, such as in helio-projective (the native to the observations CCD image projection) and in a Cylindrical Equal Area (CEA) projection onto a cartesian plane (i.e. heliographic) by preserving the pixel size.

The geosynchronous SDO has a varying orbital velocity (± 3 km/s), relative to the Sun, from local dusk (~ 1 UT) to dawn (~ 13 UT). Therefore, there is a Doppler shifting of the Fe I line about its rest wavelength by about one tuning step every 12 hours. In addition, due to the fixed velocity pattern of solar rotation, the inverted magnetic field over the Sun's disk

Table 2.1: The HMI instrument characteristics. Table is taken from Schou et al. (2012).

<i>Component</i>	<i>Specifications</i>
Target line	Fe I 6173 Å
Aperture	14.0 cm
Optical Resolution (λ/D)	0.91 arcsec
Pixel size	0.505 arcsec
CCD detector	Two 4096×4096 pixels, $12 \mu\text{m}$
Front window FWHM	50 \AA
Blocking filter FWHM	8 \AA
Lyot design	1:2:4:8:16
Untuned FWHM	612 m\AA
Tunable elements FWHMs	86 m\AA Michelson
	172 m\AA Michelson
	344 m\AA Lyot
Final filter FWHM	76 m\AA
Spectral resolution	81
Polarization	All
Filtergram cadence	3.75 seconds per camera
	1.875 overall
Filtergram positions	6 at 69 m\AA spacing
Nominal observables cadence	45 seconds
Data rate	55 Mbit s^{-1}

has temporal and spatial variation in every 24 hours (see Hoeksema et al. 2014). Also, the noise level in low and moderate field strength regions changes as a function of center-to-limb angle and orbital velocity. This causes the variation of the number of pixels contributing to the unsigned-flux and consequently a symmetric peak centered $\sim 60^\circ$ from the central meridian is observed (see Figure 2.4).

2.1.2 The Atmospheric Imaging Assembly

The AIA focuses on the evolution of the Sun’s magnetic environment, and its interaction with embedded and surrounding plasma (Lemen et al. 2012). It is designed to study the short and long-term characteristics of the Sun’s dynamic magnetic field and the corresponding coronal response. It gives an uninterrupted viewing of the Sun for months with high signal-to-noise ratio and full thermal coverage of the corona. The full thermal coverage of

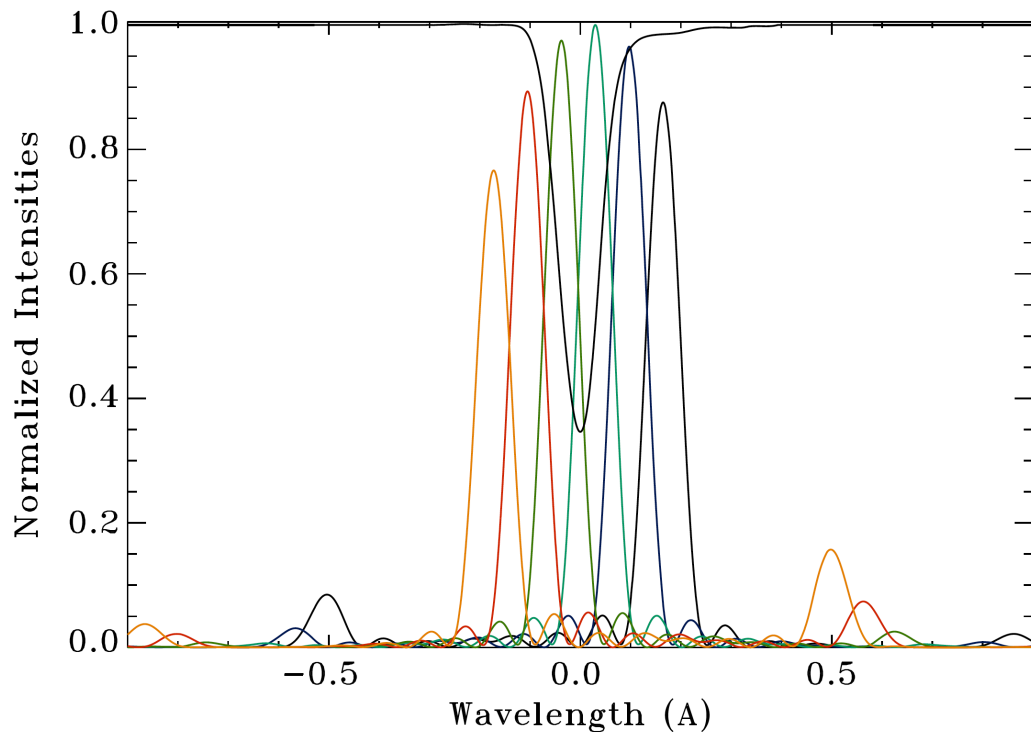


Figure 2.3: Example of HMI tuning-position profiles obtained through the wavelength-dependence calibration procedure. Colored lines show the six tuning position with respect to the Fe I solar line with no doppler shifting at the disk center. The line spacing of the tuning positions is $76 \text{ m}\text{\AA}$. Figure is taken from Schou et al. (2012).

AIA provides high-resolution full-disk images of the transition region and solar corona (up to $0.5 R_{\odot}$ above the solar limb) with 12 s temporal and 1.5 arcsec spatial resolution.

The AIA consist of four 20-cm generalized Cassegrain telescopes, optimized to observe narrow bandpasses in the EUV, in order to observe solar emissions from the transition region and corona (see Figure 2.5). Each AIA f/20 telescope has a 20-cm primary mirror and an active secondary mirror. Table 2.2 has listed the key parameters of the telescope. The design of the telescope prevents charged particles from reaching the CCD, and the aperture pupil is located by a mask that is mounted in front of the primary mirror. The multilayer coatings on the telescope mirrors are optimized for the selected EUV bandpasses. Telescopes 1, 2, and 4 have two different EUV bandpasses, whereas the mirror of telescope 3 has a 171 \AA band pass on one half and the other half has a broad-band UV coating (see

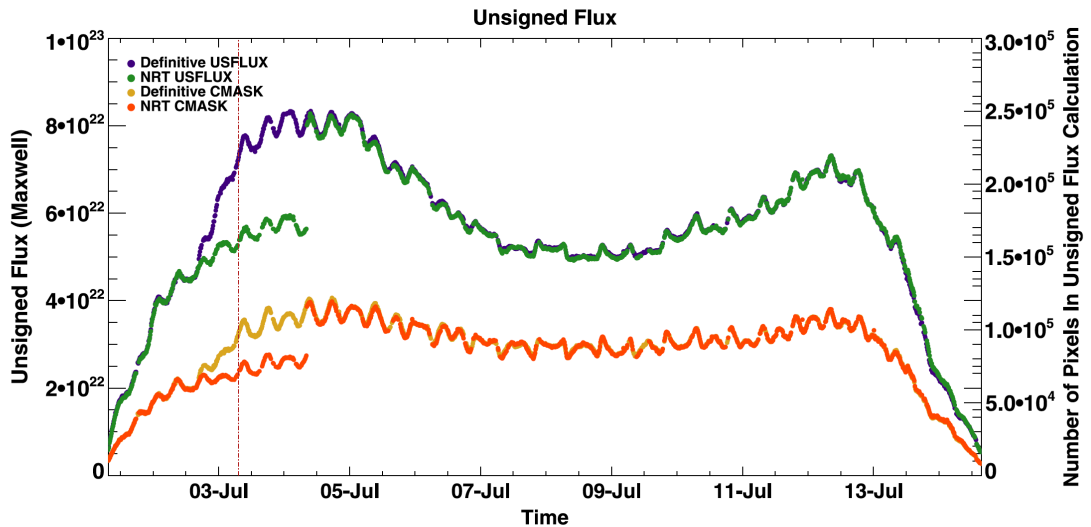


Figure 2.4: Plot of the total unsigned flux (USFLUX) calculated on an area containing NOAA ARs 11785, 11787, 11788 with CEA B_z data from SDO/HMI (blue and green curves). Also shown is the number of high confidence pixels (yellow and red curves). Note the appearance of 12-hour periodicities or undulations in the magnetic flux and the total number of high-confidence pixels due to systematic effects. The broad peaks in total unsigned flux are due to increased noise in the magnetic field measurements away from disk center (~ 60 from central meridian). Figure is adapted from Hoeksema et al. 2014.

Figure 2.5). To track the Sun continuously, each telescope has its own guide telescope which provides an error signal to its image stabilization system.

Each telescope contains a front door, a focus mechanism, a filter wheel, and a shutter mechanism. In addition, telescope number 2 has an aperture selector. Figure 2.6 shows the cross-sectional view of AIA telescope number 2 and its guide telescope. The front door is designed to protect the entrance filters during launch from debris and from acoustic loads.

The aperture selector in telescope number 2 enables only one-half of the aperture to be exposed at one time. This is required to select between 193 \AA and 211 \AA . Both of these bandpasses require aluminum filters, therefore an aperture selector is necessary. The other telescopes use only filter wheel for the selection of the filter for the desired bandpass. The narrow-band imaging of seven extreme ultraviolet (EUV) bandpasses centered on the following lines: Fe XVIII (94 \AA), Fe VIII, XXI (131 \AA), Fe IX (171 \AA), Fe XII, XXIV (193 \AA),

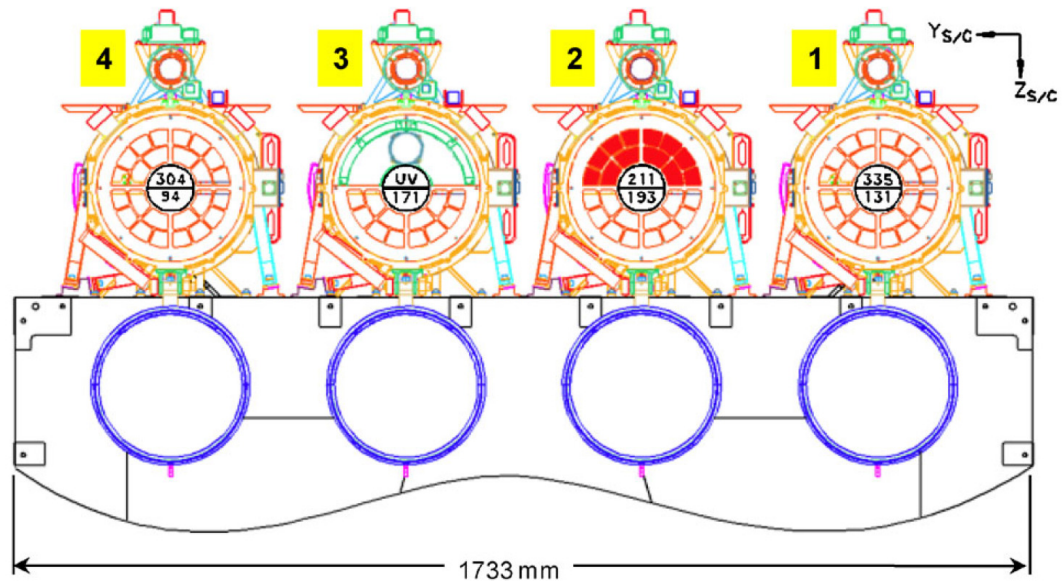


Figure 2.5: The layout of the bandpasses in each of the four AIA telescope. Telescope 2 has an aperture blade to select between wavelength channels. The other telescopes rely on filters in filter wheels to select between channels. The top half of telescope number 3 has a MgF_2 window with a coating centered at 1600 \AA . Figure is taken from Lemen et al. (2012).

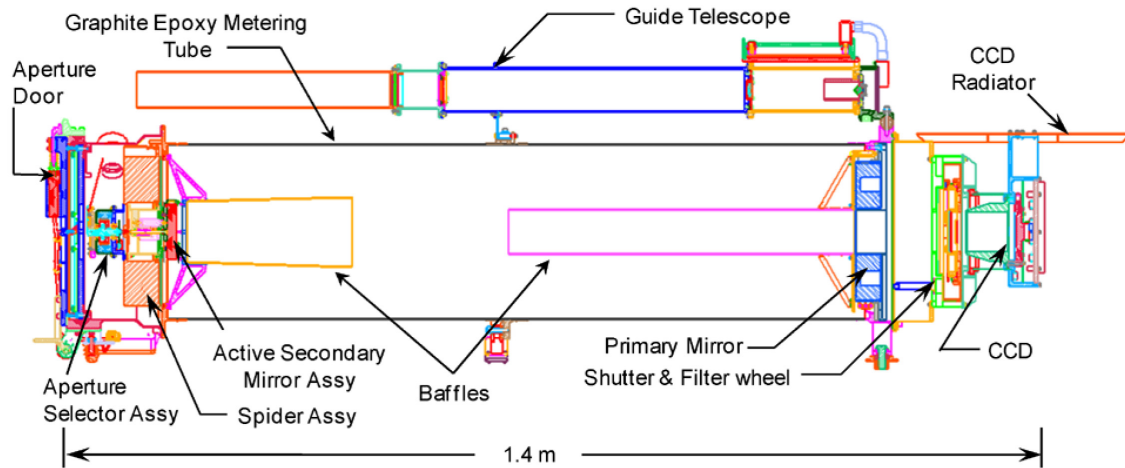


Figure 2.6: A cross sectional view of telescope number 2 of AIA. All four telescopes of the AIA have their own guide telescope to stabilize the image on the CCD. Figure is taken from Lemen et al. (2012).

Table 2.2: The AIA instrument characteristics. Table is taken from Lemen et al. (2012).

Component	Specifications
Mirrors	Multilayer-coated Zerodur
Primary diameter	20 cm
Effective focal length	4.125 m
Field of view	41 × 41 arcmin (along detector axes) 46 × 46 arcmin (along detector diagonal)
Pixel size/Resolution	0.6 arsec/1.5 arcsec
CCD detector	4096 × 4096, thinned, back-illuminated
Detector full well	150000 electrons
Effective pointing stability (with image stabilization system)	0.12 arsec RMS
Cadence(Full-frame readout)	
All telescope	8 wavelengths in 10- 12 seconds
Typical exposure times	0.5 - 3 seconds
Science Telemetry	
Interface to spacecraft	67 Mbps
Ground capture	~ 2 Tbytes (uncompressed) per day

Fe XIV (211 Å), He II (304 Å), and Fe XVI (335 Å). Besides EUV, telescope number 3 also observes C IV (near 1,600 Å) and the nearby UV continuum (1,700 Å) and has a filter that observes in the visible light (4,500 Å) to enable coalignment with images from other telescopes. Table 2.3 list the primary ions for each bandpass. Figure 2.7 illustrates the response function for the six EUV bandpasses that are dominated by iron emission lines.

The focus mechanism of each telescope adjusts the position of the secondary mirror with respect to the primary along the optical axis by up to $\pm 800 \mu\text{m}$ in $2.2\text{-}\mu\text{m}$ steps. The focus can be adjusted as often as every exposure if necessary. The shutter mechanism consists of a 159-mm diameter thin blade mounted to a motor. The blade rotates to open the shutter, exposing the CCD.

The AIA is designed to operate in a systematic, synoptic fashion, and is expected not to make frequent changes in the observing program. The original baseline observing program acquires a full-frame EUV image and one UV or visible-light image every 12 s. Each telescope is able to acquire two images in 12 s, thus eight full images are acquired in every 12

Table 2.3: The primary ions for each passband observed by AIA. Table is taken from Lemen et al. (2012).

Channel	Primary ion(s)	Region of atmosphere	Char. log (T)
4500 Å	continuum	photosphere	3.7
1700 Å	continuum	temperature minimum, photosphere	3.7
304 Å	He II	chromosphere, transition region	4.7
1600 Å	C IV + continuum	transition region, upper photosphere	5.0
171 Å	Fe IX	quiet corona, upper transition region	5.8
193 Å	Fe XII, XXIV	corona and hot flare plasma	6.2, 7.3
211 Å	Fe XIV	active-region corona	6.3
335 Å	FXVI	active-region corona	6.4
94 Å	Fe XVIII	flaring corona	6.8
131 Å	Fe VIII, XXI	transition region, flaring corona	5.6, 7.0

s. At the baseline 12 s cadence, the data acquisition exceeds the AIA telemetry allocation by a factor of 2.2. This necessitates the use of onboard compression. The AIA has two data compression/high-speed interface cards, this performs the data compression and then transmits the compressed data to the spacecraft interface. The data are then transmitted continuously to two SDO ground stations located near White Sands, New Mexico. Data from the data center are transferred to the Stanford University campus where the Level 0 data are permanently archived in the JSOC science-data processing facility.

In this section, we discussed the data and instruments mainly used in our study of ARs. The ARs and solar eruption events were selected after the analysis of a catalog. The following section discusses the creation of the catalog and some important statistics of ARs and flares.

2.2 Active Region Catalog

ARs are distinguishable as dark patches in white light images, strong magnetic concentration in magnetogram images, and as bright loops in EUV images of the Sun. Each AR is identified by a unique number given by the NOAA. We made a catalog of all the ARs that appeared from 2010 to 2015. To make this catalog we used the following data:

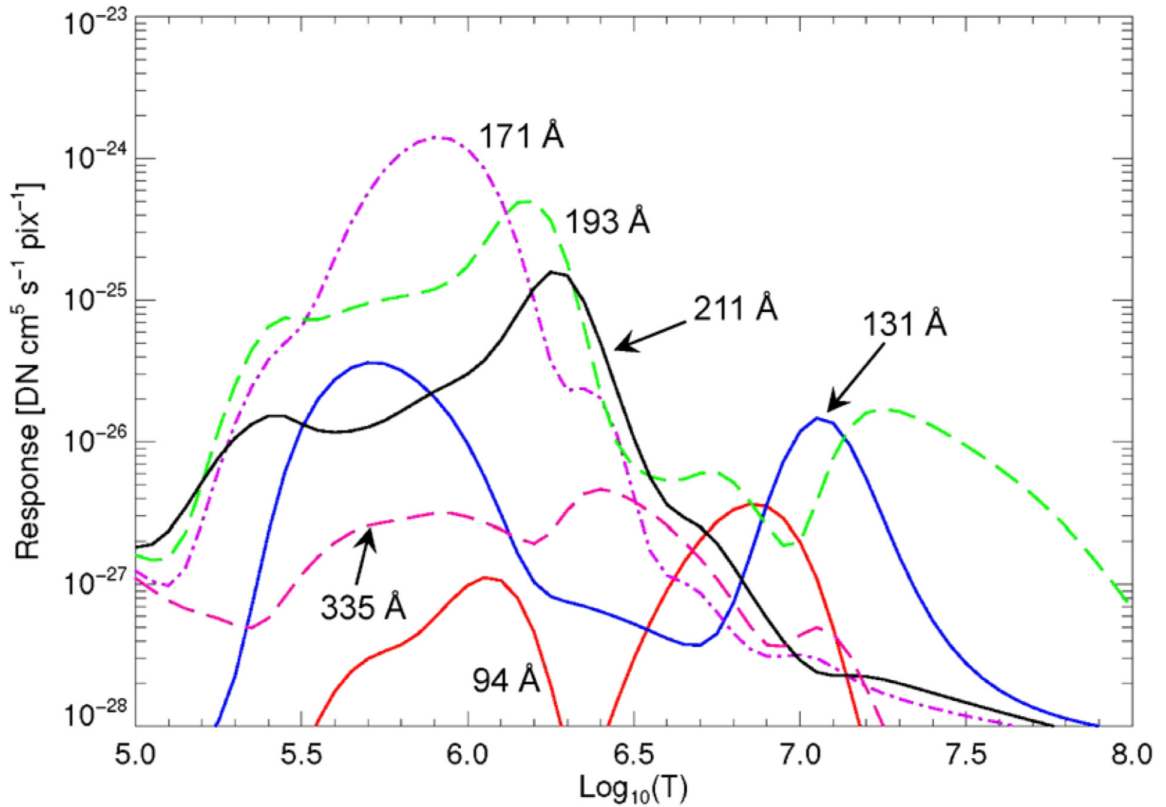


Figure 2.7: Temperature response functions for the six EUV passbands of AIA. These are dominated by iron emission lines, calculated from the effective-area functions and assuming the CHIANTI model for the solar emissivity. Figure is taken from Lemen et al. (2012).

i) **Solar Region Summary (SRS)**: SRS provides a detailed daily description of ARs observed on the solar disk during the preceding day. The Space Weather Prediction Center (SWPC) releases it daily, at 00:30 UT, after the analysis and compilation of all individual reports from the U.S. Air Force (USAF) the Solar Optical Observing Network (SOON). It has location, sunspot area, and magnetic configuration of each AR observed on the solar disk.

ii) **GOES flare list**: This list provides the information of flares observed by GOES satellite. It has information about the starting time, peak time, end time and class of the flare as observed by the GOES in soft X-ray (SXR) intensity profile. A flare event is considered ended when the current flux reading returns to half the peak flux value. Based

on the peak SXR flux, flares are classified as X, M, C, B, and A classes with flux 10^{-4} , 10^{-5} , 10^{-6} , 10^{-7} and 10^{-8} Wm^{-2} respectively.

iii) **Solarsoft latest event list:** This is another flare list compiled by the Lockheed Martin Solar & Astrophysics Laboratory (LMSAL). It is updated daily and provides a list of flares within certain time range. Further, it provides the class, location, and the associated AR of a flare.

The above mentioned sources provide the data on a daily or monthly basis. The flare lists are arranged in the order of flare's origin time. Though all the information of flares is available, except for some particular flares or ARs, they are not easy to analyze. Therefore, we extracted and arranged the information of ARs separately to form a catalog. The catalog has all the important parameters regarding ARs viz. location, area, flares, number of days it was visible, daily sunspot size, and magnetic-configuration of the sunspot.

During the period of six years, 1437 ARs appeared on the front disk of the Sun, either by rotation from the back-side or through new-emergence. This catalog has covered around half of the solar cycle 24 (December 2008 - April 2020). From 2010 to 2015, the number of ARs increased and reached to the maximum in 2014 (see Figure 2.8). This was consistent with the phase of the solar cycle 24. The yearly average sunspot size, calculated using the maximum sunspot size of the ARs, also seems to follow the solar cycle phase (see table 2.4). In total, there were 11969 flares in the span of six years (this includes A, B, C, M, and X class flares). The total number of flares per year also increased with the solar cycle phase (see Figure 2.8). Around the same numbers of ARs were appeared on the northern (710) and southern (726) hemisphere with an average sunspot size of ~ 129 in millionths of the solar hemisphere (MSH) and ~ 138 MSH respectively. In the same period, 5881 flares were recorded on the northern and 6088 flares on the southern hemisphere. Overall there was symmetry between the northern and southern hemispheres in terms of number of ARs, average sunspot size, and flares.

In comparison with B (3996) and C (7251) class flares, there were far fewer M (672) and X (45) class flares. In general, the number of flares increased with the number of ARs.

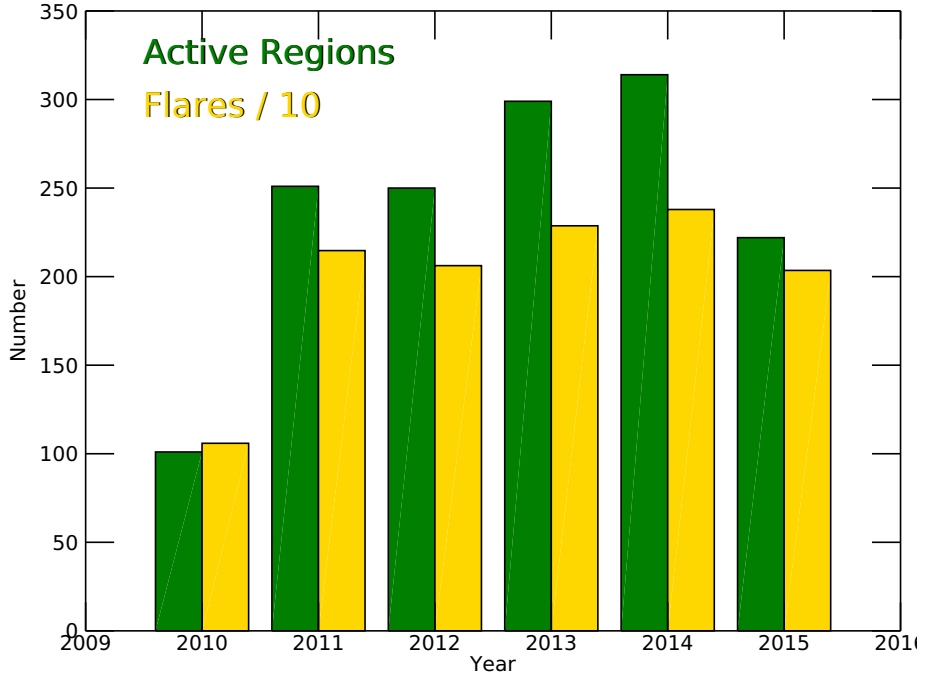


Figure 2.8: The number of ARs and flares from the Sun during the period of 2010-2015.

However, intense flares (M and X class flares; particularly X class flares) do not seem to follow this rule (see Table 2.4).

In addition to the above mentioned parameters, we calculated and assigned Flare Index (FI) to each AR to reflect their average flare-activity. The calculated FI depends on the intensity and the number of the different classes of the flares as:

$$FI = FI_{int} + FI_{num}, \text{ where} \tag{2.1}$$

FI_{int} is the FI based on the intensity of flares and FI_{num} is the FI based on the number of flares. They are calculated as:

Table 2.4: Yearly variation of Active Region number and flares. *sunspot area in millionths of the solar hemisphere (MSH).

Year	2010	2011	2012	2013	2014	2015
ARs	101	251	250	299	314	222
Flares	1059	2147	2062	2287	2379	2035
C Class	146	1191	1232	1454	1886	1342
M Class	16	105	114	104	205	128
X Class	0	8	7	13	15	2
Sunspot size (MSH*)	101	134	139	126	159	115

$$FI_{int} = \frac{(10 \sum_i X_i + 1 \sum_i M_i + 0.1 \sum_i C_i)}{T} \quad (2.2)$$

Where, X_i (or M_i/C_i) and N_X (or N_M/M_C) are the intensity class and number of X-class (or M/ C-class) flares and T is the total number of days AR was visible on the front disk of the Sun.

$$FI_{num} = \frac{(3N_X + N_M + N_C/3)}{T} \quad (2.3)$$

where, N_X (or N_M/M_C) is the number of X-class (or M/ C-class) flares.

FI based on the intensity of the flares was used before to compare the flare activity level (Abramenko 2005). As the number of flares produced by ARs is also important, we added the FI_{num} in FI. FI quantifies the averaged daily flare activity of an AR and thus makes it easy to compare the flare activity among ARs.

The right panel of Figure 2.9 shows the scatter plot of the sunspot area vs. FI of all the ARs. The AR 12192 had exceptionally large area (2750 MSH) and FI (22), therefore it is not shown in Figure 2.9. To differentiate the changes in flare productivity with different evolutionary phases and to identify the physical mechanism for the intense flares we needed to compare the evolution of ARs for a long period of time, possibly having both emerging

and decaying phases of ARs. Certain ARs like ARs emerging near the western limb of the Sun, decaying ARs, and ephemeral (small area) ARs did not satisfy such requirements. ARs on the western solar limb are visible only for a few days, due to solar rotation. Further, the true magnetic configuration of an AR is hard to determine on the solar limb due to projection effects. The lifetime of ephemeral regions is a few days and they may not have the same origin as of larger ARs (see van Driel-Gesztelyi & Green 2015 and references therein). Also, decaying ARs in their last stage may only have a single sunspot and be visible for a few days. Therefore, to exclude the above mentioned ARs the following selection criteria were set: a) area greater than 50 MSH, b) FI greater than 0.5, c) the AR was visible for more than 7 days. Only 228 ARs met the selection criteria with the average FI ~ 2.24 and area ~ 403 MSH. The left panel of Figure 2.9 shows the scatter plot of sunspot area and FI of ARs satisfying the selection criteria. The vertical and horizontal lines divide the entire plot in the following four sub-regions (see the right panel of Figure 2.9):

- **sub-region I:** ARs with small sunspot area (< 700 MSH) and small FI (< 4). Most of the ARs belong to this sub-region, in total there are 185 ARs in this sub-region.
- **sub-region II:** ARs with large sunspot area (≥ 700 MSH) and small FI (< 4). Fewer ARs belong to this sub-region, a total of 13 ARs.
- **sub-region III:** ARs with large sunspot area (≥ 700 MSH) and large FI (≥ 4). Relatively greater number of ARs belong to this sub-region, compared to sub-region II. In total there are 20 ARs in this sub-region.
- **sub-region IV:** ARs with small sunspot area (< 700 MSH) and large FI (≥ 4). Fewest ARs belong to this sub-region, in total there are 10 ARs in this sub-region.

The boundaries separating different sub-regions are fixed arbitrarily to facilitate grouping of ARs for further investigation. ARs above the horizontal line in Figure 2.9 are SAARs with bigger FI and ARs below it are LAARs with small FI. ARs on the right side of the vertical lines (see Figure 2.9) are larger ARs and on the left side are smaller ARs. It is

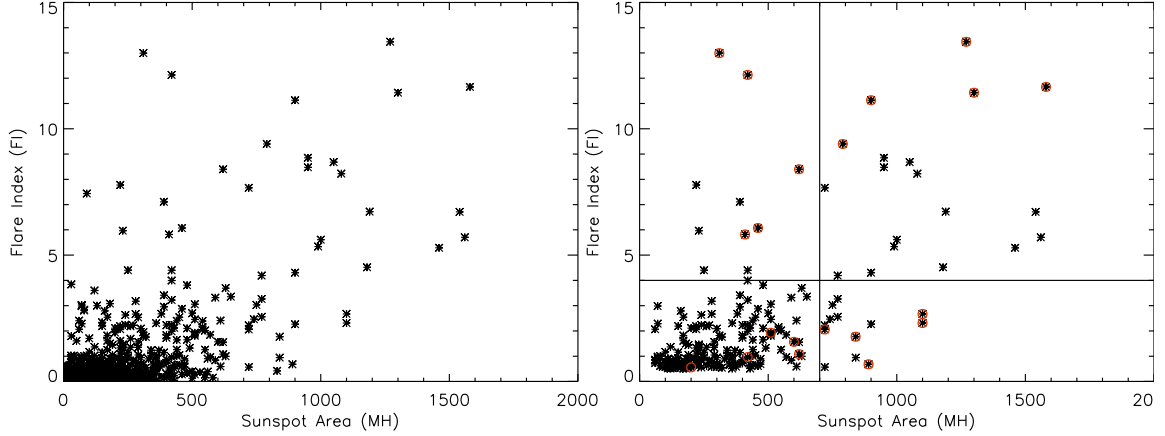


Figure 2.9: Plots of sunspot area versus flare-index. The left panel shows the scatter plot for all the ARs in the catalog. The right panel shows the scatter plot for the AR satisfying the selection criteria. ARs selected for the comparative study are circled in red.

important to note that the usage “large” and “small” is relative. Comparing the number of ARs on both sides, it is clear that large ARs are rare. The correlation between the sunspot area and FI of ARs satisfying selection criteria is 0.72. Such a moderate correlation suggests that flare productivity increases with sunspot size. However, ARs in sub-region II (ARs with large sunspot area and small FI) and sub-region IV (small sunspot area and large FI) deviate from the expectation that the flare productivity should depend on the size/ magnetic flux content of the ARs. To understand what essentially determines the flare productivity in an AR, we selected five ARs from each sub-regions randomly (circled in red in Figure 2.9) and analyzed their evolution in detail. The following chapter (Chapter 3) presents the comparative study of these ARs.

Chapter 3: Evolutionary Differences between Super-Active and Low-Active Active Regions: A Statistical Analysis

ARs are the main sources of solar flares. Considering energy budget, the probable source of flare energy is stored magnetic energy. Magnetic energy is stored in the non-potential structures of ARs and such structures can form at certain regions within ARs. For many decades, solar physicists are intrigued in the study of ARs to understand the mechanisms of energy storage. Another problem they are tackling is to know when and how stored magnetic energy is released from ARs.

ARs are identified as areas of magnetic flux concentration of opposite polarities. The life cycle of an AR begins with the emergence of magnetic flux (emergence phase) and ends with the disappearance of magnetic flux (decay phase) from the photosphere. The size/ magnetic flux content and flare activity rate vary among ARs. Depending on the size of ARs, the emergence phase can last for hours to days and the decay phase lasts for days to several weeks (see van Driel-Gesztelyi & Green 2015 and reference therein). One of the most debated issues regarding the origin of flares is whether the intensity and frequency of flares depend on the emerging twisted magnetic tube structures or the surface evolution of magnetic fluxes. Choudhary et al. (2013) found that flare activity is higher during the emergence phase of ARs. The rapid emergence of new magnetic flux and overall reconfiguration of the magnetic fields can lead to higher flare productivity (e.g. Choudhary et al. 1998). Schrijver (2007) believed that the emergence of a current-carrying magnetic field causes most of the major flares. However, in some cases flare activity increases only during the course of simplifying of magnetic morphology (e.g. Patten & Hagyard 1986). Chintzoglou et al. (2019) believe that the shearing motion and flux cancellation causes the major flares in ARs. So, the question is whether the new flux emergence is always associated

with higher flare activity. If not, when and how new emergence increases the flare activity in an AR?

Major flares are believed to correlate with the size (e.g., Yang et al. 2017), complex polarity patterns like δ -configuration (e.g., Shi & Wang 1994), anti-Hale magnetic configuration (e.g., Tian et al. 2002), and long PILs (e.g., Vasantharaju et al. 2018a). Besides these observational features, it would be helpful to quantify the magnetic nonpotentiality of ARs to understand the flare productivity. Using photospheric magnetic field data many magnetic field parameters are calculated and used to analyze the nonpotentiality and flare productivity of ARs. For example, total magnetic flux content (e.g., Yang et al. 2017), length of strong-gradient PIL (e.g., Vasantharaju et al. 2018a), magnetic shear (e.g., Leka & Barnes 2007), and R-value (e.g., Schrijver 2007). These magnetic field parameters, calculated at the photosphere, may not give the true condition of the solar atmosphere (Leka & Barnes 2003). Nevertheless, some of such parameters are considered a good indicator to predict flares from the ARs. Mostly, such parameters are used to predict the intensity of flares, can they also be used to predict the frequency of flares from the ARs?

In this study, we addressed the issue why certain ARs produce multiple intense flares than others? Here, we analyzed and compared twenty ARs having different sizes and flare productivity. Sizes of the ARs were based on the maximum size of the sunspot and the FI was used to compare the flare productivity among the ARs. Further, we compared many magnetic field parameters between SAARs and LAARs. The chapter is structured as follows. The data and methodology are described in Section 3.1. Selection of ARs for the study is discussed in Section 3.2. Evolutions of ARs are compared in Section 3.3. Quantification of flare drivers is discussed in Section 3.4, and results and discussion are presented in Section 3.5.

3.1 Data and Methodology

We used high time-cadence and high spatial resolution observation taken by the HMI instrument, onboard the SDO spacecraft (Schou et al. 2012), to analyze the evolution of ARs. The HMI instrument provides line-of-sight magnetograms (B_{los}) at a cadence of 45 seconds and spatial resolution of $1''$. In addition, we also used full vector magnetogram data, provided by the HMI team, at a cadence of 12 minutes.

We analyzed the evolution of ARs by using 2D cut-outs of HMI/ B_{los} . The cut-outs were prepared in a number of steps: 1) Rotation of AR to a reference frame. The reference frame was chosen when AR was on the central meridian position. The rotation minimized the projection effects and also removed the solar rotational effects. 2) A rectangular cut-out was prepared from the rotated data. The rectangular area of the cut-out was fixed in such a way that it contained the AR all the time. The cut-outs were then corrected for the longitudinal line-of-sight effect. 3) The final step of this process was to change the cut-out from the heliographic coordinate system to the Cylindrical Equal Area (CEA) system. In the CEA coordinate system, each pixel has equal area. Here, each pixel has an area of 0.03° .

In addition to 2D cut-out maps, we used the 3D time-image stacking method to analyze and compare the evolution of ARs. At the optimal cadence of 45 s, HMI provides 1920 full-disk images of the Sun every day. Thus, tracking and comparison of the evolution of ARs for several days is a herculean task. In order to compare the overall evolution of different ARs we adopted the method of time-image stacking of the 2D HMI data. In this method we stack the 2D cut-out of ARs in the order of time; starting from the initial cut-out, other cut-outs are placed beneath it as time progress. The HMI cut-out gives the 2D information of AR's magnetic configuration, the time-image stacking adds a new dimension (time) to give the 3D information or the evolution of ARs. In the past time-image stacking method has been used to study the emerging structure of the flux tube (e.g., Leka et al. 1996; Chintzoglou & Zhang 2013). In such cases, when the time is multiplied by the velocity

Table 3.1: Magnetic field parameters formulae.

magnetic field parameters	
parameters	calculation
Total magnetic Flux	$\Phi_{tot} = \sum B_z dA$
Net Flux	$\Phi = \sum B_z dA$
Current density	$J_z = \frac{1}{\mu_0} \sum (\frac{\partial B_y}{\partial x} - \frac{\partial B_x}{\partial y}) $
Current helicity	$H_c = \sum B_z \cdot J_z $
NC	Ratio of dominant current to non-dominant current in each polarity
sgPIL	Length of the overlapped region of opposite magnetic polarity and where gradient of $B > 150$ G/Mm
R-value	Sum of flux near sgPIL

of the emerging structure, it is considered as the vertical extent of the emerging structures. In our case, Z-axis is time and should not be confused with the real flux tube. Nevertheless, the time-image stacking method is very useful to track the motion of strong magnetic poles and to compare the overall evolution of ARs.

In this study, the HMI vector magnetograms are used to calculate physical parameters to quantify flare drivers. These parameters are calculated and analyzed at an hourly cadence from a cut-out of vector magnetograms containing the AR. The size of the cut-outs for different ARs was fixed in such a way that it contained the strong magnetic polarity of the AR throughout the observational period. Our initial FI for an AR was based on all the flares that occurred from the AR between the eastern to western solar limbs. The data quality of HMI vector magnetograms degrades considerably beyond 60° , as discussed in Chapter 2. Therefore, to compare the average flare productivity with the physical parameters, we restricted ourselves within 60° of longitude from the central meridian. The calculation of these physical parameters is explained below and summarized in table 3.1.

Magnetic flux: Our classification of ARs was based on the sunspot size and FI. The total magnetic flux is another quantitative measure of the size of an AR and are considered to be correlated with the flare productivity (e.g., McIntosh 1990). The strongest magnetic fields are concentrated at the umbra of sunspots and are radial. Therefore, we only used the z-component of magnetic field to calculate the total flux as $\Phi_{tot} = \sum |B_z| dA$. In addition to

total flux content, flux imbalance between opposite magnetic polarities are also associated with intense flares (e.g., Shi & Wang 1994). As a measure of flux imbalance we calculated the net flux as, $\Phi = \sum B_z dA$. The sum of signed flux or net flux would be close to zero in a flux balanced AR.

Current density: Magnetic reconnection, during a flare, dissipates electric current and releases magnetic energy to thermal and kinetic energies (Priest & Forbes 2002). The solar surface can have vertical currents either due to the emergence of magnetic flux through the photosphere into the corona (e.g., Leka et al. 1996) or due to the surface flow of plasma (Leka and Barnes 2003a,b). Using vector magnetogram data we calculated the vertical current density at the photosphere as $J_z = \sum |(\frac{\partial B_y}{\partial x} - \frac{\partial B_x}{\partial y})|$. The vertical current density (J_z) is one of the physical parameters that provide information about the extent of non-potentiality of ARs.

Neutralized current: In relatively force free-field plasma, the current through a flux tube (direct current) should be equal and opposite to the current flowing in the interface between flux tube and surrounding plasma (return current) (Parker 1996). Thus, the net current at the photosphere, where flux tubes emerge and are surrounded by plasma, should be zero. Net current deviates from neutrality for ARs having local magnetic shear along the sheared PILs and such ARs have higher rate of flare and CMEs (Vemareddy 2019a). In this study, we used the ratio of direct current to return current ($|DC/RC|$) as a measure of the degree of deviation from net current neutrality.

Current helicity: The magnetic helicities are the topological measure of the structural complexity of the magnetic fields (e.g., Seehafer 1990). The total helicity represents the linkages of magnetic fields i.e. the internal twist and external linking and knotting of flux tubes. The twist of magnetic fields of ARs is another parameter that the insight about the non-potentiality of ARs. Another way to estimate the twist of the field is through the calculation of current helicity (H_c). It describes the linkages of electric currents and its rapid variation is linked with the origin of flares (e.g., Bao et al. 1999). In this study, we

calculated the current helicity (unsigned) as $H_c = \sum |B_z \cdot J_z|$.

Strong gradient PIL and R-value: PIL is an imaginary line that separates the opposite magnetic polarities. The distribution and motion of magnetic fluxes around PIL are important, as shearing motion and flux cancellation form long twisted magnetic field lines and can cause solar eruption (van Ballegoijen 1982). In this study, we analyzed the strong-gradient PIL (sgPIL) of ARs. Using the HMI line-of-sight magnetogram, we first determined the bitmaps of the positive or negative fluxes. These maps were then dilated with kernels of 15×15 pixels and eroded with kernels of 5×5 pixels, to join and isolate the island of like magnetic polarities. The next step was to determine the regions where the maps of opposite magnetic polarities are overlapped with each other and where the gradient of magnetic field is greater than 150 G/Mm. We discarded the isolated PIL where the length of overlapped region was smaller than 10 pixels.

Further, we calculated the unsigned flux (R-value; in log scale) within ~ 15 Mm of sgPIL. R-value is a way to quantify the compactness of magnetic fluxes around sgPIL (Schrijver 2007). To calculate R-value we multiplied the absolute value of the magnetogram with a weighting map. The weighting map was determined by taking the bitmap of sgPIL and convolving it with area-normalized Gaussian with an FWHM of 15 Mm (similar to Schrijver 2007).

3.2 Selection of ARs for Comparative Study

Nearly fourteen hundred ARs were observed between 2010 to 2015. Only 201 (~ 14 %) of ARs had intense flares (M or X-class) and out of them only 25 had both M and X-class flares. In the period of six years, 672 M-class and 45 X-class flares were detected. Considering the number of ARs having M/ X class flares, and number of M/ X class flares, it is clear that certain ARs had produced multiple intense flares during their front disk passage. For example in 2012 out of seven X-class flares in the whole year, three were from the single AR (NOAA AR 11429), and in 2014 out of fifteen X-class flares, six were from

the NOAA AR 12192. To understand the physical mechanisms that make certain ARs very flare productive, we selected five ARs having low FI and small sunspot size, five ARs having low FI and large sunspot size, five ARs having high FI and large sunspot size, and five ARs having high FI and small sunspot size (these sub-regions are described in 2.2). Table 3.2 lists the selected SAARs and 3.3 lists the selected LAARs for the comparative study. From tables, it is clear that the selected ARs cover a wide range of FI and sunspot sizes from both SAARs and LAARs. In the following section we describe the evolutionary differences between these two groups.

Table 3.2: Active regions (ARs) from super-active ARs (SAARs) group. The first row shows the NOAA AR number. The second row shows the flare index (FI) of each ARs. The third row shows the maximum sunspot size (SS) achieved by each ARs. The fourth row shows the number of days (DO) each AR was observed on the solar disk. ARs having small (large) sunspot areas are in green (yellow).

ARs	11158	11748	11928	12205	12297	11302	11429	11515	11967	11875
FI	8.4	13.0	6.1	5.8	12.1	11.4	13.4	11.1	11.6	9.4
SS	620	310	460	410	420	1300	1270	900	1580	790
DO	10	13	8	13	14	13	14	14	14	13

Table 3.3: Active regions (ARs) from low-active ARs (LAARs) group. The first row shows the NOAA AR number. The second row shows the flare index (FI) of each ARs. The third row shows the maximum sunspot size (SS) achieved by each ARs. The fourth row shows the number of days (DO) each AR observed on the solar disk. ARs having small (large) sunspot areas are in green (yellow).

ARs	11363	11430	11745	11917	12277	11654	11785	12085	12108	12209
FI	1.1	0.6	1.6	1.0	1.9	2.7	2.0	1.8	0.7	2.3
SS	620	200	600	420	510	1100	720	840	890	1100
DO	13	10	14	13	14	14	13	10	13	15

Depending on the sunspot size or flux content, the life cycle of an AR can vary from weeks to months. Since there are no instruments to observe the magnetic field on the

backside of the Sun, it is impossible to track the evolution of large ARs for their entire life cycle. Nevertheless, our selection criteria of seven days visibility of AR on the solar disk enable us to analyze the AR's evolution for a significant period. Also, the selected list has ARs that had emerged on the backside and that had emerged on the front solar disk to provide a broad understanding of the evolution of two groups of ARs (SAARs and LAARs).

3.3 Differences between SAARs and LAARs

Figures 3.1 and 3.2 show the ARs with large and small sunspot sizes respectively. The left panels of these images show the SAARs and the right panels show the LAARs. The location of C, M, and X-class flares are shown in brown, blue, and red asterisks respectively. Irrespective of the sizes, the SAARs have complex magnetic configuration, where opposite magnetic fluxes are close to each other to form a long PIL in the middle of the AR (see the left panels of Figures 3.1 and 3.2). Comparatively, the overall magnetic configuration of LAARs is simple like a magnetic bipole, where the groups of opposite magnetic poles are well separated from each other and they lack long PIL (see the right panels of Figure 3.1 and 3.2). Another striking observational difference between these groups is the location of flares. There were many intense flares from SAARs and they are mostly located around the PIL. It is important to note that Figures 3.1 and 3.2 are showing the ARs at a particular time, whereas the flares happened throughout the front disk passage of these ARs. Though the whole evolution of the ARs is not captured in one snapshot, it is clear that the intense flares were located around some particular region.

Most of the ARs, analyzed here, were emerged on the far (back) side and rotated to the front side of the solar disk. Only three ARs (AR 11158, 11928, and 12085), out of twenty ARs, were newly emerged on the front disk. New emergences of magnetic fluxes has a higher tendency to occur near the existing magnetic fluxes (e.g., Ribes & Nesme-Ribes 1993). During the observation of these ARs, new emergence of magnetic fluxes of significant magnitude had occurred in almost all the ARs (except in AR 11748, 11745,

12277, and 12209). However, new emergence was not always associated with intense flares or increase in flare productivity. The following examples of evolution in four ARs show how the new emergence can change the magnetic configuration and flare activity in ARs, these were selected from each sub-regions (discussed in Section 2.2). Two of these ARs (AR 11430 and 12108) had only C-class flares and the other two (AR 11515 and 11928) had produced multiple intense flares.

3.3.1 Evolution of AR with Small Sunspot Area and Low FI: AR 11430

The AR 11430 is from the first sub-region type, with a small sunspot size (200 MSH) and small FI (0.6). Most of the ARs ($\sim 80\%$), satisfying the selection criteria discussed in Section 2.2, belonged to this sub-region. The AR 11430 was first observed on 2012 March 5, with a simple β magnetic configuration. Table 3.4 summarizes the daily evolution of the AR, based on the catalog (described in Section 2.2). On March 6, new magnetic bipoles emerged from the side of existing magnetic bipoles (see Figure 3.3). The orientation of newly emerging magnetic poles was consistent with the Hale’s law. The separation motion of emerging fluxes led the emerging negative fluxes to move and merge with the existing negative poles. Figure 3.4 shows the evolution of ARs in the 3D map obtained from the time-stacking method. The separation motion of emerging magnetic fluxes and the merging of emerging fluxes with the existing fluxes is very clear in the 3D map. The positive (in blue) and negative (in red) polarities were well separated from each other throughout the observational period. Though small flux emergences were observed between March 8-10, however the emerging poles were not enough strong to form the sunspot. Therefore, the total sunspot area of the AR was decreasing after March 8 (see Table 3.4). The opposite magnetic fluxes diffused and came close to each other during the decay phase (see Figure 3.3-(e) and (f)).

The overall magnetic configuration of the AR 11430 was simple β configuration, where opposite magnetic polarities were well separated from each other (see Figure 3.4). The new flux emergence had occurred in such a way that there was no interaction between opposite

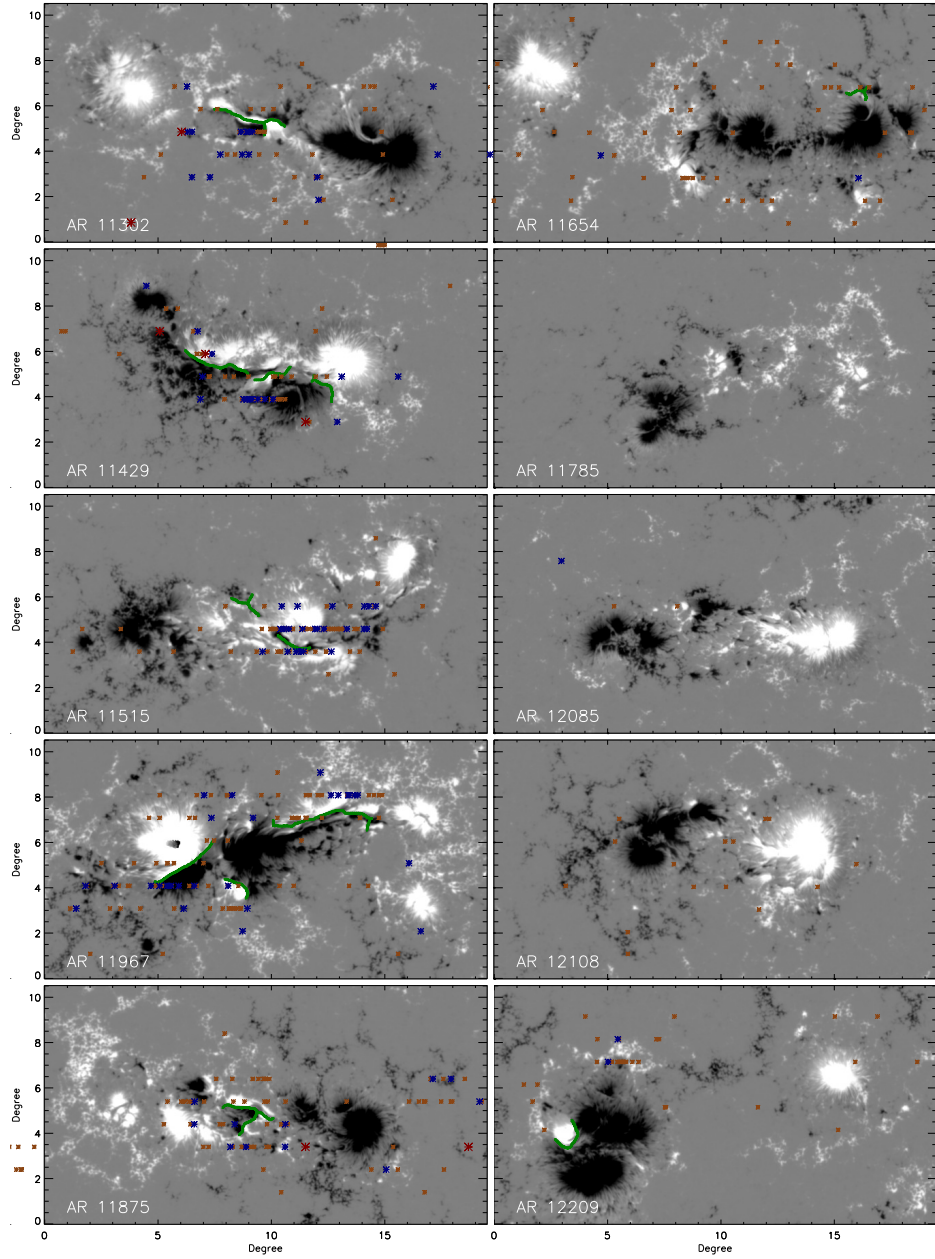


Figure 3.1: Snapshots showing the ARs, in B_{los} of HMI, with large sunspot area. The positive (negative) magnetic fluxes are shown in white (black). The left panels show the ARs with large flare productivity (SAARs). The right panels show the ARs with small flare productivity (LAARs). The location of C, M, and X-class flares (during the entire observational period) is shown in brown, blue, and red asterisks. The green lines show the location of the strong-gradient polarity inversion line.

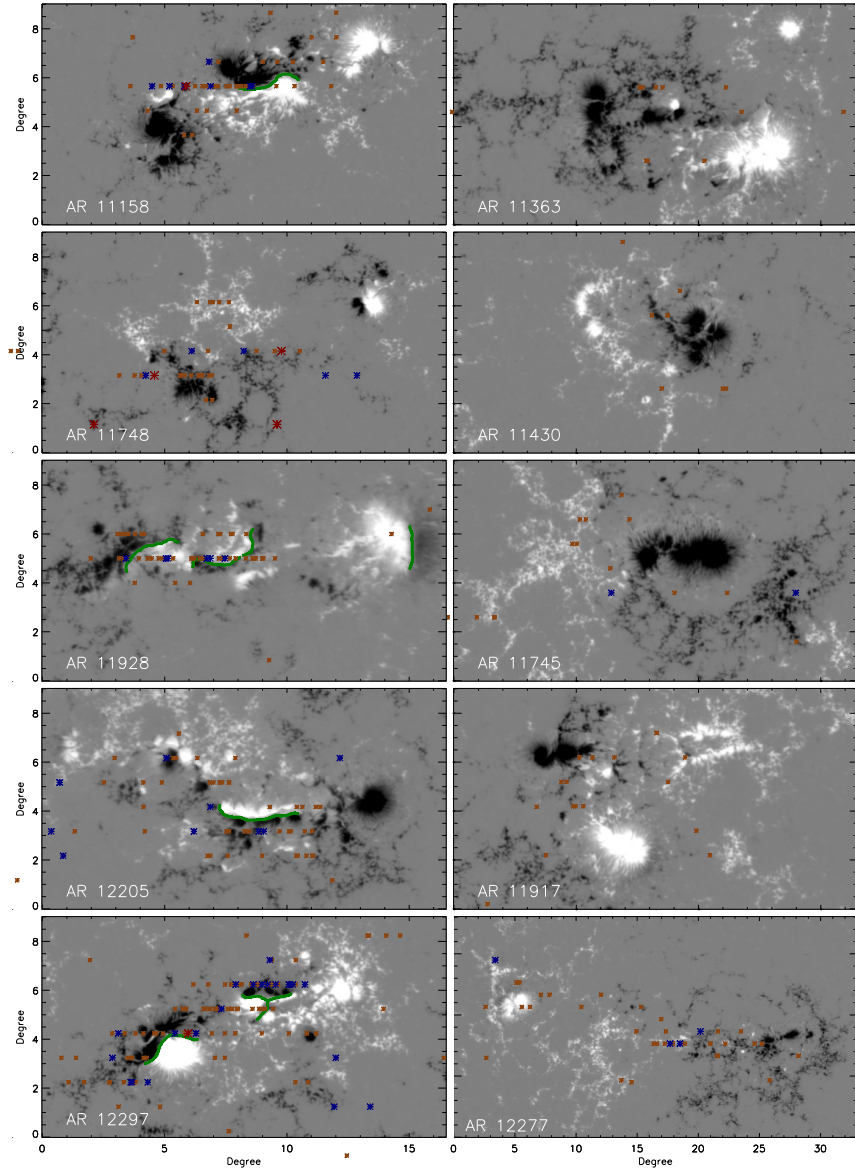


Figure 3.2: Snapshots showing the ARs, in B_{los} of HMI, with small sunspot area. The positive (negative) magnetic fluxes are shown in white (black). The left panels show the ARs with large flare productivity (SAARs). The right panels show the ARs with small flare productivity (LAARs). The location of C, M, and X-class flares (during the entire observational period) is shown in brown, blue, and red asterisks. The green lines show the location of the strong-gradient polarity inversion line.

magnetic fluxes of emerging and existing magnetic polarities. Following the emergence, the sunspot area of the AR increased and reached to maximum on 2012 March 8 (see Table

Table 3.4: Table showing the changes in the area and sunspot type during the period flares were recorded from the AR 11430. The second column is showing the changes in the area of the sunspot. The third, fourth, and fifth columns are showing the number of X, M, and C-class of flares produced by the ARs on each day respectively. The last column is showing the change in the sunspot configuration during the evolution.

NOAA AR 11430					
Date	Area (MSH)	X	M	C	Sunspot Type
2012/03/05	20	0	0	0	β
2012/03/06	90	0	0	2	N/A
2012/03/07	110	0	0	1	β
2012/03/08	200	0	0	2	β
2012/03/09	180	0	0	1	β
2012/03/10	120	0	0	1	β
2012/03/11	100	0	0	0	β
2012/03/12	100	0	0	1	β
2012/03/13	30	0	0	0	α
2012/03/14	30	0	0	0	α

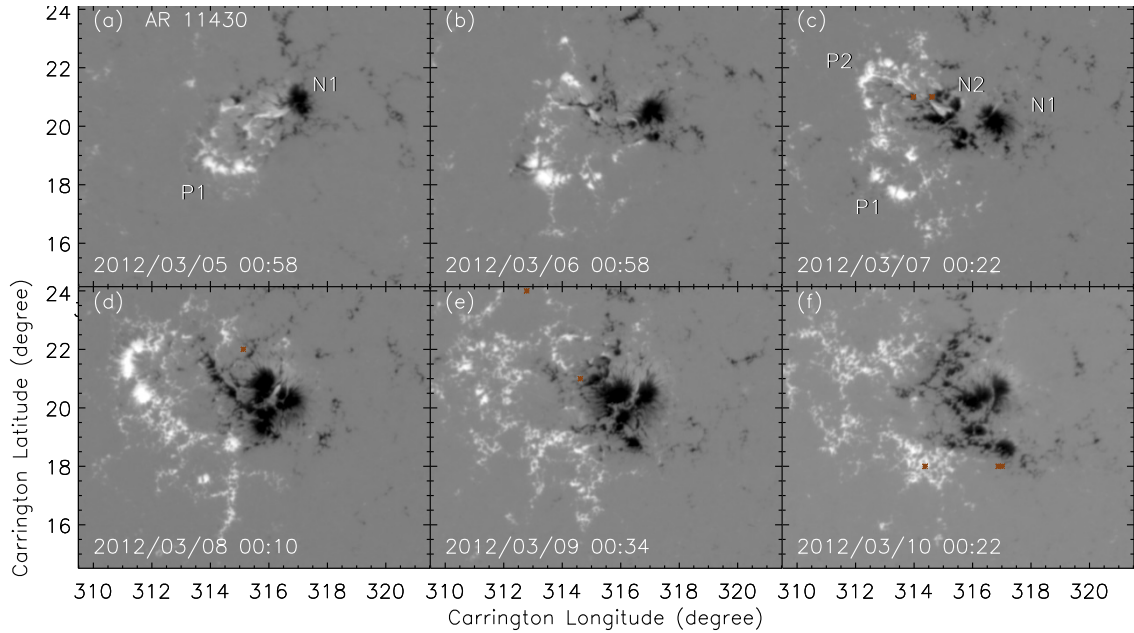


Figure 3.3: Evolution of AR 11430 as observed in the HMI line-of-sight magnetogram in the period of six days. Positive (negative) flux is shown in white (black). Locations of C-class flares are shown in brown asterisks.

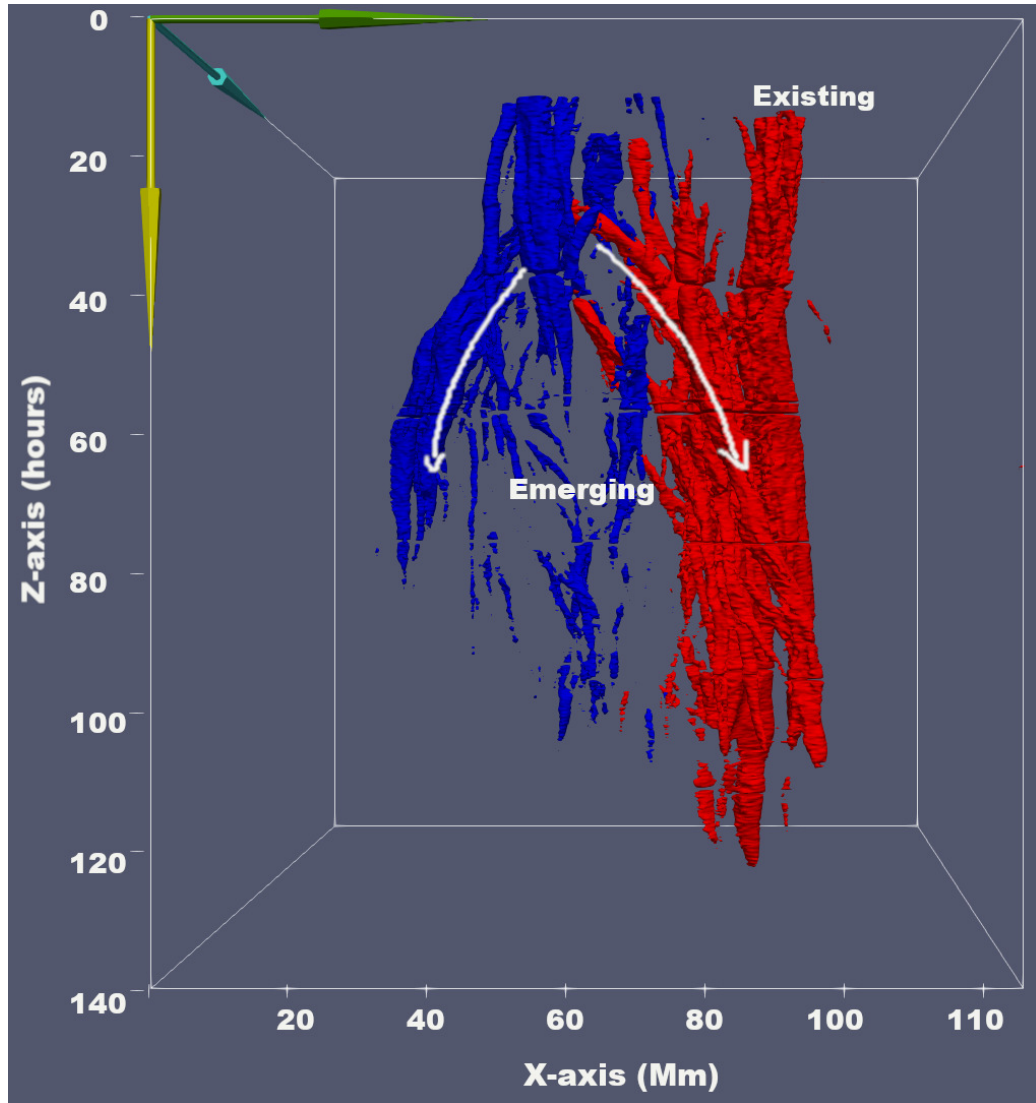


Figure 3.4: Photospheric magnetic field evolution of AR 11430 in the 3D map obtained through the time-image stacking method (discussed in 3.1). The red (blue) structure shows the contour of negative (positive) magnetic flux ($|B| \geq 800$ G) of the AR between 2012 March 6 - 12. The green, cyan, and yellow arrows show the direction of the west limb, the north pole, and time respectively. The moving magnetic poles have a slanted shape. The white arrows show the motion of newly emerging magnetic fluxes and their interaction with existing magnetic fluxes. The overall magnetic configuration of the AR is simple throughout the evolution.

3.4). After that, the sunspot area decreased. There were only C-class flares from this AR (see Table 3.4) and the flare productivity was the same both during the emergence or decay

phases.

3.3.2 Evolution of AR with Large Sunspot Area and Low FI: AR 12108

The AR 12108 is from the second sub-region, with a large sunspot area (890 MSH) and low FI (0.7). Around 5% of ARs were in this sub-region. The AR 12108 had a simple β magnetic configuration as it appeared on the eastern limb on 2014 July 1. Table 3.5 summarizes the evolution and flares from the AR 12108. On July 2, a magnetic bipole emerged (P2N2) in between the existing magnetic bipoles (P1N1; see Figure 3.5-(b)). The orientation of newly emerging magnetic poles was consistent with the Hale's law. Since the emergence was in the middle of existing magnetic bipole, the separation of emerging fluxes led the emerging positive (negative) fluxes to move and merge with the existing positive (negative) poles. There was another emergence of a small magnetic bipoles (P3N3) towards the north of P2N2 on July 4. Due to the location of emerging P3N3, their separation motion led the P3 to move toward the N2. The interaction of P3 and N2 resulted in a complex magnetic configuration ($\beta/\gamma/\delta$) of the AR for around three days. Due to the small size of P3, the interaction between opposite magnetic fluxes of non-conjugate poles (P3 and N2) was for a brief period of time. The entire evolution of AR 12108 is clearly captured in Figure 3.6.

The overall magnetic configuration of the AR 12108 was simple like β/γ configuration. Two strong negative poles were close to each other, but well separated from the positive pole (see Figure 3.6). The new flux emergence had occurred in such a way that there was no strong interaction between opposite magnetic fluxes of emerging and existing magnetic polarities. There were only C-class flares from this AR (see Table 3.5) and the flare productivity was the same both during the emergence and decay phase.

3.3.3 Evolution of AR with Large Sunspot Area and High FI: AR 11515

The AR 11515 is from the third sub-region, with a large sunspot area (900 MSH) and high FI (11.1). The evolutionary summary of the AR is in Table 3.6. It appeared on the eastern limb with a β magnetic configuration on 2012 June 28. Many episodic flux emergences of

Table 3.5: Table showing the changes in the area and sunspot type during the period flares were recorded from the AR 12108. The second column is showing the changes in the area of the sunspot. The third, fourth, and fifth columns are showing the number of X, M, and C-class of flares produced by the ARs on each day respectively. The last column shows the change in the sunspot configuration during the evolution.

NOAA AR 12108					
Date	Area (MSH)	X	M	C	Sunspot Type
2014/07/01	N/A	0	0	1	N/A
2014/07/02	30	0	0	0	β
2014/07/03	90	0	0	0	β
2014/07/04	90	0	0	1	β
2014/07/05	120	0	0	2	β/γ
2014/07/06	350	0	0	1	β/γ
2014/07/07	620	0	0	2	$\beta/\gamma/\delta$
2014/07/08	720	0	0	0	$\beta/\gamma/\delta$
2014/07/09	890	0	0	0	$\beta/\gamma/\delta$
2014/07/10	830	0	0	1	$\beta/\gamma/\delta$
2014/07/11	690	0	0	0	β/γ
2014/07/12	560	0	0	3	β/γ
2014/07/13	600	0	0	3	β/γ
2014/07/14	200	0	0	1	β/γ
2014/07/15	N/A	0	0	1	N/A

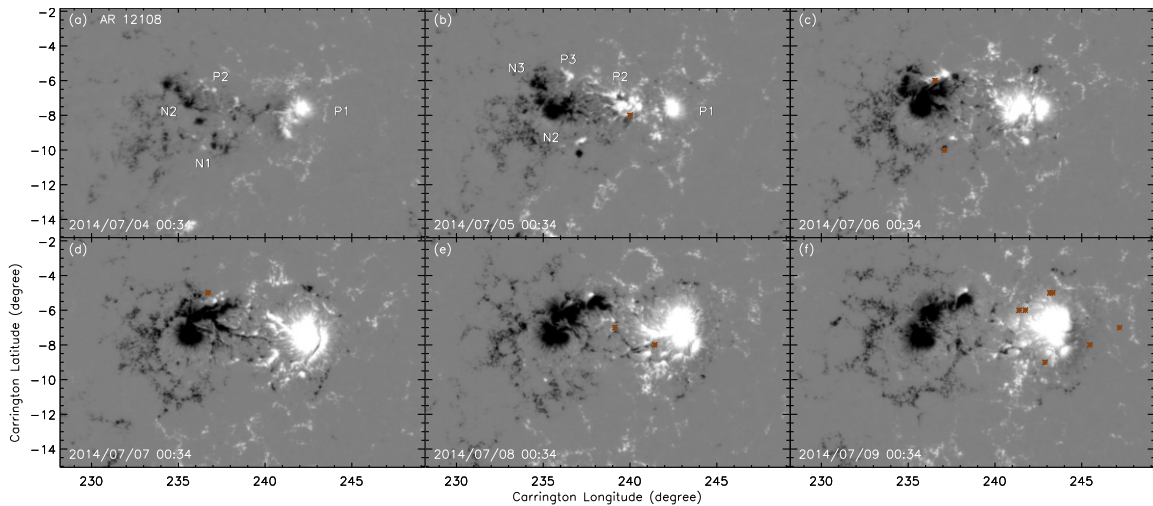


Figure 3.5: Evolution of AR 12108 as observed in the HMI line-of-sight magnetogram in the period of six days. Positive (negative) flux is shown in white (black). Locations of C-class flares are shown in brown asterisks.

new magnetic bipoles occurred in the middle of existing bipoles (P1N1) throughout the observational period. During the separation of emerging fluxes, the negative fluxes coalesce to form N2 and the positive fluxes coalesce to form P2 (see Figure 3.7). Since the negative (positive) fluxes of subsequent episodic emergence, in the middle of existing poles, merged with N2 (P2), we did not indicate them differently in Figure 3.7. These episodic emergence, in the middle of existing poles, were similar to the emergence observed in AR 11430 and AR 12108. Though episodic flux emergences observed since June 28, there were only a few C-class flares from around this region (see Figure 3.7). From the beginning of the observational period, the existing positive pole (P1) was moving towards the north-west direction.

On July 1 at $\sim 14:00$ UT new flux emergence was observed near the P1. With the continuation of new emergence, P1 is divided into two parts (P1₁ and P1₂). The emerging positive flux seemed to merge with P1₁ and the emerging negative flux moved toward the P2. P1₂ also moved toward the P2. All the emerging magnetic pairs followed the Hale's law of polarity; with the leading (following) pole being positive (negative) magnetic flux.

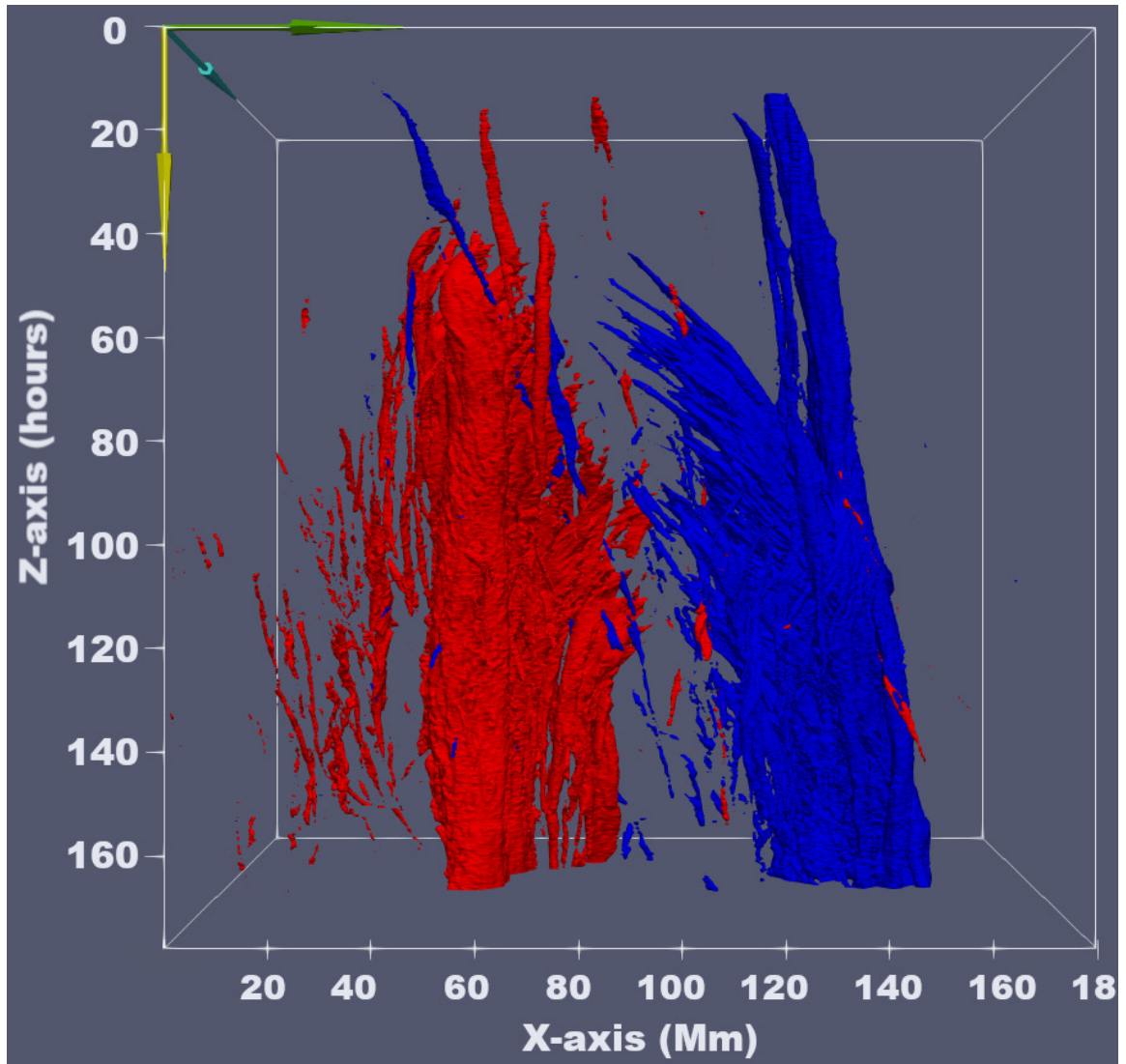


Figure 3.6: The photospheric magnetic field evolution of AR 12108 between 2014 July 3 - 11. The contour of negative (positive) magnetic flux ($|B| \geq 800$ G) is shown in red (blue). The green, cyan, and yellow arrows show the direction of the west limb, the north pole, and time respectively. Opposite magnetic poles are far from each other throughout the evolution.

Three M-class flares occurred during the emergence period near P1 and N3 (see Figure 3.7 (e)). P2, N3, and P1₂ approaches each other in the middle of the AR and a long PIL start to form by June 3 (see the third panel of Figure 3.1). Many M-class flares occurred from around this region (see panels (e)-(i) of Figure 3.7).

Table 3.6: Table showing the changes in the area and sunspot type during the period flares were recorded from the AR 11515. The second column is showing the changes in the area of the sunspot. The third, fourth, and fifth columns are showing the number of X, M, and C-class of flares produced by the ARs on each day respectively. The last column is showing the changes in the sunspot configuration during the evolution.

NOAA AR 11515					
Date	Area (MSH)	X	M	C	Sunspot Type
2012/06/28	200	0	0	1	β
2012/06/29	180	0	0	3	β/γ
2012/06/30	310	0	0	1	β
2012/07/01	380	0	0	3	β/γ
2012/07/02	850	0	3	11	β/γ
2012/07/03	620	0	0	13	β/γ
2012/07/04	570	0	5	10	$\beta/\gamma/\delta$
2012/07/05	640	0	8	11	$\beta/\gamma/\delta$
2012/07/06	670	0	2	6	$\beta/\gamma/\delta$
2012/07/07	900	0	2	6	$\beta/\gamma/\delta$
2012/07/08	780	0	4	8	β/γ
2012/07/09	550	0	0	3	β/γ
2012/07/10	320	0	0	1	β/γ

Figure 3.8 shows the evolution of ARs in the 3D map. The AR had a simple β configuration in the earlier evolutionary period (top portion of Figure 3.8). Later on, the magnetic configuration of the AR became very complex with the new emergence and interaction between non-conjugate opposite fluxes (see Figure 3.8). The negative fluxes were moving towards the left and the positive fluxes were moving towards the right. This indicated a continuous shearing motion between opposite magnetic fluxes. Along with the shearing motion, a continuous flux cancellation was observed in this region (see panels (f)-(i) of Figure 3.7). Strong shearing motion and flux cancellation were not observed in AR 11430 and AR 12108. Many of the M-class flares originated around this region (locations of flares are shown in blue asterisks in Figure 3.7).

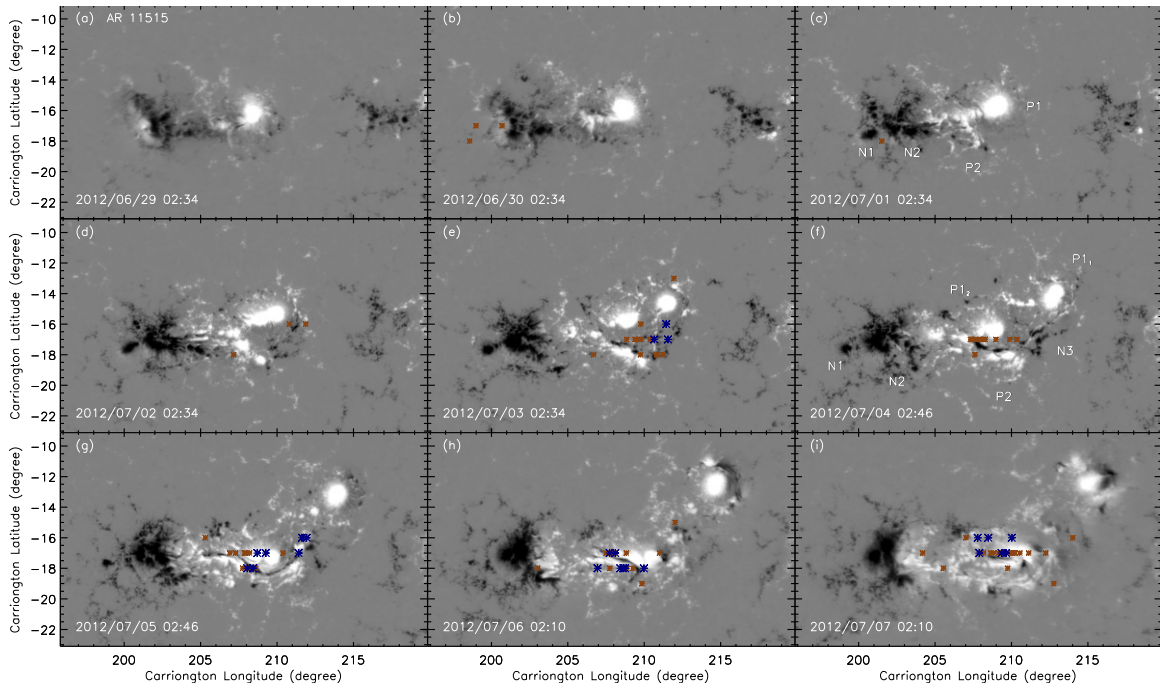


Figure 3.7: Evolution of AR 11515 as observed in the HMI line-of-sight magnetogram in the period of nine days. Positive (negative) flux is shown in white (black). Locations of C-class and M-class flares are shown in brown asterisks and green asterisks respectively.

3.3.4 Evolution of AR with Small Sunspot area and High FI: AR 11928

The AR 11928 is from the fourth sub-region, with a small sunspot area (460 MSH) and high FI (6.1). The evolutionary summary of the AR is in Table 3.7. It emerged on the front disk of the Sun. In an area of diffused negative polarity, probably of a decayed AR, a new magnetic bipole (P1N1) started to emerge on 2013 December 16, at $\sim 04:24$ UT. The coalescence of emerging fluxes resulted in a multipolar magnetic configuration on December 18 (P1, N1, and N2; see Table 3.7 and Figure 3.9). A small magnetic bipole (P3N3) emerged near P1 on December 19 (see panel (c) of Figure 3.9). Diverging from its conjugate pair P3, N3 interacted with the positive fluxes coalescing toward P1 in the middle of AR. As the interacting positive fluxes were not that strong, the interaction occurred for less than a day and there was only one C-class flare. There were many subsequent magnetic emergences after December 20; P4N4 emerged near N2, P5N5 emerged near P1 and P6N6 emerged in

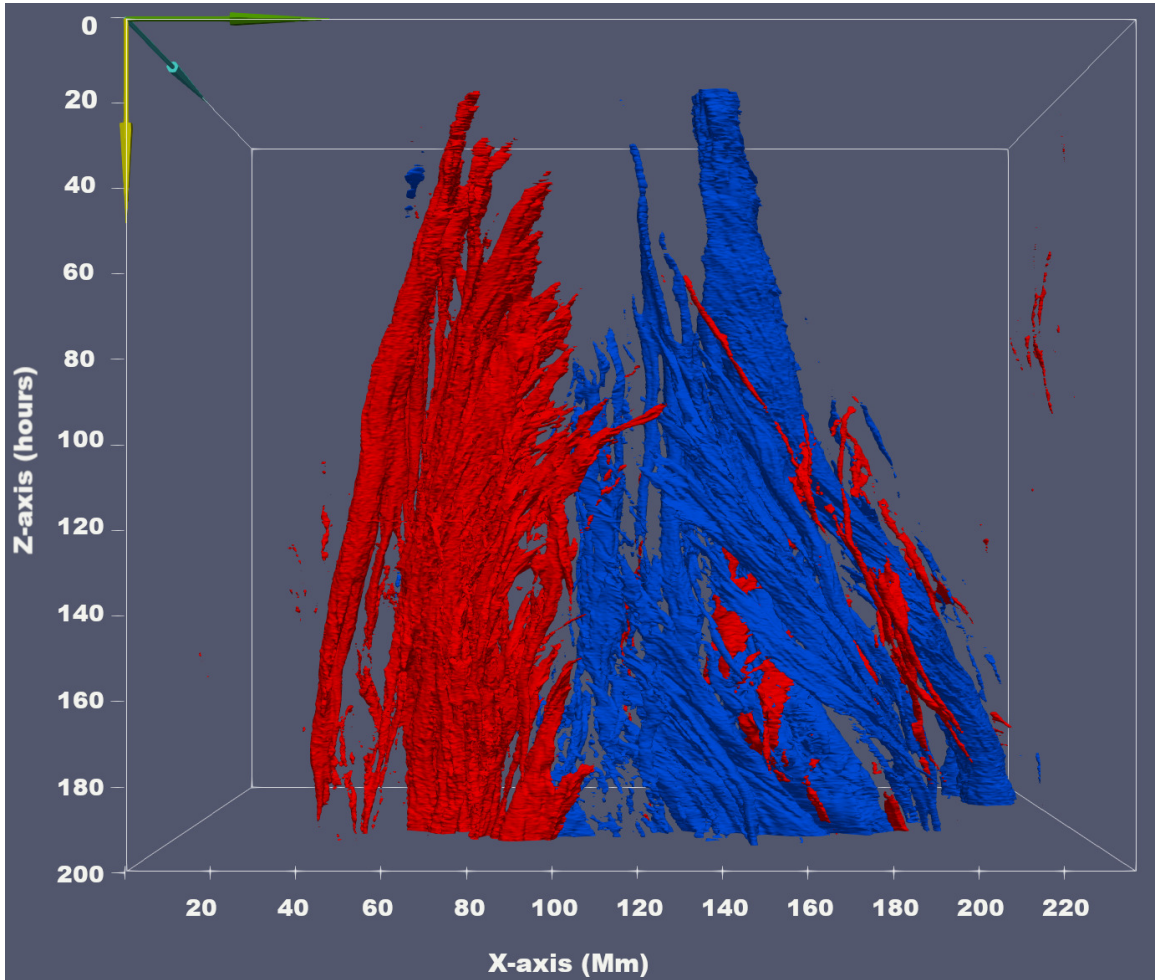


Figure 3.8: The photospheric magnetic field evolution of AR 11515 between 2012 June 28 - July 6. The contour of negative (positive) magnetic flux ($|B| \geq 800$ G) is shown in red (blue). The green, cyan, and yellow arrows show the direction of the west limb, the north pole, and time respectively. The mixed polarities in the middle show the interaction between opposite magnetic fluxes.

the middle of the AR. Except for P4N4, all the emerging magnetic pairs followed the Hale's law of polarity; with the leading (following) pole having positive (negative) magnetic flux (see Figure 3.9). The interaction between P4, P5, P6, and N5 formed a long PIL in the middle of the AR (see the third panel of Figure 3.2).

Figure 3.10 shows the evolution of ARs in a 3D map obtained from the time-stacking method. Two strong magnetic polarities were far from each other and in the middle there

Table 3.7: Table showing the changes in the area and sunspot type during the period flares were recorded from the AR 11928. The second column is showing the changes in the area of the sunspot. The third, fourth, and fifth columns are showing the number of X, M, and C-class of flares produced by the ARs on each day respectively. The last column is showing the changes in the sunspot configuration during the evolution.

NOAA AR 11928					
Date	Area (MSH)	X	M	C	Sunspot Type
2013/12/18	130	0	0	1	β/γ
2013/12/19	240	0	0	3	β/γ
2013/12/20	360	0	0	5	β/γ
2013/12/21	400	0	0	9	β/γ
2013/12/22	460	0	5	11	β/γ
2013/12/23	380	0	1	11	β/γ
2013/12/24	330	0	0	2	β/γ
2013/12/25	130	0	0	5	β/γ

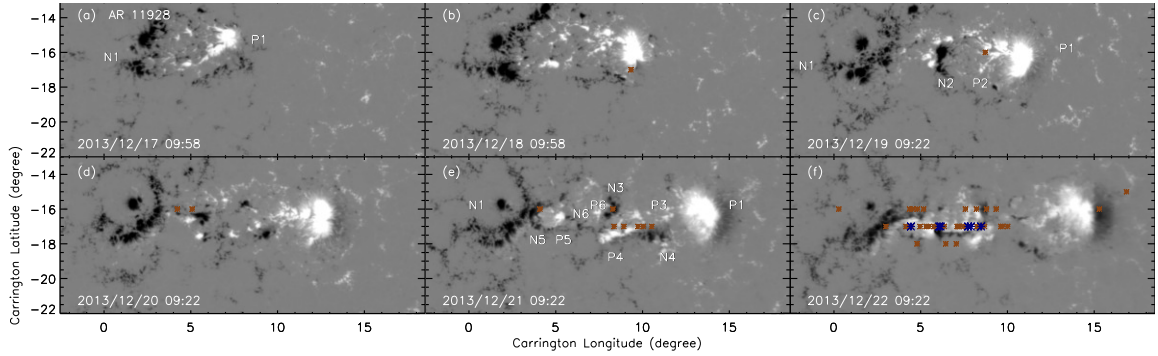


Figure 3.9: Evolution of AR 11928 as observed in the HMI line-of-sight magnetogram in the period of six days. Positive (negative) flux is shown in white (black). Locations of C-class and M-class flares are shown in brown and green asterisks respectively.

was complex mixed polarity. Shearing motion and flux cancellation of opposite magnetic fluxes were observed in the middle part of the AR. Since the size of the emerging bipoles was very small, the interaction between opposite magnetic fluxes was observed for a brief evolutionary period. Six M-class flares originated around this region.

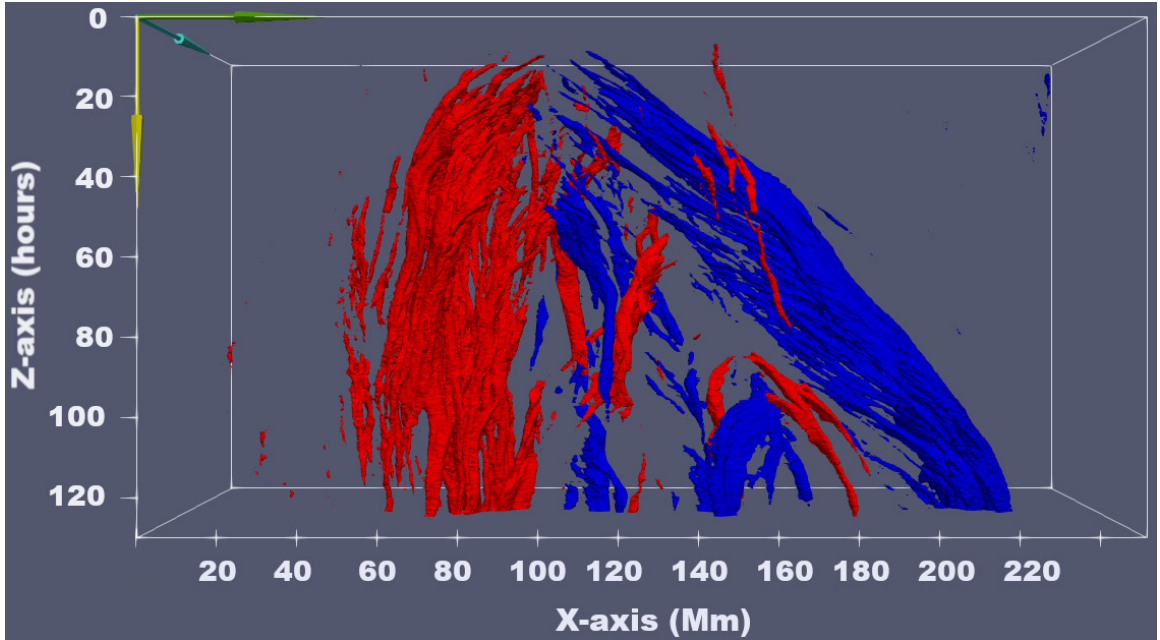


Figure 3.10: The photospheric magnetic field evolution of AR 11928 between 2013 December 16 - 22. The contour of negative (positive) magnetic flux ($|B| \geq 800$ G) is shown in red (blue). The green, cyan, and yellow arrows show the direction of the west limb, the north pole, and time respectively. The mixed polarities in the middle show the interaction between opposite magnetic fluxes.

3.4 Quantification of Flare Drivers: Magnetic Field Parameters

The above sections compared the evolution of SAARs and LAARs. To quantify the flare drivers we calculated and analyzed six magnetic field parameters (discussed in Section 3.1) within 60° of longitude from the central meridian. In the following we discuss the time-profile of these parameters with the evolution of ARs 11430, 12108, 11515, and 11928.

Total Unsigned Magnetic Flux: The top panels of Figures 3.11, 3.12, 3.13, and 3.14 show the variation in total magnetic flux in black and positive (negative) magnetic flux in blue (in red) in ARs 11430, 12108, 11515, and 11928 respectively. During the evolution of these ARs, as discussed in the above section, there were many episodic emergences. The flux emergence is clearly evident only for AR 11430 (see panel (a) of Figure 3.11), where

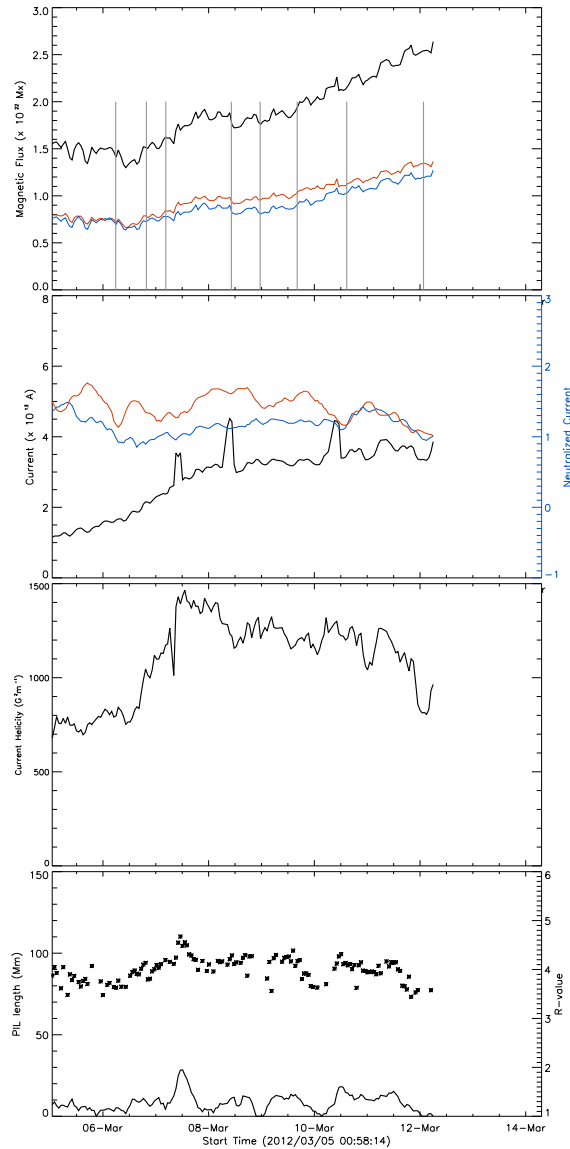


Figure 3.11: Evolution of magnetic field parameters in AR 11430. The first panel, at the top, shows the time-profile of total unsigned, positive, and negative magnetic flux in black, blue, and red respectively. The vertical grey lines show the time of C-class flares from the AR. The second panel shows the total current in black and the degree of net current neutralization in positive (negative) polarity in blue (red). The third panel shows the current helicity in black. The last panel shows the length of strong-gradient polarity inversion line (sgPIL) and R-value in solid black line and black asterisks respectively.

the emerging magnetic fluxes were significant with respect to the existing magnetic fluxes. For AR 12108, 11515, and 11928, the systematic variation due to instrument effect was

dominant i.e. decreasing (increasing) of magnetic flux as ARs moves to (from) central meridian from eastern limb (to western limb). There is no clear relation between the rate of change of magnetic flux and the flare productivity from ARs. All four of the ARs had a little imbalance of magnetic fluxes. However, it does not seem to have a relation with the flare productivity.

Current Density: Second panel of Figures 3.11,3.12, 3.13, and 3.14 show the time-profile of current density of the ARs 11430, 12108, 11515, and 11928 respectively in black. The current density of the AR 11430 increased till it reached to the maximum sunspot size on March 8, 2012, after that it decreased gradually. The current density of the AR 12108 increased gradually throughout the observational period. The current density for AR 11515 was almost constant till July 1, afterwards with new magnetic flux emergence it increased continuously. The rate of increase of current density in AR 11515 was higher than the AR 12108. The current density of AR 11928 was also increasing continuously during the observational period. However, the slope for current density was smaller than AR 12108 and 11515. Current density increased in all these four ARs, but that does not increase the flare productivity in all the ARs.

Degree of Current Neutralization: Second panel of Figures 3.11,3.12, 3.13, and 3.14 show the evolution of $|DC/RC|$ in positive (negative) polarity of ARs 11430, 12108, 11515, and 11928 respectively in blue (red). The ratio measures the degree of net current neutrality in the ARs and would be one for ARs having neutralized current. The ratio was undulating for AR 11430 and flare productivity was almost the same during rise and fall of the ratio. For AR 12108, the ratio was close to unity throughout the observational period. The flare productivity in AR 11515 increased with the rise in the value of the ratio. In AR 11928 intense flares were observed when the ratio was decreasing and approaching to unity. There is no obvious relation between the flare productivity and rate of change of the ratio.

Current Helicity: Third panel of Figures 3.11,3.12, 3.13, and 3.14 show the time profile of current helicity of ARs 11430, 12108, 11515, and 11928 respectively. Though the current helicity increased a little for AR 11430 during the new emergence around March 7, 2012,

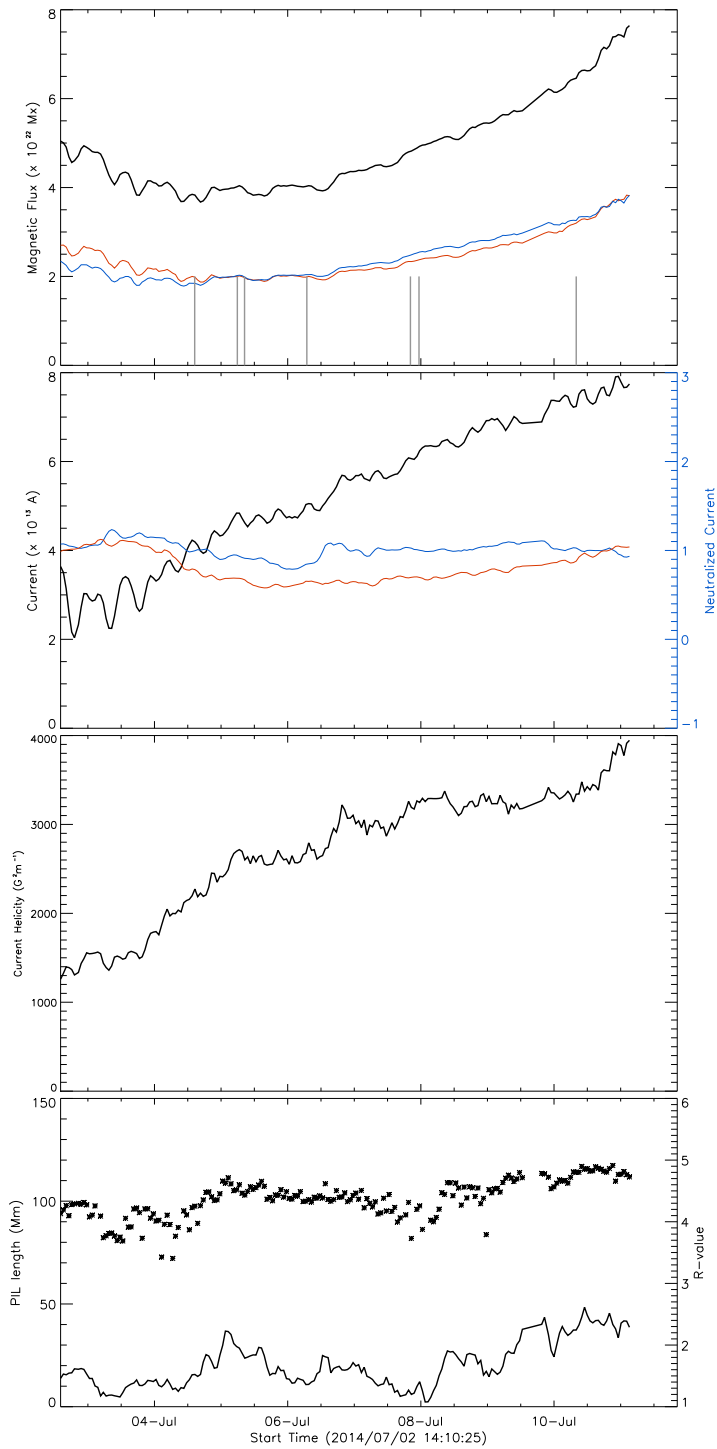


Figure 3.12: Evolution of magnetic field parameters in AR 12108. This is similar to Figure 3.11.

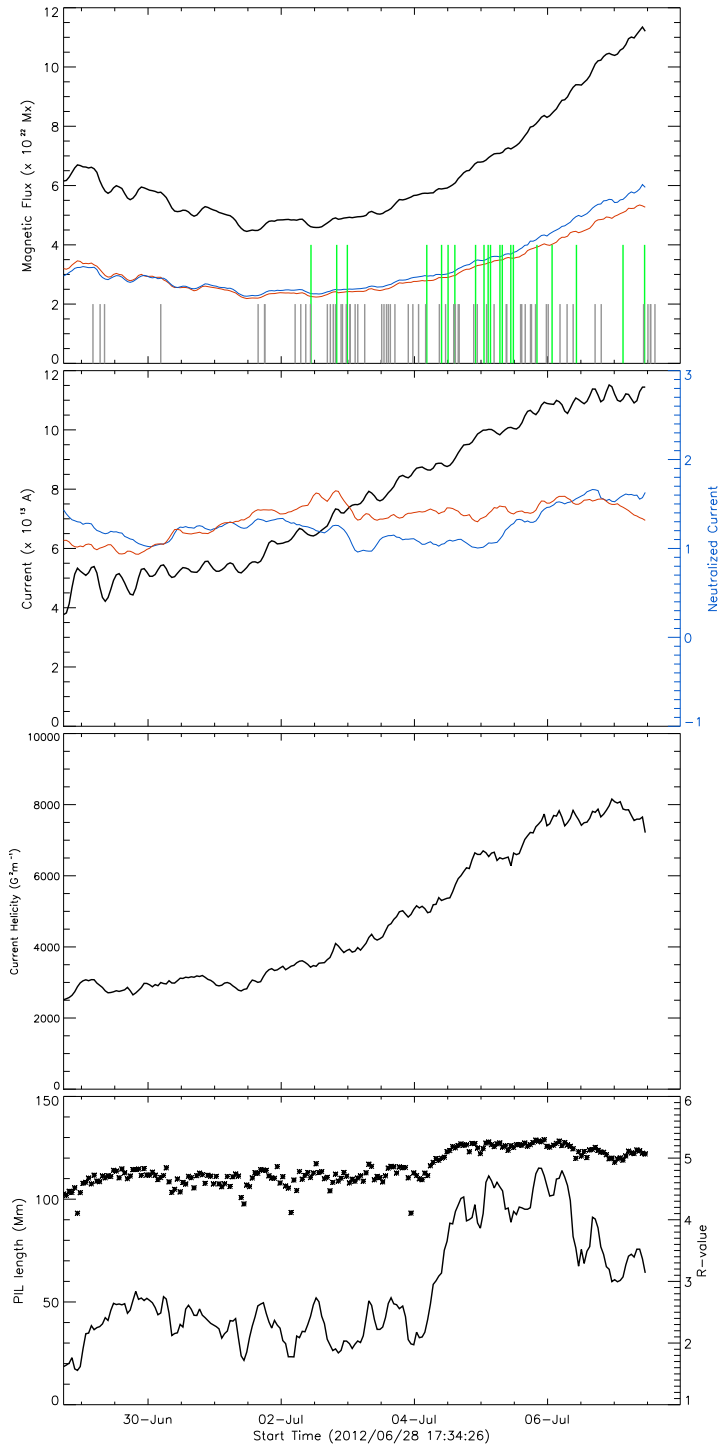


Figure 3.13: Evolution of magnetic field parameters in AR 11515. This is similar to Figure 3.11.

later on it decreased slowly. The current helicity in the AR 12108, 11515, and 11928 increased throughout the observational period, the rate of increase of current helicity for AR 11515 was much higher than that in the other two ARs. The rate of increase of current helicity and maximum value reached were similar for AR 12108 and AR 11928. This suggests that the increasing of current helicity or the magnitude of current helicity may not reflect the frequency or intensity of flares.

sgPIL and R-value: The last panels of Figures 3.11,3.12, 3.13,and 3.14 show the variation in the length of sgPIL of ARs 11430, 12108, 11515, and 11928 respectively in black solid line. The AR 11430 had a very small sgPIL (< 50 Mm) throughout the observational period. There was no considerable variation in the length of sgPIL. The AR 12108 also had a very small sgPIL (< 50 Mm) and there was no considerable variation in the length of sgPIL. Both of these ARs had small FI. The AR 11515 and 11928 had small sgPIL for the initial evolutionary period, after it had increased very much. Though there were a few intense flares in AR 11515 before the jump in the length of sgPIL, the flare rate increased very much after the jump. In AR 11928, with the jump in the length of sgPIL the number of C-class flares increased. However, there was no intense flares during the rise in the length of sgPIL. There were intense flares in AR 11928 only after the sgPIL reached to maximum value. As the R-value represents the compactness of opposite magnetic fluxes around the sgPIL, it follows a similar trend as of sgPIL.

Comparison of Flare Productivity with Average Value of Magnetic Field Parameters: Above, we compared the flare production with the rate of change of magnetic field parameters. We also wanted to know if the magnitude of the parameters has information about the flare productivity. We calculated the average of magnetic field parameters during the observational period of each AR to compare with flare productivity. ARs having the higher value of certain parameters during the observational period would have a higher value of the average of that parameter. Table 3.8 shows the average value of magnetic field parameters in each AR. The calculated FI reflects the flare productivity of ARs. Therefore, we compared the average value of parameters with the FI. Figure 3.15 shows the scatter

Table 3.8: Average value of magnetic field parameters. First column shows the NOAA AR number. Second column shows the flare index within 60° of the central meridian. Third column shows the average value of unsigned magnetic flux (USF). Fourth column shows the net flux (NF). Fifth column shows the current density (J_z). Sixth column shows the current helicity (H_c). Seventh column shows the degree of current neutralization (NC). Eighth column shows the length of strong-gradient polarity inversion line (PIL). Ninth column shows the R-value.

Average values of magnetic field parameters								
AR	FI (new)	USF (10^{22} Mx)	NF (10^{20} Mx)	J_z (Am^{-2})	H_c (G^2m^{-1})	NC	PIL (Mm)	R-value
11429	17.3	5.1	9.3	448.4	4142.6	2.4	103.6	5.0
12297	15.2	4.6	67.7	436.9	3648.7	2.4	78.0	5.0
11515	14.5	6.4	14.3	592.6	4749.6	1.3	94.4	4.9
11302	12.4	5.8	18.5	552.7	4271.7	1.3	71.9	4.9
11967	11.5	10.6	236.1	886.7	9843.7	1.6	146.0	5.3
11158	10.6	3.2	2.5	390.9	2933.6	1.6	56.6	4.8
11875	6.6	4.6	-0.2	471.1	3365.3	1.2	55.9	4.7
11928	6.5	3.8	-9.5	396.8	2734.5	1.0	64.4	4.7
12205	4.7	4.7	-67.6	450.8	3297.3	1.5	59.0	4.7
11654	3.5	7.2	4.5	605.3	4380.2	1.0	73.1	4.8
12209	3.2	11.7	-399.6	791.0	6406.8	1.1	61.4	4.8
11785	2.4	2.8	-10.7	292.6	1672.1	1.0	17.2	4.0
12277	2.0	8.1	44.3	615.3	4162.2	1.0	30.9	4.3
11748	1.7	2.0	-18.1	251.1	1450.9	2.1	17.0	4.0
12085	1.5	3.8	49.9	364.3	2424.0	1.1	36.4	4.5
11917	0.8	5.0	195.1	415.2	2439.2	1.2	19.0	4.1
11430	0.8	1.7	-8.4	219.2	1093.8	1.3	13.6	4.0
11363	0.4	4.7	-40.3	426.2	2567.3	1.1	30.1	4.3
12108	0.4	4.8	0.0	408.0	2696.9	0.9	33.5	4.4
11745	0.2	5.6	-8.6	435.2	2610.4	1.2	19.8	4.1

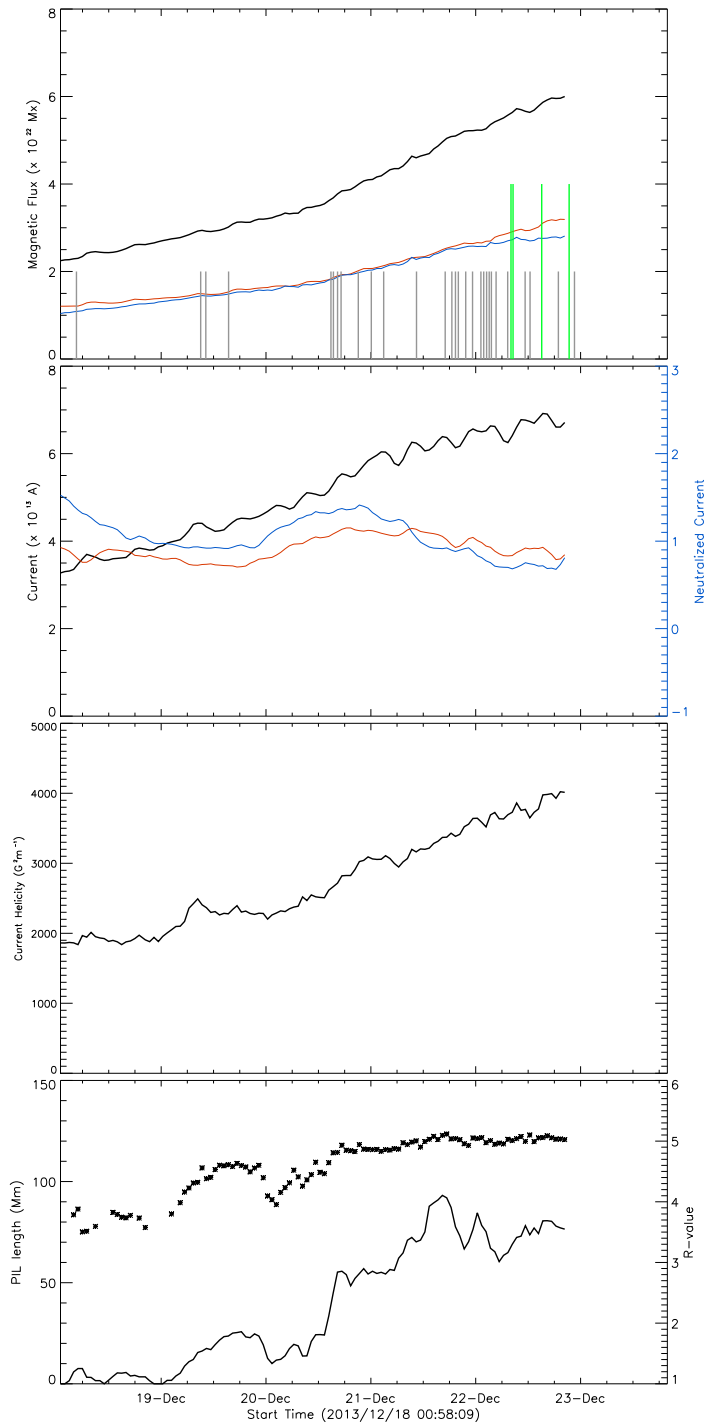


Figure 3.14: Evolution of magnetic field parameters in AR 11928. This is similar to Figure 3.11.

plots between average of magnetic field parameters and FI. Plots of neutralized current, sgPIL, and R-value are less scattered compared to the plots of magnetic flux, current density, and current helicity. Table 3.9 shows the correlation between the magnetic field parameters and FI. The correlation between FI and the average total flux content is the weakest (0.16). This suggests that big ARs do not necessarily produce intense flares and vice versa. The correlation between FI and the length of the sgPIL/ R-value is the highest (0.8). This suggest that ARs having long PIL are most likely to produce intense flares. Also, the scatter plot of the sgPIL/ R-value shows the division of ARs into two groups. ARs having sgPIL < 50 Mm (R-value < 4.5) have small FI (see Figure 3.15).

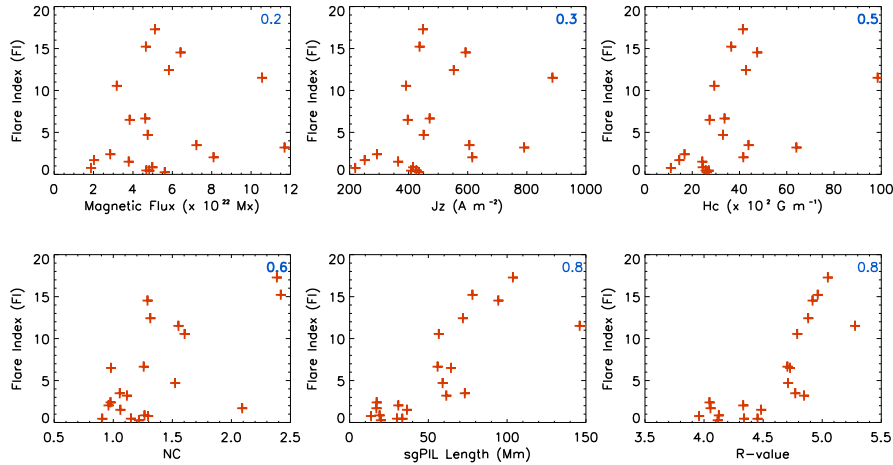


Figure 3.15: Scatter plots between magnetic field parameters and flare index (FI). The correlation coefficient between FI and parameters is on the upper right corner of each panels. The left, middle, and right upper panels show plots for total unsigned magnetic flux, current density, and current helicity respectively. The left, middle, and right lower panels show plots for deviation from degree of current neutrality, length of sgPIL, and R-value respectively.

Table 3.9: Correlation between flare indices (FIs) and magnetic field parameters.

Correlations							
Correlation	Total Flux	Net flux	Jz	Hc	NC	sgPIL	R-value
FI	0.16	0.20	0.31	0.46	0.62	0.80	0.80

3.5 Results and Discussion

In this study, we analyzed and compared the evolution of ten super-active active regions (SAARs) and ten low-active active regions (LAARs). The first goal of this study was to identify the physical processes responsible for multiple intense flares from an AR. Long strong-gradient polarity inversion lines (sgPILs) in the middle of ARs were distinctive features for the SAARs, whereas in LAARs opposite magnetic poles were far from each other. The sgPILs are one of the important observational features identified in the flare productive ARs for a long time (e.g., Zirin & Wang 1993; Vemareddy 2019a). Shearing motion and flux cancellation of opposite magnetic fluxes along the PIL are well known to produce solar eruptions (e.g., van Ballegooijen & Martens 1989). Certain studies argue that the emergence of a highly twisted magnetic flux tube can produce observational features such as long PILs and shearing motion between opposite magnetic fluxes (e.g., Tanaka 1991; Fan et al. 1999). In such scenarios, PILs and shearing motions between opposite magnetic fluxes are observed between conjugate magnetic pairs (magnetic pairs emerging together). This was not the case in our study, in most cases sgPILs were formed between the non-conjugate pairs (magnetic pairs emerging simultaneously at a different locations or at a different times). The emerging opposite magnetic fluxes move away from each other to a certain distance (generally this separation distance depends on the magnetic flux content; Wang & Sheeley 1989). If such a moving pair approaches toward the magnetic pole (pre-existing or emerging simultaneously) of similar polarity, then a long strong sgPILs can not be formed (see top panels of Figure 3.16). On the other hand, if such pair approaches toward the magnetic pole of opposite polarity, then sgPILs are formed between non-conjugate pairs (see middle and

lower panels of Figure 3.16). The separation motion of conjugate pair essentially acts as a driver of shearing motion between non-conjugate pairs, the period of interaction between opposite fluxes of non-conjugate pairs depends on the sizes of the emerging pair. If each interacting opposite magnetic polarities (of non-conjugate pair) are of considerable sizes, then the sgPILs are observed for a long period of time. Consequently, shearing motion and flux cancellation of opposite magnetic fluxes occur for a long period, and such continuation stores magnetic energy in the solar corona for repetitive flares around the PIL, which was observed for SAARs. Chintzoglou et al. (2019) studied two SAARs and suggested that shearing motion and flux cancellation between non-conjugate pairs were responsible for multiple intense flares and CMEs along the same PIL. They termed the shearing and flux cancellation between the non-conjugate pairs as collisional shearing to differentiate from the classical cancellation picture of magnetic fluxes between conjugate pairs. Our study supports their idea, where collisional shearing are observed for a much larger number of ARs and multiple intense flares observed in such ARs. Also, our study demonstrates the cases where new magnetic emergence does not result in the interaction between non-conjugate pairs. In such cases, the flare activity does not change either during the emergence or decay phase of ARs. This further supports the idea that collisional shearing is the physical process responsible for multiple intense flares from SAARs.

The second goal of this study was the quantification of flare drivers. Here, we calculated the total unsigned flux (USF), net flux (NF), current density (J_z), current helicity (H_c), degree of current neutralization (NC), length of sgPIL, and R-value to analyzed the flare productivity of ARs. The correlation between the size/ total magnetic flux content and FI, which was the weakest (0.16) among the analyzed magnetic field parameters, suggests that the size does not determine the flare productivity of ARs. As the size/ magnetic flux content of AR is determined by the size/ frequency of magnetic flux emergence, this again indicates that emergence alone does not change the flare productivity in an AR. The correlation between the length of sgPIL/ R-value and FI was the highest (0.8) among the analyzed magnetic field parameters. Long sgPILs are the indicator of complex magnetic

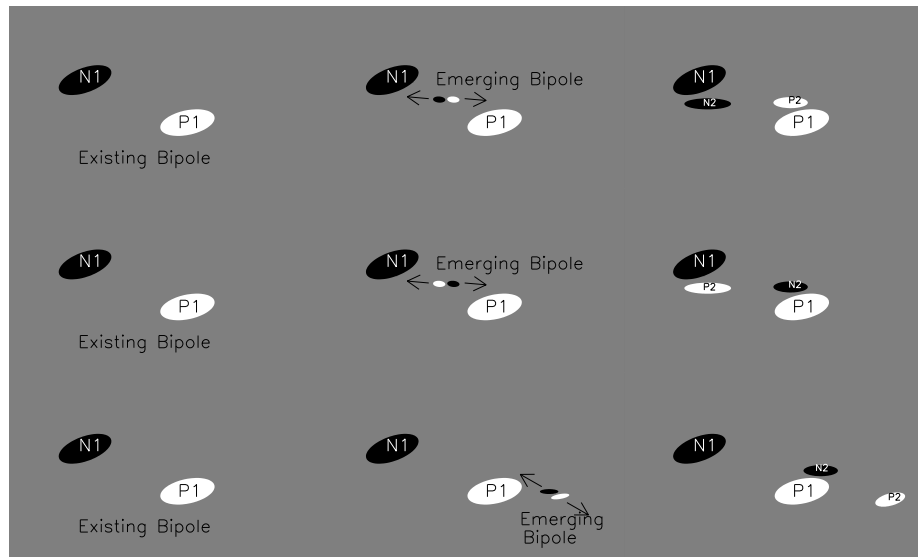


Figure 3.16: Cartoon models showing the changes in the magnetic configuration due to new magnetic flux emergence. Top panels show the case of interaction between like magnetic fluxes of emerging and existing magnetic poles. The overall magnetic configuration would be simple and flare productivity would not change in this scenario. Middle and lower panels show the cases of interaction between unlike magnetic fluxes of emerging and existing magnetic poles. The overall magnetic configuration would be complex and intense flares would originate in this scenario.

configuration, where opposite magnetic fluxes are close to each other. Shearing motions and magnetic flux cancellation along the PIL store the magnetic free energy by forming sheared and twisted magnetic structure (van Ballegoijen & Martens 1989). Though the length of sgPILs does not quantify the shearing motion and magnetic flux cancellation, it indicates the possibility of these processes in an AR.

It is important to note that our selection of ARs was based on the contrast cases of FI and sunspot sizes. Maybe due to selected ARs, the correlation between total magnetic flux and FI was very small. Nevertheless, we believe that the present study was very clear to differentiate the evolution of SAARs and LAARs. We summarize our major findings in the following list:

1. SAARs have complex magnetic configuration than LAARs. SAARs have opposite magnetic fluxes in close proximities of each other, generally in the middle of the

ARs, giving a complex magnetic configuration and long PILs to ARs. On the other hand, opposite magnetic fluxes are well separated from each other in LAARs, like in a simple bipole with β -configuration.

2. Magnetic flux emergences do not necessarily lead to the formation of a complex magnetic configuration. New magnetic flux emergence was observed in both SAARs and LAARs. The interaction between opposite magnetic fluxes of non-conjugate pairs (existing and emerging) created the complex magnetic configuration in SAARs. In LAARs interaction between like magnetic fluxes of non-conjugate pair keep the overall magnetic configuration simple.
3. The separation of conjugate pair sets up a long-term shearing motion and flux cancellation along the PIL between non-conjugate pairs. Our study found that many of the intense flares from SAARs are located around the PIL. This suggests that multiple intense flares were caused by the consistent shearing motion and flux cancellation.
4. The present study found a weaker correlation (< 0.5) between flare productivity (FI) and total flux content, net flux, current density, and current helicity. The correlation between flare productivity and total flux content was the weakest (0.16).
5. Our study found a stronger correlation (> 0.5) between flare productivity (FI) and degree of current neutralization, length of sgPIL, and R-value. The correlation between flare productivity and sgPIL/ R-value was the strongest (0.8).

Chapter 4: What Causes Homologous Eruptions?

Solar eruptions, manifested as flares and Coronal mass ejections (CMEs), are the most spectacular phenomena happening in the solar corona. Besides being magnificent, these are the main sources of the disturbances in the interplanetary space and the space weather effects near the Earth. Flares and CMEs (often occur together) are probably the manifestation of a single energy release process, during which a tremendous amount of stored magnetic energy is released from the solar atmosphere (see, Forbes 2000; Zhang et al. 2001). The CSHKP model (initially developed by Carmichael 1964; Sturrock 1966; Hirayama 1974; Kopp & Pneuman 1976) describes the solar eruption as the eruption of magnetic flux rope (MFR) through magnetic reconnection (e.g., Forbes 2000). An MFR is a highly sheared and twisted magnetic field structure. In stable condition, MFR is kept in equilibrium by the overlying magnetic field lines. Due to some instability or loss of equilibrium, the MFR starts to rise and it could result in three scenarios:

1. **Failed eruption:** In this scenario, MFR rises up as it is erupting and then stops at a certain maximum height (Song et al. 2014). It could stop due to many reasons e.g., strong overlying magnetic field pressure (Sun et al. 2015), an asymmetric overlying coronal field distribution (Liu et al. 2009), or not having sufficient energy for a successful eruption (Shen et al. 2011).
2. **Partial eruption:** As the name suggests, in this scenario only part of MFR erupts from the Sun. MFR can be split into two parts by (a) reconnection within the MFR (Gibson & Fan 2006), or (b) the partial emergence and reconnection with the coronal dipole field (Leake et al. 2014). Non-erupting filaments or immediate reformation of long-lived X-ray sigmoids after the eruption is considered as a signature of partial eruption (Tang 1986; Gilbert et al. 2000; Gibson et al. 2002).

3. Full eruption: In this scenario, MFR fully escapes from the Sun.

In the last case, an AR (or solar region where eruption happened) returns to a potential magnetic configuration of minimum energy. However, in the first two scenarios AR could be still in non-potential magnetic configuration with some stored free magnetic energy. There are not many studies comparing the pre and post eruption evolution in such cases.

A typical solar eruption has three phases: (i) the precursor phase (PP), (ii) the impulsive phase (IP), and (iii) the gradual phase (GP; see Zhou et al. 2016 for a discussion). The PP is important for understanding the initiation of solar eruptions and validating different models of them (Gopalswamy et al. 2006). In the past, different observational signatures have been identified in the PP for certain individual events, such as: soft X-ray (SXR) emission (Fárník et al. 1996; Fárník & Savy 1998), hard X-ray bursts (Harra et al. 2001), UV/EUV brightenings (e.g., Joshi et al. 2011; Awasthi et al. 2014), type II radio bursts (e.g., Klassen et al. 2003; Liu et al. 2007), prominence oscillation (Chen et al. 2008), and MFR oscillation (Zhou et al. 2016). However, due to weak or entirely absent observational activities during the PP, its current understanding is very poor compared to the IP and GP (Hudson 2011).

Though rare, multiple eruptions could originate from the same local region of an AR consecutively (e.g., Gopalswamy et al. 2004). Successive eruptions from the same region, with homologous flares, similar dimming in extreme ultraviolet (EUV) imaging, and similar coronagraphic morphology are known as homologous eruptions (Zhang & Wang 2002). Multiple eruptions are possible only if certain physical processes continuously store magnetic energy in the region or when the stored energy is not released in a single eruption (Gopalswamy et al. 2005). Therefore, their study is important to understand the mechanisms of long-term magnetic energy build-up in the corona.

In the past, homologous eruptions have been studied either during the magnetic flux emergence phase and were considered due to flux emergence (e.g., Nitta & Hudson 2001; Chatterjee & Fan 2013) or flux decaying phase and were considered due to shearing motion

and magnetic flux cancellation (e.g., Li et al. 2010; Vemareddy 2017a). The persistent photospheric horizontal motion of the magnetic structure along the PIL was also considered to produce homologous eruptions (e.g., Romano et al. 2015; Romano et al. 2018). Observations of initiation of solar eruptions are very rare, therefore our understanding of the triggering mechanism of solar eruptions is not matured. Homologous eruptions can be triggered by similar mechanisms, such as moving magnetic features (Zhang & Wang 2002), coronal null point magnetic configuration (e.g., DeVore & Antiochos 2008) and shearing motion and magnetic reconnection (e.g., Vemareddy 2017a). Therefore, their study is also important to understand the triggering mechanism of solar eruptions.

Here, we analyze three homologous eruptions, viz., SOL2012-03-07T01:05, SOL2012-03-09T03:22, and SOL2012-03-10T16:50. These eruptions originated from the same location in the complex AR 11429, but at different magnetic flux evolutionary phases. An MFR of similar morphology was formed, along the same PIL, before each of the three eruptions. Magnetic flux cancellation led by the shearing and converging motion and new connectivity in the corona were responsible for its formation. A confined flare was observed during the precursor-phase (PP) of each eruption, which helped in the eruption by weakening the constraint of overlying magnetic fields. The chapter is structured as follows. Successive eruptions are described in Section 4.1. The evolution of the AR before each eruption, pre-eruptive coronal magnetic structures, and initiation of eruptions are described in Section 4.2.1. Discussion and conclusions of the study are presented in Section 4.3.

4.1 Observations of Homologous Eruptions

The NOAA AR 11429 was initially emerged on the backside and appeared on the eastern limb of the Sun on March 4, 2012. During its front disk transition, the AR acquired very complex magnetic-configuration ($\beta/\gamma/\delta$), with many small magnetic polarities (see Elmhamdi et al. 2014 for more details about the evolution of magnetic configuration). However, as discussed in Chintzoglou et al. 2015 and Dhakal et al. 2018, it could be divided

into two relatively simpler sub-regions namely: northeast (NE) and southwest (SW) sub-regions, more discussed in the section 4.2.1. Also, it had an anti-hale magnetic configuration i.e., the leading magnetic polarity (positive) was opposite of the normal hemispheric trend (negative). Both δ and anti-hale magnetic configuration are identifiable with severe flaring activity (e.g., Zirin 1970; Tanaka 1991; Sammis et al. 2000). Indeed, it was super flare and CME productive. Moreover, four of the eruptions from the AR were associated with sustained gamma-ray emission (SGRE; Gopalswamy et al. 2019). Most of the flares were observed before the AR crossed the central meridian on March 9. By the end of March 9, it had produced 3 X-class, 11 M-class, and 30 C-class flares. Afterward, there were only 2 M-class flares and 7 C-class flares. The events under study occurred in the SW sub-region in the interval of ~ 4 days. These homologous eruptions are summarized in Table 4.1.

Table 4.1: Three homologous solar eruptions from AR 11429.

^aInitiation time of the solar eruption

^bflare location

^cpeak time of GOES X-ray flux

^dfirst LASCO C2 appearance

^elinear speed of CME in LASCO C2, obtained from https://cdaw.gsfc.nasa.gov/CME_list/UNIVERSAL/2012_03/univ2012_03.html

Three Homologous Solar Eruptions from AR 11429					
Events	Initiation Time ^a	Location ^b	Flare (Peak Time) ^c	C2 Appearance ^d	Speed (km s ⁻¹) ^e
CME1	2012/03/07 01:05	N15 E26	X1.3 (01:14)	01:30 UT	1825
CME2	2012/03/09 03:22	N15 W03	M6.3 (03:53)	04:26 UT	950
CME3	2012/03/10 16:50	N17 W24	M8.4 (17:44)	18:00 UT	1296

The first solar eruption occurred on 2012 March 7 at $\sim 01:05$ UT when the AR was in the north-east quadrant of the solar disk. On March 7, within one hour, there were two solar eruptions viz., SOL2012-03-07T00:02 (shown in red dotted line in Figure 4.1(a)) and SOL2012-03-07T01:05 (shown in black line in Figure 4.1(a)) from the NE and SW sub-regions respectively (see Chintzoglou et al. 2015). Here, we study the eruption from

the SW sub-region. It was associated with X1.3 class flare and its location was \sim N15E26. Associated flare ribbons were concentrated mainly on the positive and negative fluxes of the SW sub-region (see Figure 4.1(d) for observed flare ribbon in AIA 1600 Å) and were observed to move away on either side of the PIL during the MFR eruption. The position and separation of the flare ribbons indicated that the MFR erupted from the SW-PIL. The eruption led to the coronal mass depletion in the region and observed as coronal dimming in different AIA passbands (e.g. Tian et al. 2012; see Figure 4.1(g) for observed dimming in AIA 193 Å). Later it was observed as halo CME, moving with 1825 km/s (CDAW CME catalog), in *LASCO* white light observation at 01:30 UT. The morphology of the CME at a single time snapshot is not clear due to contamination from the earlier CME. However, its morphology was clear in *STEREO-A* FOV as eastward-moving CME and in *STEREO-B* FOV as westward-moving CME (see upper panels of the Figure 4.2).

The second solar eruption started on 2012 March 9, at \sim 03:22 UT when the AR was located around the central meridian of the solar disk. It was associated with an M6.3 class flare (see Figure 4.1(b)) at \sim N15W03. The flare ribbons, similar to the ribbons of the previous eruption, evolved and concentrated on the opposite magnetic flux in the SW sub-region (see Figure 4.1(e)). This again indicated that the MFR had erupted from the SW-PIL. A dimming similar to the previous eruption was observed in EUV observation (see Figure 4.1(h)) and eventually observed as halo CME in *LASCO* C2 at 04:26 UT. In the *LASCO* FOV CME moved with a linear velocity of 950 km/s. *STEREO-A* data was not available during that period, but like the earlier eruption it appeared as westward-moving CME in *STEREO-B* FOV (see middle panels of the Figure 4.2).

The third solar eruption started on 2012 March 10, at \sim 16:50 UT when the AR was at the north-west quadrant. It was associated with an M8.4 class flare (see Figure 4.1(c)) at \sim N17W24. The evolution and separation of flare ribbons were similar to the previous two eruptions and they were primarily concentrated on the opposite magnetic flux of the SW sub-region (see Figure 4.1(f)). Therefore, the third MFR also erupted from the SW-PIL. Observed EUV dimming was also similar to the previous two eruptions (see Figure 4.1(i)).

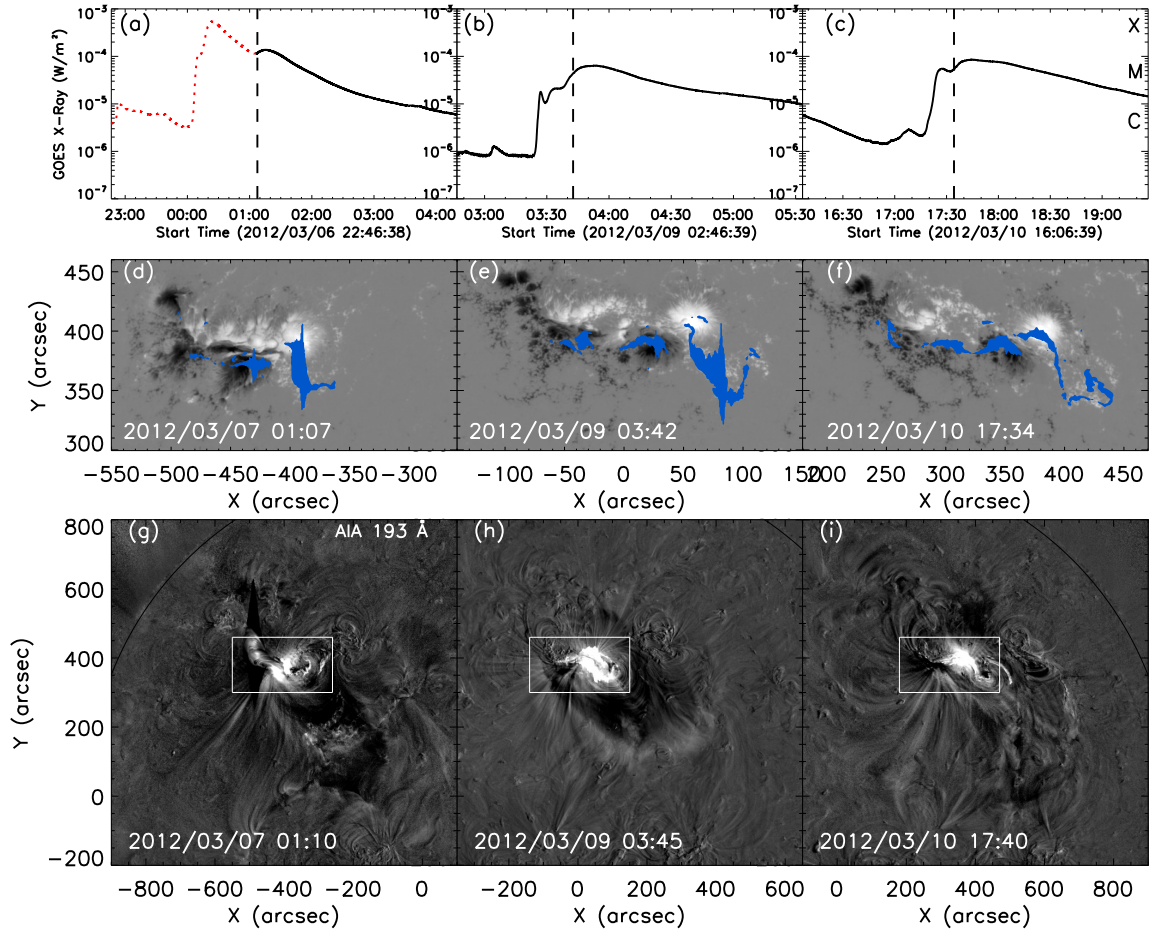


Figure 4.1: Three homologous eruptions from NOAA AR 11429. (a-c) time profiles of GOES soft X-ray intensity flux during the three eruptions. The maximum flux in these profiles corresponds to X1.3, M6.3, M8.4 flares, respectively. The red dotted line in (a) shows the contamination in the X-ray profile due to an earlier eruption. (d-f) Overlay of the flare ribbons (in blue) observed in AIA 1600 Å on HMI LOS-magnetogram. (g-i) Difference images of AIA 193 Å showing the EUV dimming associated with each eruption. The white box represents the FOV of the magnetograms shown in (d-f).

It appeared as halo CME in *LASCO* C2 at 18:00 UT, moving with a linear velocity of 1296 km/s. Like earlier eruptions, it was observed as eastward-moving CME in *STEREO-A*, and westward-moving CME in *STEREO-B* (see the lower panels of Figure 4.2) with a similar CME morphology.

All three solar eruptions were originated from the SW-PIL of the AR 11429. The

direction of successive CMEs seemed to move towards north-side in *STEREO* FOV and this could be due to the change in magnetic flux distribution with evolution. Nevertheless, the overall morphology of the CMEs appeared similar in each recurring eruptions. Also, the X-ray profile, evolution of flare ribbons, and EUV dimming associated with these eruptions were nearly identical to be homologous eruptions. The time difference between the first and the second eruption was ~ 50 hours, and the time difference between the second and the third eruption was ~ 37 hours. The next section discusses the evolution of the AR that led to identical solar eruptions.

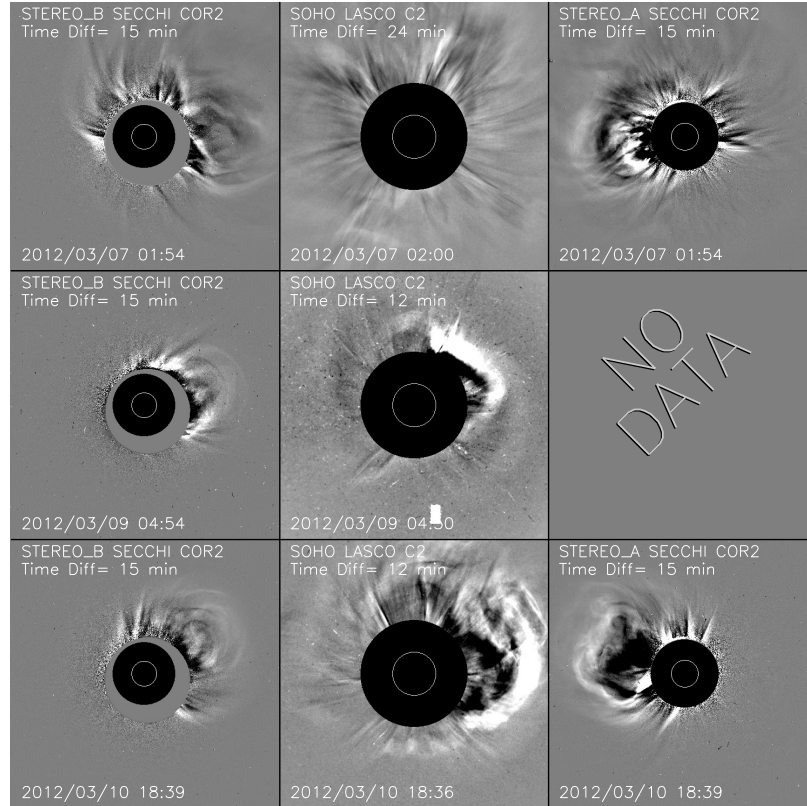


Figure 4.2: Homologous CMEs seen from three different view points. Left panels: the COR2 images from SECCHI/STEREO-B. Middle panels: the C2 images from LASCO/SOHO. Right panels: the COR2 images from SECCHI/STEREO-A.

4.2 Evolution of AR 11429 Leading to Homologous Eruptions

We used the preprocessed cutouts of SHARP data products (`hmi.sharp_cea_720s`) to study the photospheric evolution of the magnetic flux distribution in the AR. Preprocessing resolves the 180° azimuthal uncertainty and remaps helioprojective images into a cylindrical equal-area (CEA) projection, where each pixel has the same surface area (Hoeksema et al. 2014). Although there were several episodes of new magnetic flux emergence in the early evolutionary period, no major emergence was observed after March 8, as is evident from the time-profile of magnetic flux of the AR shown in the Figure 4.3 (also, see the movie accompanying Figure 4.4). Here, we used the CEA maps of HMI LOS-magnetogram to analyze the magnetic flux. The apparent 12-hour periodicity in the plots of magnetic flux (in Figure 4.3) is due to instrumental effect and related to spacecraft orbital velocity, also there is a variation of the number of pixels contributing to the low-to-moderate magnetic field values as AR moves from central meridian to the limb (see, Hoeksema et al. 2014). Solar eruptions under consideration had occurred at the different evolutionary phases of the AR (eruptions are shown by dashed-vertical lines in Figure 4.3). The first eruption had occurred when the total magnetic flux was increasing i.e. during the magnetic flux emergence phase. The second eruption happened at the end of the flux emergence phase, and the third eruption happened during the flux decay phase of the AR. In the following, we describe the evolution of the AR, focusing on SW sub-region, in the period of 2012 March 6 to March 11.

4.2.1 Evolution of the Photospheric Magnetic Field

Initial compactness and complexity of the magnetic flux distribution of the AR decreased with its evolution. It was divided into two simpler sub-regions: NE and SW based on the presence of two erupting MFRs on 2012 March 7 (Chintzoglou et al. 2015) and are shown

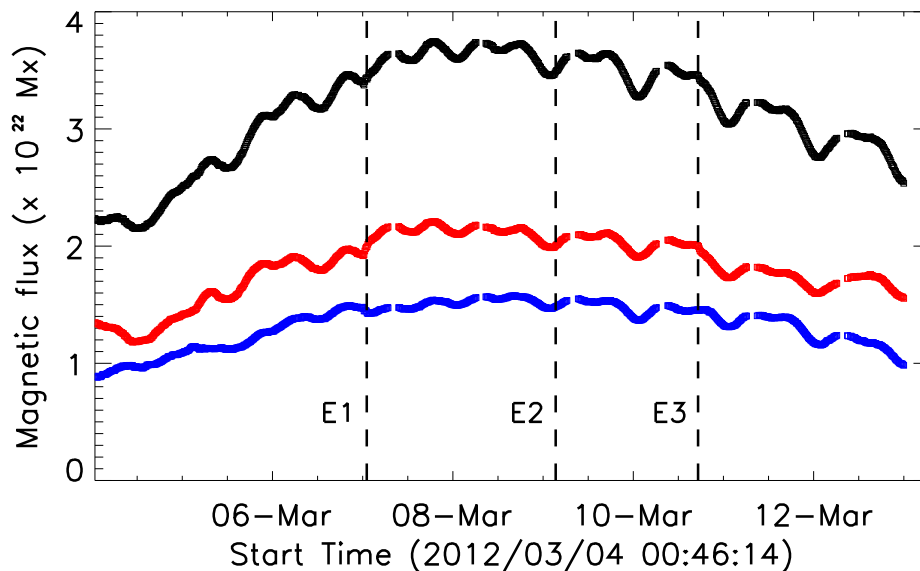


Figure 4.3: Time evolution of the magnetic-flux in the AR 11429 during March 4-13. The total unsigned magnetic flux is plotted in black, the total negative magnetic flux is plotted in red and the total positive flux is plotted in blue. Dashed vertical lines marks the time of three homologous solar eruptions.

in red and cyan box respectively in Figure 4.4(a). The distinction between the two sub-regions become more clear in the later evolutionary period. Long and sharp strong-gradient PILs, shown in green asterisks in the left panels of Figure 4.4 (obtained from an image gradient operation as discussed in Zhang et al. 2010), were present throughout the observational period. The plasma velocity maps show the persistent shearing motion between opposite magnetic fluxes along the SW-PILs (see the middle panels of Figure 4.4; also see the movie accompanying Figure 4.4 for the plasma velocity). These maps were derived using DAVE4VM method with an apodization window of 19 pixels (Schuck 2008). Shearing motions along the PILs are well known to convert potential field to sheared field arcade (e.g., van Ballegoijen & Martens 1989). The direction of horizontal magnetic fields, which were aligned along the length of PILs (see the right panels of Figure 4.4), indicated that there was indeed strong non-potential shear along the PILs. The SW-PIL was lying between two large areas of opposite magnetic polarity i.e., P-SW and N-SW (see Figure 4.4(d)). The

distance between the centroid of opposite magnetic poles was decreasing with time (see the plot in black-asterisks in Figure 4.5). This showed that the opposite magnetic poles were continuously converging towards each other. The centroid-distance was decreased by ~ 1 Mm between first and second solar eruptions (from March 7 to March 9) and by ~ 2 Mm between second and third eruptions (from March 9 to March 10). Though the convergence was observed in both flux emerging and decaying phase, the rate of convergence was increased after the flux emergence had been stopped. Flux cancellation was not obvious from the plot of the magnetic flux of the entire AR and it was hard to isolate the SW sub-region completely. However, after March 6 it was possible to isolate the negative polarity of the SW sub-region. Therefore we encompassed the negative polarity with an ellipse and ellipse was varying with time to make sure that it fully encompassed the negative polarity all the time, and analyzed it. The plot in red asterisks in Figure 4.5 shows the time-profile of negative flux in the SW sub-region. The negative flux was decreasing gradually, indicating a continuous flux cancellation in the SW sub-region. Though the rate of convergence was increased after the second eruption on March 9, there was no significant change in the slope of the negative magnetic flux, which indicates that the flux cancellation rate was almost the same during and after the flux emergence phase.

To understand the high eruptivity of the AR 11429, we analyzed certain non-potential parameters: viz, non-neutralized current, length of sheared PIL, helicity injection rate (dH/dt), and energy injection (dE/dt) rate (for computational details of these parameters see, Vemareddy 2015; Vasantharaju et al. 2018b; Vemareddy 2019b). The upper panel of Figure 4.6 shows the non-neutralized currents in positive (negative) polarity in blue (red). A strong non-neutralized current was observed in the AR 11429 throughout the observational period. Also, long sheared PILs were observed throughout the evolution of the AR (shown in grey in the upper panel of Figure 4.6). The stress in the field lines due to plasma flows generates non-neutralized current in an AR (e.g., Török et al. 2014; Vemareddy et al. 2015; Vemareddy 2017b). A higher level of deviation (> 1.5) from the current neutrality condition and long sheared PILs suggests that the AR was very CME

productive (e.g., Liu et al. 2017; Vemareddy 2019a). There was a significant decrease in the length of sheared PIL after March 9, and maybe that was the reason for the decrease in the flare activity after it. Further, continuous shearing and converging motions of opposite magnetic fluxes were injecting and storing magnetic helicity and magnetic energy in the solar corona (see the middle and lower panels of Figure 4.6). The rate of helicity and energy injection was almost constant after March 7. The initial high helicity and energy rates were due to major magnetic flux emergence during the early evolutionary phase of the AR. Continuous shearing and converging motion of the opposite magnetic fluxes were continuously injecting magnetic helicity and energy in the AR 11429 and were responsible for recurrent solar eruptions. The homologous eruptions can be understood as a cycle of storage and release of magnetic helicity and energy from the AR (Vemareddy, 2017a).

4.2.2 Pre-eruptive Structures in the Corona

While strongly influenced by magnetic evolution in the photosphere, solar eruptions occur in the corona. Therefore, coronal magnetic structures and their evolution are one of the most important aspects of solar eruptions. One way to analyze them is through the observation of plasma-emission at different electromagnetic wavelengths. Another way to know about the coronal magnetic field is through the extrapolation of photospheric magnetic field data. However it is not possible to get the exact 3D magnetic field in the corona through 2D magnetic flux observations. Therefore observational validation is necessary for the analysis of such results. Here, we used both techniques to complement each other and to have a proper understanding of pre-eruptive coronal structures and environment. To reconstruct the coronal magnetic structure, we carried out NLFFF extrapolation (Wiegelmann & Inhester 2010) at every hour from 2012 March 6, 00:10 UT to 2012 March 10, 19:34 UT. Cutouts of HMI vector magnetograms were taken as the bottom boundary of the computational domain. These were inserted in an extended field of view to weaken the effects of lateral boundaries and were pre-processed to make them suitable for the force-free conditions (Wiegelmann et al. 2006). Computations were performed on a uniformly spaced

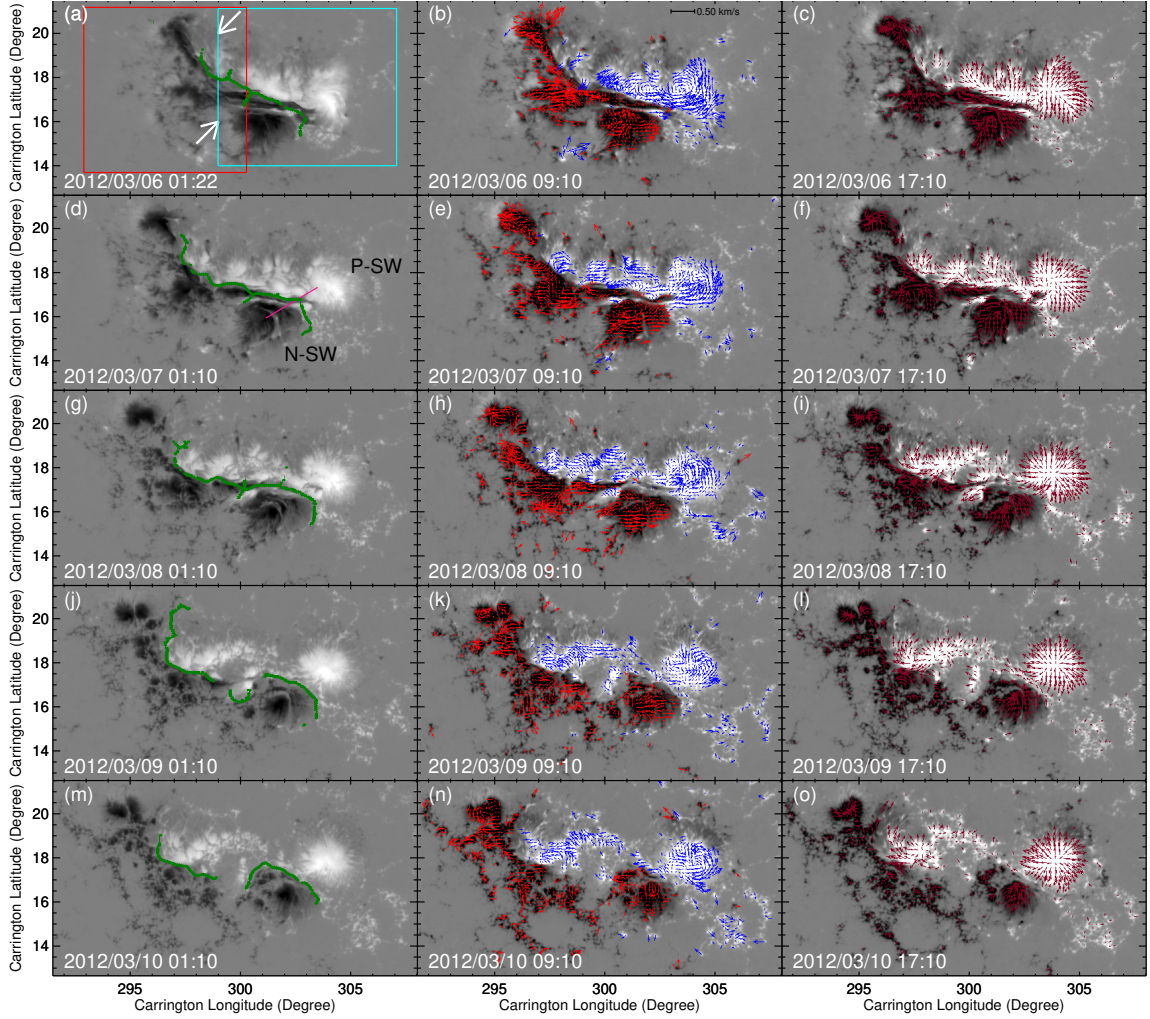


Figure 4.4: Evolution of the photospheric magnetic field in NOAA AR 11429. Images are taken from the line-of-sight magnetograms of SDO/HMI and shown in a cylindrical equal-area heliographic projection. Left panels: the strong-gradient polarity inversion lines in green asterisks are overplotted on the HMI LOS-magnetogram. The red and cyan boxes, in (a), represent the northeast (NE) and southwest (SW) sub-regions respectively, and white arrows show the location of new flux emergence. The pink line in (d) shows the distance between the centroid of positive (P-SW) and negative (N-SW) polarity in the SW sub-region. Middle panels: the direction of motion of positive (negative) flux are overplotted on the HMI LOS-magnetogram in blue (red) arrows. Right panels: the direction of the horizontal component of magnetic fields are overplotted on the HMI LOS-magnetogram in brown arrows.

grid of $276 \times 148 \times 196$ pixels corresponding to a physical volume of $199 \times 106 \times 141 \text{ Mm}^3$ (more details in Dhakal et al. 2018).

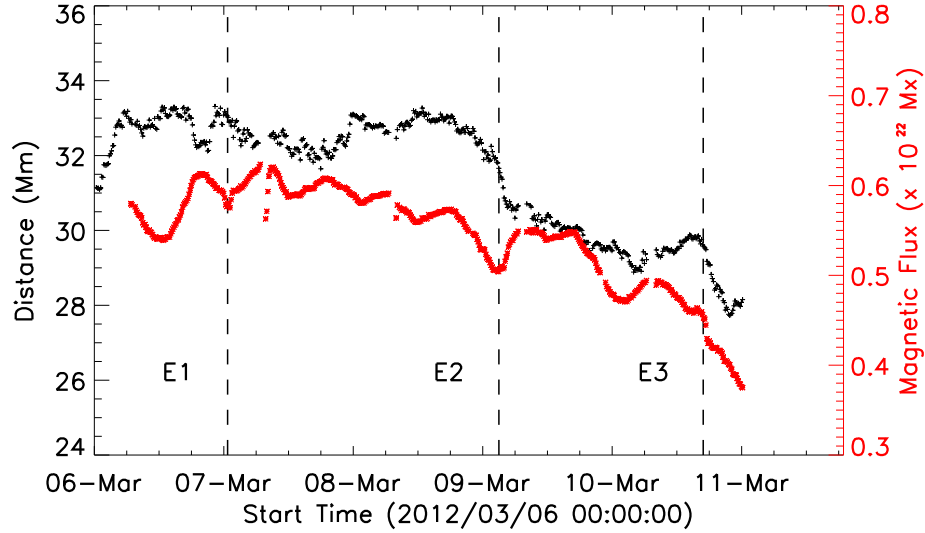


Figure 4.5: Convergence of opposite magnetic polarity and magnetic flux cancellation in the southwest sub-region of the AR 11429. Convergence rate is examined by monitoring the distance between the centroid of positive and negative magnetic polarity and is shown in black asterisks. The time profile of negative flux in the SW sub-region is in red. The vertical dashed lines refer to the time of three solar eruptions from the AR.

A filament was observed to lie along the SW-PIL (see Figure 4.8), indicating sheared and/or twisted field lines (e.g., Priest et al. 1989). Following the eruptions on March 7 and 9, the filament was observed to still exist along the SW-PIL under the fading post-flare arcade in AIA cool passbands (see Figure 4.7). The appearance of the filament, immediately after the eruption, suggests that either only part of it erupted or it did not erupt at all, thus indicating the partial eruption of the magnetic structure (e.g., Tang 1986; Gilbert et al. 2000; Gibson et al. 2002).

On March 6 at 23:35 UT, \sim one hour prior to the first solar eruption, we observed a coherent hot-channel structure (HCS) to lie along the SW-PIL (see Figure 4.9(a)). Hot channels are so named as they are observed in hot passbands of the AIA i.e., 94 \AA (6 MK) and 131 \AA (10 MK) (e.g., Zhang et al. 2012). The temperature map, obtained through differential emission measure (DEM) method (e.g., Cheng et al. 2012), indicated that it was hotter than 7 MK. It was also observed as sigmoid in X-ray images (see Figure 4.9(c)).

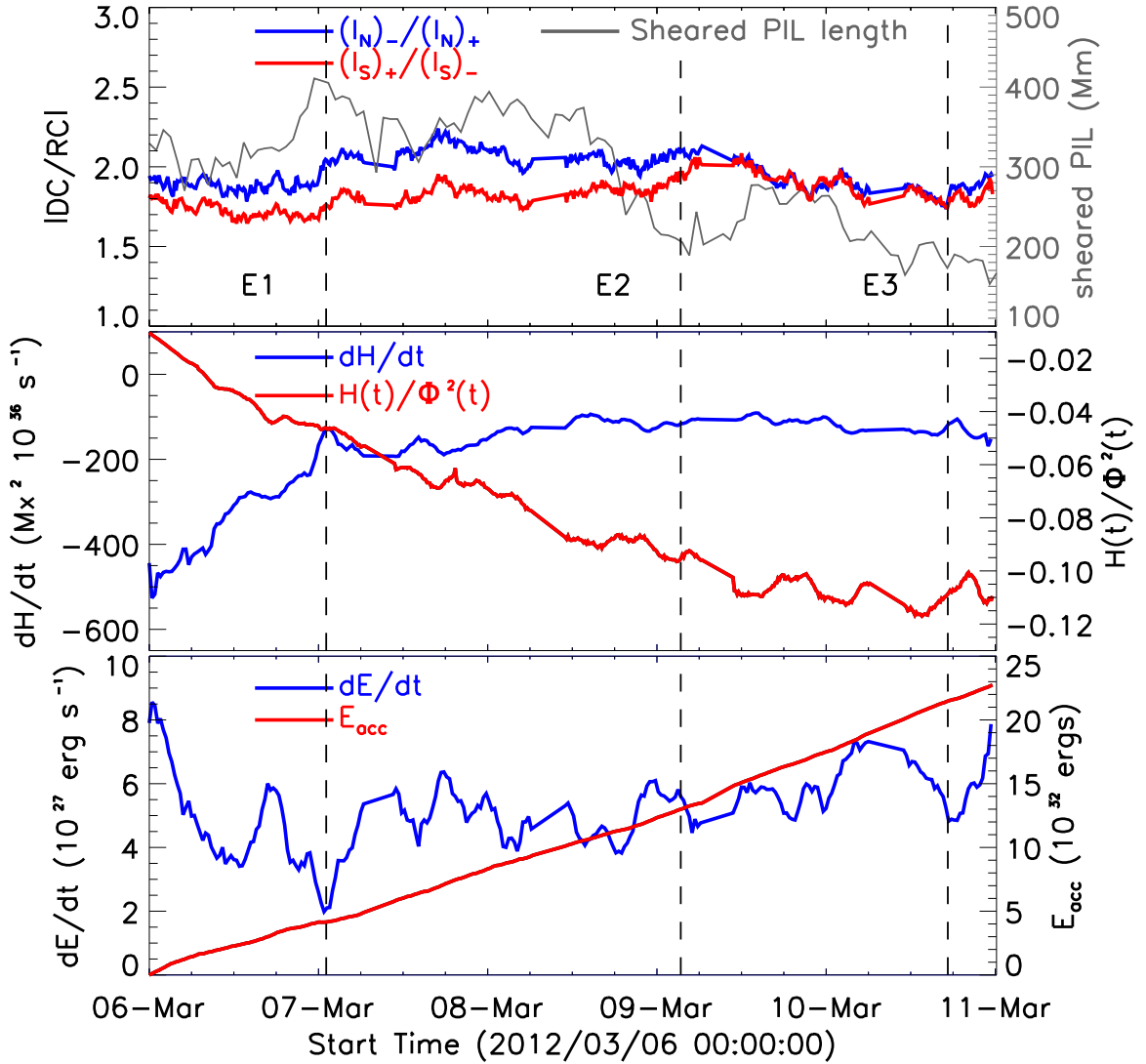


Figure 4.6: Evolution of non-potential parameters in AR 11429. Top panel: Degree of net current neutralization in positive (negative) polarity in blue (red). A higher value of around 1.8 suggest non-neutralized currents in the AR flux system and instability. The length of sheared PILs is also plotted in grey. Middle panel: the time rate of helicity flux is plotted in blue. Normalized accumulated helicity (time-integrated helicity flux normalized with square of the flux) is plotted in red. Bottom panel: energy flux injection (pynting flux) and its accumulated quantity in blue and red respectively.

These are called sigmoid because of their forward-S or reverse-S shape (e.g., Rust & Kumar 1996). Both the HCS and X-ray sigmoids are considered as the observational proxy of MFR (e.g., Green et al. 2007; Zhang et al. 2012). NLFFF extrapolation results showed that

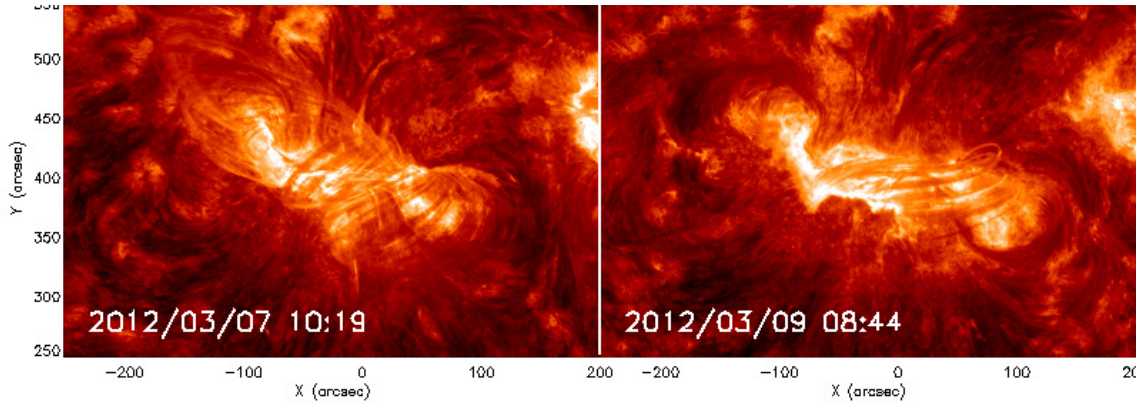


Figure 4.7: Filament observed in the AIA 304 Å. The left panel shows the survived filament under the post-flare arcade of the eruption on 2012 March 7. The right panel shows the survived filament under the post-flare arcade of the eruption on 2012 March 9.

long, sheared and twisted magnetic field lines were lying along the SW-PIL (see the top panels of Figure 4.10). Both observational and extrapolation results suggest the existence of an MFR in the SW sub-region of the AR. As discussed in section 4.1, the HCS was observed to erupt on March 7 around 01:05 UT. A coronal structure was seen to reform by March 9 01:30 UT, in the SW sub-region over the period of two days. Its morphology in EUV and X-ray images was similar to the coronal structure observed on March 6 (see the middle panels of Figure 4.9). Ensuing the eruption on March 9 at 03:00 UT, another coronal structure of identical morphology (see the lower panels of Figure 4.9) was observed to reform in the period of one and half days. The extrapolation results showed that the coronal structure (on both days) was sheared and twisted like the observed structure on March 6 (see Figure 4.10). This suggests that MFR of identical shape was reformed before each homologous eruption. A persistent convergence and flux cancellation were observed in the SW sub-region. Also, there was a continuous shearing motion between the opposite magnetic fluxes. Shearing motion and flux cancellation are well known to generate long and twisted field lines along the PILs (e.g., van Ballegoijen & Martens 1989). This suggests that the shearing motion and flux cancellation were responsible for the recurrent formation of MFR along the SW-PIL.

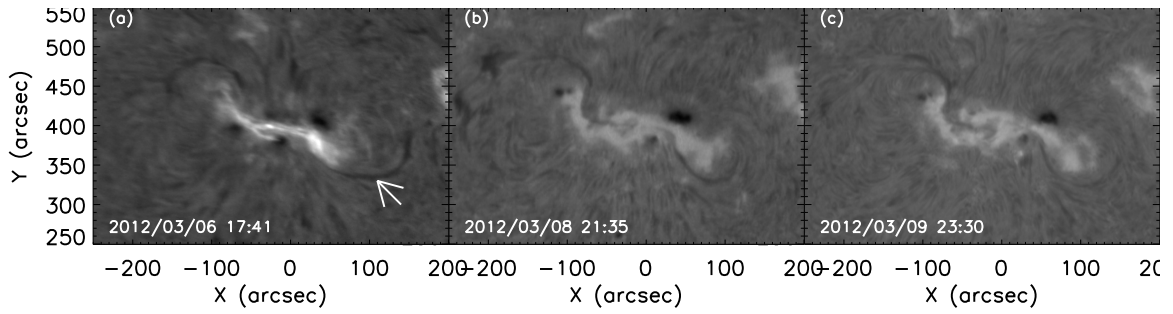


Figure 4.8: Filament of identical shape, in $H\alpha$ images from BBSO, were present persistently during the evolution of the AR 11429. White arrow in (a) points to the filament in southwest sub-region of the AR.

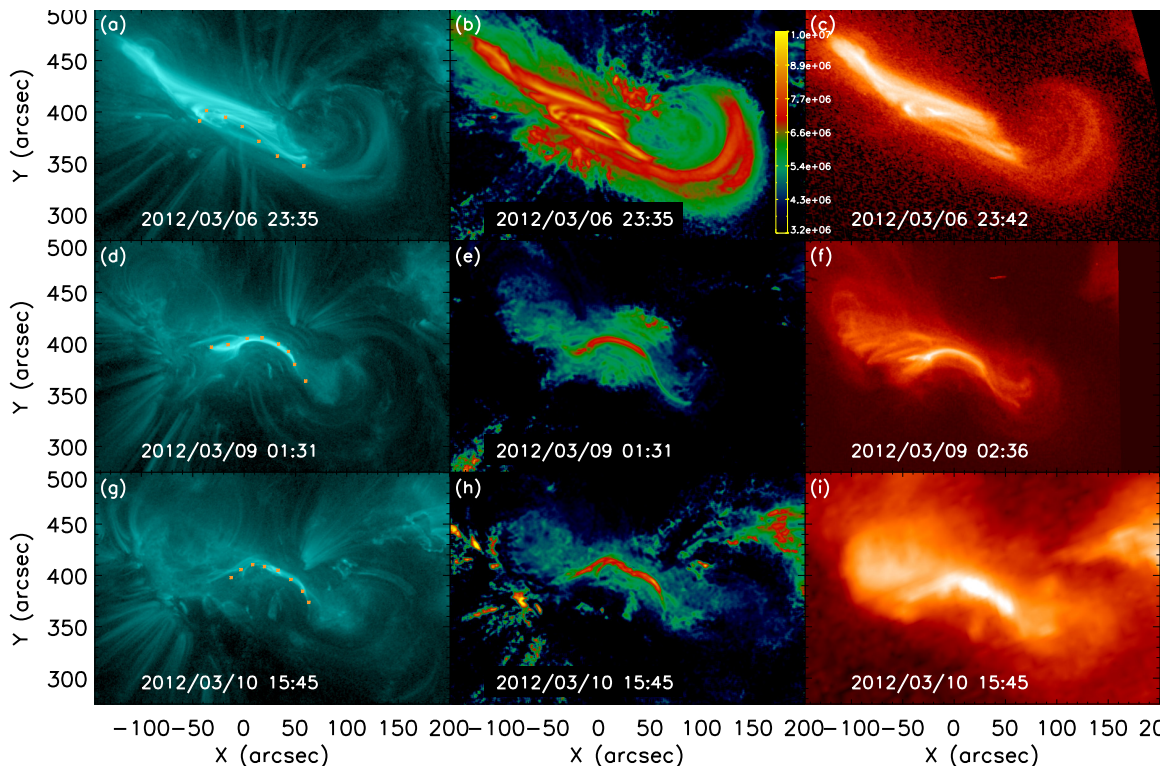


Figure 4.9: Observation of pre-eruptive coronal structure. Left panels: the hot-channel structures (HCS) before each eruptions in AIA 131 \AA . The brighter part of the HCS is outlined by orange asterisk. Middle panels: the temperature map obtained using the DEM method. Right panels: the sigmoidal hot coronal structures in X-ray images. (c) and (f) images are from *Hinode*/XRT, and (i) is from *GOES*/SXI.

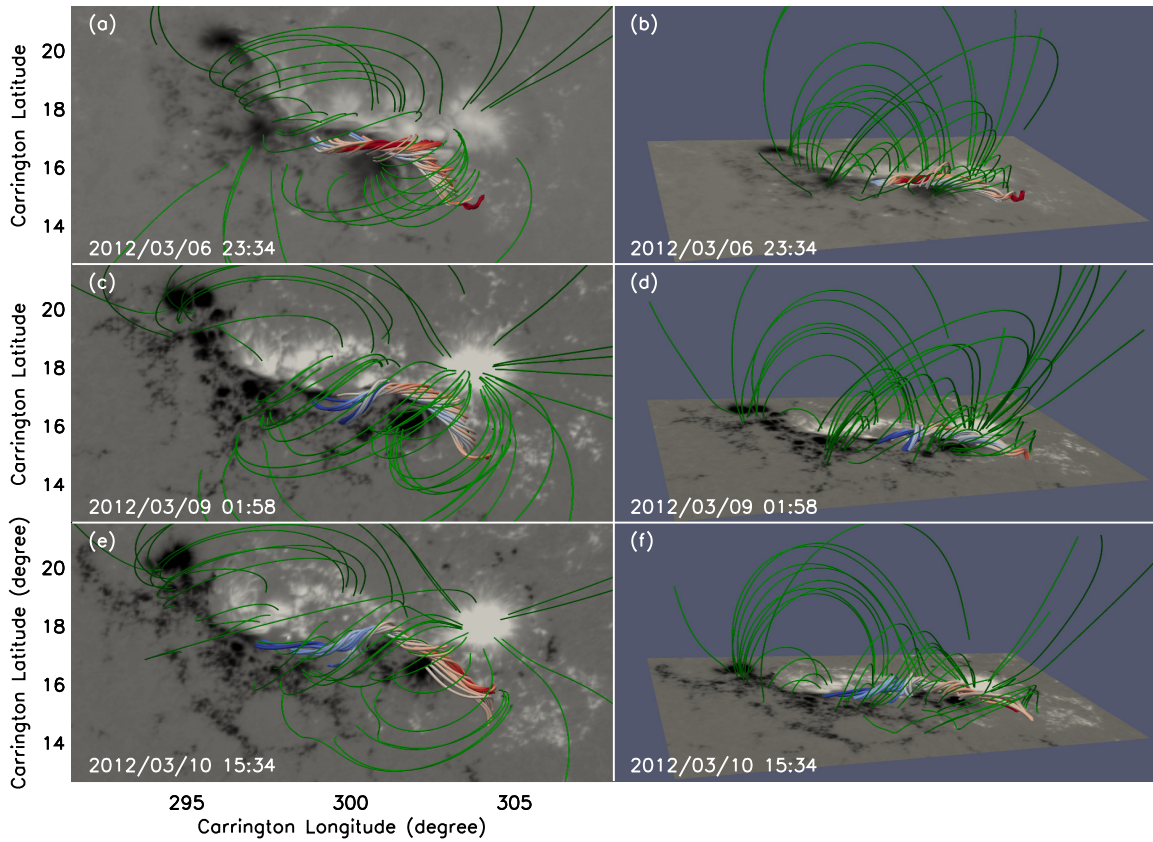


Figure 4.10: Magnetic structure modeled by NLFFF extrapolation. Left (right) panels show the top (side) view of magnetic field lines rendered on the HMI LOS-magnetograms before each eruption. The sheared and twisted field lines, along the southwest polarity inversion line (SW-PIL), are shown in blue-red lines. The green lines show the overlying magnetic field in the corona.

4.2.3 Initiation of the Eruption

A confined flare was observed on the left side of the SW sub-region during the PP of each eruption. It was observed as a small bump in the SXR intensity profile, a brightening of HCS, and the appearance of flare ribbons (see Figure 4.11 for the flare ribbons). The SXR peak of the PP for the first eruption was not observed due to the contamination from another nearby event (as discussed in 4.1; see Figure 4.1), nevertheless other signatures were observed. Identical PP could suggest that the triggering mechanisms were the same for the three solar eruptions (e.g., Vemareddy 2017a). The confined flare was observed near

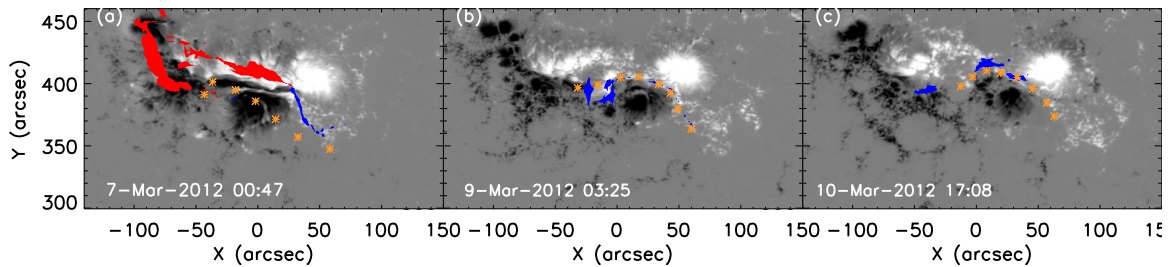


Figure 4.11: Confined flare during the precursor phase of each eruption. The contours of flare ribbons during the precursor phase activity, as observed in AIA 1600 Å, are overlotted on the HMI LOS-magnetogram in blue. The red contours in (a) show the flare ribbons from an earlier eruption. The orange asterisks indicate the outline of the hot-channel structure observed in AIA 131 Å.

the small chunk of positive magnetic flux (positive-chunk), which was almost surrounded by the negative magnetic flux (shown by a red arrow in Figure 4.12 (a)). Using NLFFF extrapolation results and codes developed by R. Liu and J. Chen (See Liu et al. 2016), we calculated the squashing factor Q in the AR 11429. The contours of high- Q are considered as the proxy of quasi-separatrix layers (QSLs; Titov et al. 2002). Flare ribbons appeared around the positive-chunk, therefore we analyzed the magnetic topology around it. The vertical-slice of Q -map in the middle of it revealed the presence of semicircular QSLs (see Figure 4.12), extending from one end to the other end of it. The previous study by Polito et al. (2017) of the AR 11429, on March 9, had found 3D dome-shaped QSLs surrounding the positive-chunk. Here, the vertical slice of dome-shaped QSLs is seen as semicircular QSLs. The semicircular shape of QSLs was maintained before each eruption, though its size changed over the period. QSLs are the probable sites of magnetic reconnection (Demoulin et al. 1996, 1997). The whole positive-chunk was very dynamic throughout the evolution of the AR. Also, new flux emergence was observed there before March 9. Therefore, the shearing motion or flux emergence could have triggered the magnetic reconnection there.

The MFR, along SW-PIL, was situated between two big magnetic poles and thus a strong overlying magnetic strapping force can be inferred above it. Strong overlying fields can inhibit successful eruption from ARs (e.g., Sun et al. 2015). The rate at which the

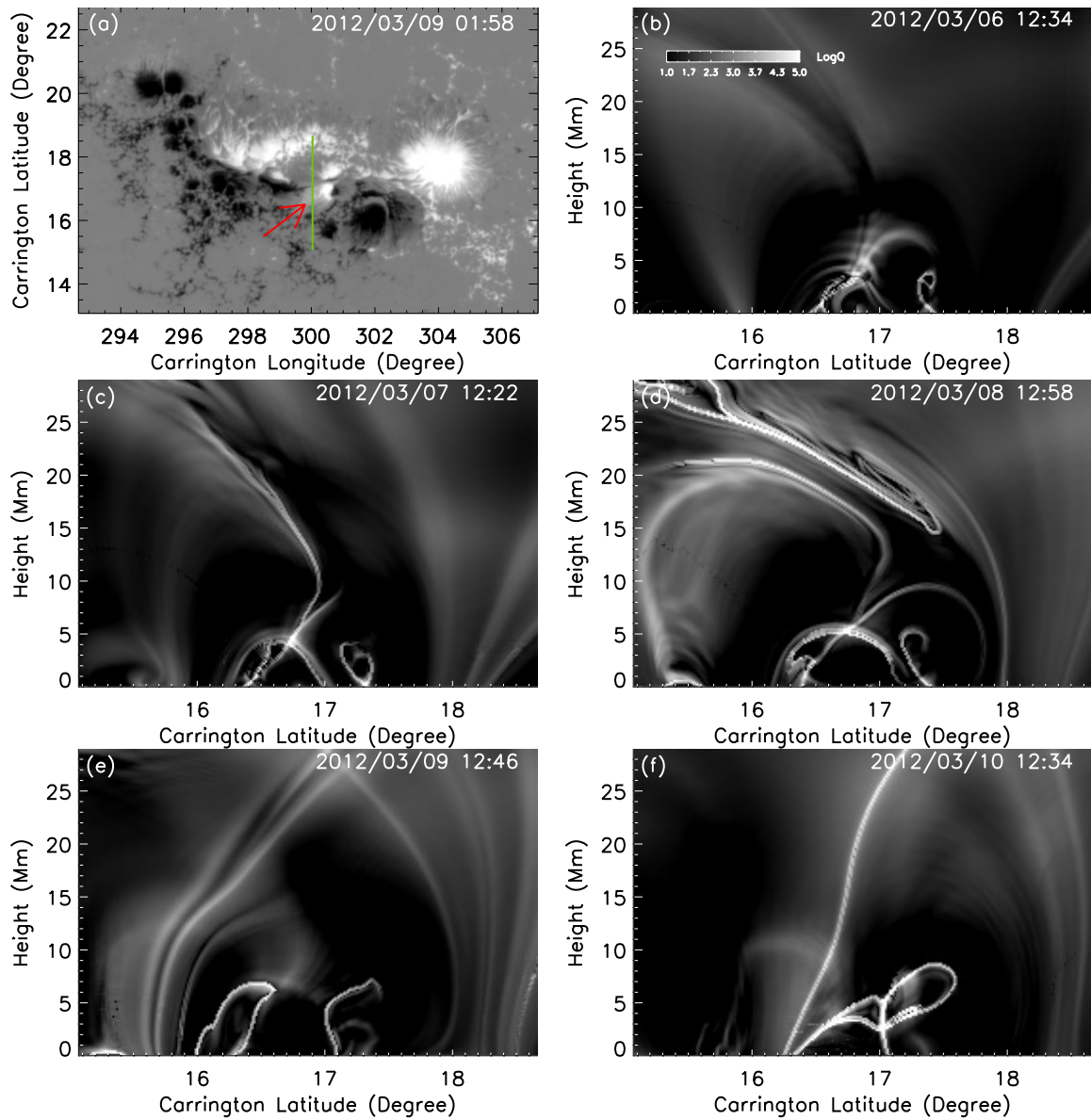


Figure 4.12: The magnetic topology at different evolutionary epochs of the AR 11429. (a) HMI LOS-magnetogram on March 9, red arrow shows the area where positive magnetic flux is almost surrounded by negative flux. (b-f) show the vertical slice of logarithm squashing factor Q ($\text{Log}(Q) > 5$) at the location of the green line in (a). Left panels show similar magnetic topology before each eruption.

strength of overlying magnetic fields decreases with height can be analyzed using the decay-index (n). An MFR becomes torus-unstable if n is greater or equal to the critical value ($n_{crit} = 1.5$; Bateman 1978; Kliem & Török 2006). Using NLFFF results we calculated the

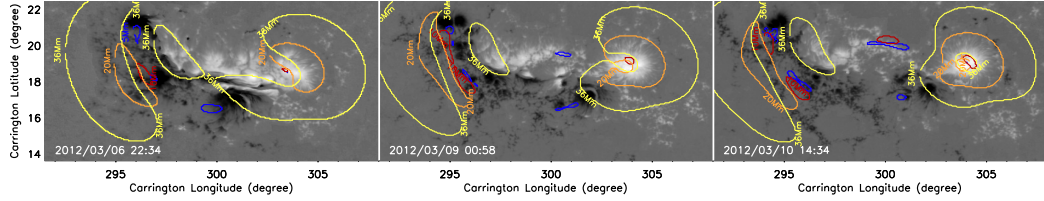


Figure 4.13: Contours of critical decay index ($n \geq 1.5$) for the AR 11429. The contours are overplotted on HMI LOS-magnetogram and different colors represent the heights at which decay index is calculated.

decay-index at different height as,

$$n = \frac{-d \log B_h}{d \log z} \quad (4.1)$$

Here, B_h is the horizontal component of the magnetic field, and z is the radial distance from the solar surface. Figure 4.13 shows the distribution of super-critical decay-index ($n \geq 1.5$) at different heights before each eruption. The closed contours represent the area where horizontal magnetic fields are very weak. An erupting MFR would preferably pass through such contours (e.g., Chintzoglou et al. 2015). In the SW sub-region, the contours changed and moved more toward the positive polarity with evolution. This could be the reason for the observed change in the direction of successive CMEs, as discussed in section 4.1. Also, it is clear from the decay-index maps that it would have been hard for low-lying MFR to become torus-unstable and erupt from the SW-PIL. Therefore, it is most probable that the PP flare facilitated the eruption of underlying MFR by weakening the constraint of overlying magnetic field.

4.3 Discussion and Conclusion

Our primary goal of the present study is to understand the recurrent homologous solar eruptions from the AR 11429. There were three homologous eruptions from the southwest (SW) sub-region within 87 hours. The first eruption was associated with X-class flare

and the other two eruptions were associated with M-class flares. Nevertheless, the shape of X-ray profiles of the three flares was very similar. The same photospheric location, similar evolution and location of flare ribbons, EUV dimmings, and identical coronagraphic morphology of the CME invoked them as homologous eruptions.

Our main result of the study is that the continuous flux cancellation due to shearing motions and the convergence of opposite magnetic bipoles along the PILs was the primary factor for the homologous solar eruptions. Flux emergence was observed only in the initial evolutionary period of the AR, flux cancellation was observed throughout the evolution that span all three events, including prior to the first event. While flux emergence was important and relevant in AR 11429, our study suggests that long-term flux cancellation and shearing motions were the most probable mechanisms that produced homologous eruptions. The photospheric motions of magnetic flux injected magnetic helicity and magnetic energy in the corona gradually. Stored helicity and energy released intermittently during solar eruptions. We believe that due to continuous shearing and converging motions of the magnetic flux, there was a cycle of storage and release of magnetic helicity and magnetic energy from the AR. In general, opposite magnetic poles of an emerging bipoles (conjugate pair) move away from each other, the separation distance depends on the flux content of the emerged bipoles (Wang & Sheeley 1989). In the present case, we did not observe the separation between opposite poles in SW sub-region, instead they were converging towards each other throughout the observational period. Therefore, we believe that these were non-conjugate pair. It was accompanied by the persistent shearing motion and magnetic flux cancellation. Chintzoglou et al. (2019) suggests that the convergence of opposite magnetic poles of non-conjugated pair leads to the magnetic flux cancellation and shearing motions, which could produce solar eruptions.

A filament was lying along the SW-PIL throughout the observational period and was observed soon after the eruptions. A filament survives and would be visible after a partial eruption. Partial eruption could happen either by the splitting of a single flux rope during the eruption(e.g., Gibson & Fan 2006; Zhang et al. 2015) or by the eruption of upper part

of double-decker system (e.g., Liu et al. 2012; Kliem et al. 2014). Though a double-decker system was observed along the SW-PIL before the eruption on March 10 (see Dhakal et al. 2018), it is hard to say whether a single flux rope split or a double-decker system was present before the eruption on March 7 and March 9. Nevertheless, we believe that there was a partial eruption of the magnetic system from the SW-PIL.

A magnetic structure was formed along the SW-PIL before each eruption. It was observed as a coherent hot-channel structure in AIA EUV and sigmoid in X-ray images. Reforming HCS/sigmoid was almost identical in appearance. HCS and sigmoid are considered as an observational proxy of magnetic flux rope (MFR). Long, sheared and twisted magnetic field lines along the SW-PIL were found in our extrapolation results. Therefore, we believe that an MFR was formed and existed before each eruption. Chatterjee & Fan 2013 studied the emergence of twisted flux rope in magnetohydrodynamic simulation. They suggest that the partial eruption and reformation of MFR can produce homologous eruptions. In their simulation, reformed MFR was appeared as X-ray sigmoid. In the present case, flux emergence was going on before the first eruption. It is possible that the erupting MFR, before the first eruption, could have emerged from the sub-photosphere. However, since there were continuous shearing motion and flux cancellation in the SW sub-region, spanning the three eruptions. Also, after partial eruption an erupting magnetic structure of similar morphology was reformed. Therefore we believe that, most probably the shearing motion and flux cancellation were the primary mechanisms that formed the erupting MFR along the SW-PIL.

At last, we want to discuss about the identical precursor phase (PP) activity in the AR. It was identified as a confined flare surrounding an island of positive flux at the left side of the SW sub-region. A complex magnetic configuration, semicircular quasi-separatrix layers (QSLs), was inferred to exist in the region. The magnetic configuration was almost the same before each eruption, we believe this was due to the reformation of identical magnetic structures in the region. It is arguable that the identical PP was due to reconnection at identically shaped QSLs, either due to flux emergence or shifting of the island itself. As

a strong overlying magnetic strapping force, due to overlying magnetic field, was inferred above the MFR lying along the SW-PIL. Our study suggests that the PP flare facilitated the eruption by removing the overlying magnetic strapping force above the MFR.

Chapter 5: An atypical scenario: Compound Eruptions

Solar eruptions, manifested as flares and coronal mass ejections (CMEs), remove the stored free magnetic energy from the Sun. They are the main sources of disturbances in interplanetary space and the driver of space weather near the Earth. A typical solar eruption has three phases: (1) the precursor phase, observed as small bump in the X-ray profile, (2) the impulsive phase (IP), observed as sharp rise in the X-ray profile and (3) the gradual phase, observed as gradual decrease of X-ray profile. These variation in X-ray profiles are associated with three distinct acceleration phases of CMEs (Zhang et al. 2001).

In some instances, multiple solar eruptions happen within a short period of time; such eruptions are known as sympathetic eruptions. Sympathetic eruptions may occur at different ARs or within same AR with different polarity inversion lines (PILs). It is debatable whether these consecutive eruptions are related to each other (Biesecker & Thompson, 2000). Interrelation among sympathetic eruptions has been shown in the simulation work by Török et al. (2011). In their 3D MHD simulation, the eruption of one filament can weaken the overlying magnetic pressure sufficiently leading to the eruption of the other filaments. There is a high chance of interaction among the CMEs when they occur in close proximity and/or within a short period of time. The study by Gopalswamy et al. (2002) found that the interaction among the CMEs could be an important factor for the SEP production. For a complex AR, with multiple PILs, MFRs could be formed along the different PILs and they could erupt consecutively (e.g., Chintzoglou et al. 2015).

There are also cases where instead of having a single MFR along the PIL, two MFRs could be formed along the same PIL (e.g. Liu et al. 2012). The two MFR arrange themselves in a double-decker (DD) configuration: one lying above the other along the same PIL. Unlike a partial-eruption, where splitting of erupting MFR results in the eruption of only a part

of MFR, in a DD configuration the lower and upper structures are observed to exist well before the commencement of the eruption. Observation of the DD system is very rare and study of such atypical magnetic configuration is important to understand i) how and why the DD system is formed?, ii) how the DD system erupts from the Sun?

In this study, we analyze solar eruption SOL2012-03-10T16:50:00L303C17, which is associated with a single flare (M8.5) and a single CME. However, the flare contains two peaks in its IP separated by only 12 minutes, and the eruption contains two different erupting structures sharing the same PIL. We name this type of eruption a ‘compound eruption’, i.e. two closely connected magnetic structures erupting consecutively within a short time interval forming a single flare and a single CME. The compound eruption studied in this paper originated from NOAA AR 11429 on 2012 March 10. The study of the photospheric magnetic structure showed that the shearing and converging motions lead to the flux cancellation and new connectivity in the corona. These processes resulted in the formation of two MFR candidates, which were arranged in a DD configuration. The chapter is structured as follows. The compound eruption is described in Section 5.1. The evolution of the AR prior to the eruption and the pre-eruptive configuration are analyzed in Section 5.2, and the discussion and conclusion are presented in Section 5.3.

5.1 Observations of the Compound Eruption

NOAA AR 11429 was a mature AR when the eruption under study occurred. It was located near the center of the solar disk (N17E01) and had very complex magnetic configuration ($\beta/\gamma/\delta$). The compound eruption began on 2012 March 10, around 16:54 UT, in the southwest (SW) part of the AR. The X-ray profile of the eruption had three distinct peaks; all three peaks were also shown in AIA pass-bands (see Figure 5.1). The flare could be divided in three phases: precursor phase, impulsive phase and gradual phase. However, unlike typical flares (of which time profiles are single peaked), this flare exhibited two peaks during the impulsive phase (pointed by two black arrows in Figure 5.1. AR 11429 had two

pre-eruptive hot-channel structures and corresponding filaments on the SW side of the AR. These structures are called hot-channel structures as they are observed in hot passbands of AIA i.e. 94 Å (6 MK) and 131 Å (10 MK) (e.g., Zhang et al. 2012). These two hot-channel structures (and associated filaments) were lying one above another along the same PIL in a Double-Decker (DD) configuration (detailed study of the pre-eruptive configuration is in 5.2.3). Hereafter, the higher-lying hot-channel structure would be referred to as “Hot-Channel Structure A” (HCSA), and the lower-lying hot-channel structure as “Hot-Channel Structure B” (HCSB). We also refer to the higher-lying filament as “filament-A” and lower-lying filament as “filament-B”.

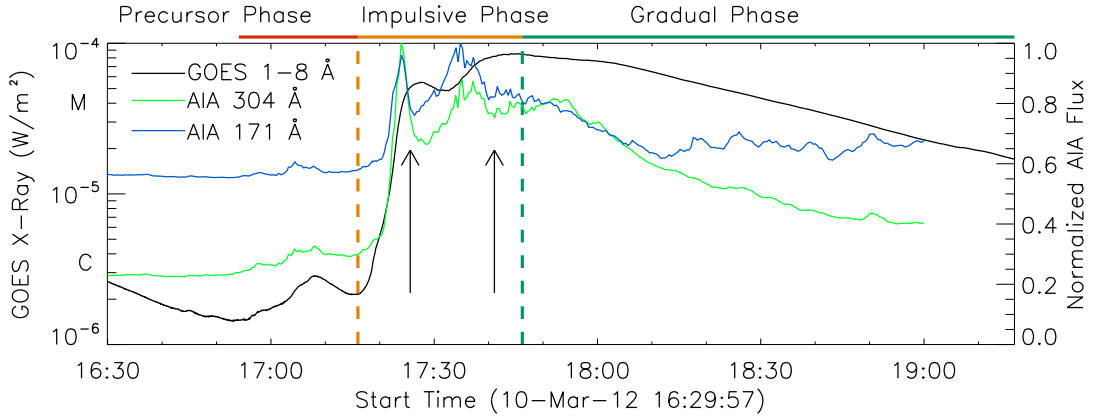


Figure 5.1: The three phases of the compound-eruption. The black curve shows the SXR time-profile observed by GOES. The colored lines show the intensity plot for different AIA passbands. The vertical-dashed lines indicate the beginning and ending of the impulsive phase. The two peaks in the impulsive phase are pointed by two black arrows.

5.1.1 The Precursor Phase

The precursor phase is defined as the time period during which a small amount of energy is released just prior to the impulsive phase (main energy release phase) of the solar eruption

(e.g., Zhou et al. 2016). Generally, a small peak is observed in the time profile of the SXR flux in the precursor phase, which marks the initiation or slow rise phase of the associated CME (Zhang & Dere 2006). During the precursor phase of this event, brightenings were observed in-between the two filaments, starting at around 16:33 UT. After that moment the whole HCSA became bright in 131 Å (Figure 5.2(a); an online movie is accompanied with Figure 5.2). Brightenings could have been due to the interaction between the two filaments. Evidences for such interaction have been observed in previous study of DD structures (Liu et al. 2012). The region near the left elbow of the HCSA was intensely brighter than the rest of the HCSA structure. In AIA 1600 Å there were sporadic brightenings underneath along the HCSA, which later concentrated more towards the left elbow of the HCSA around 17:08 UT (Figure 5.2(f)). The study by Cheng & Ding (2016) of erupting sigmoidal structures found that the initial sporadic brightenings of the flare-ribbons marked the slow rise phase of the erupting sigmoidal structure. Brightenings in 1600 Å during the precursor phase may indicate the instability and the slow rise of the HCSA of the DD configuration. The slow rise may in turn indicate the initiation-phase of the solar eruption; this is observed as a small peak in the SXR time profile in this event. The intense brightening at the left elbow of the HCSA might be due to the interaction of the rising HCSA with the overlying magnetic fields. Such activities could result in the weakening of the strapping force from the overlying magnetic fields.

5.1.2 The Impulsive Phase

The Impulsive Phase (IP) of a solar eruption is the phase of main energy release. It is characterized by a sharp increase in soft X-ray flux and fast acceleration of the erupting structure (Zhang & Dere, 2006). The onset of IP for the compound eruption of 2012 March 10, started at 17:16 UT with the acceleration of HCSA (the latter shown with green asterisks in AIA 131 Å images in figure 5.3). The onset of IP was also observed as an intense and continuous brightening in AIA 1600 Å along HCSA. As the IP progressed, the HCSA lifted

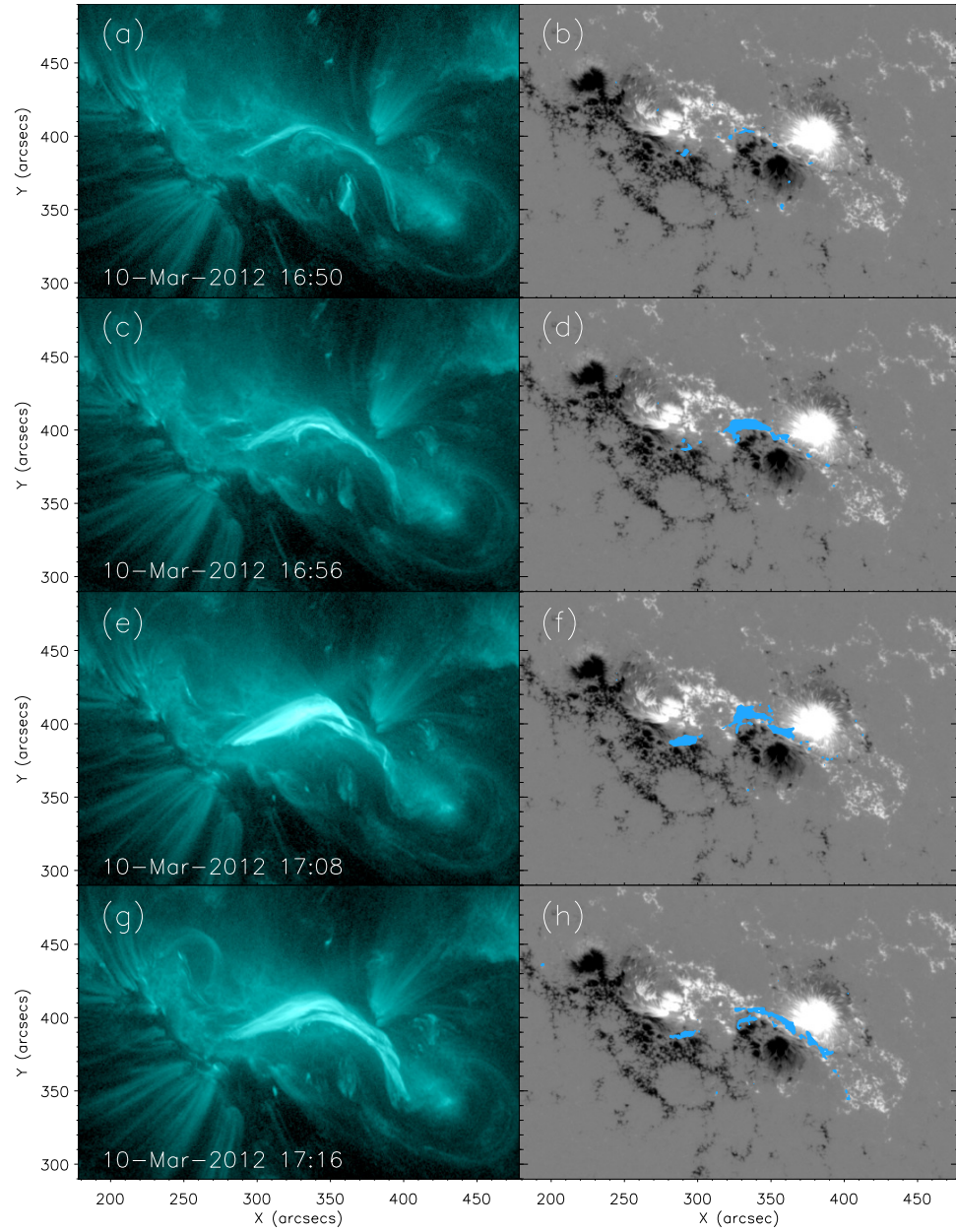


Figure 5.2: The precursor phase of the compound eruption. The left four images show the change of the hot structure in AIA 131 Å during the precursor phase. The right four panels show the flare-ribbon evolution during the pre-flare phase in 1600 Å (blue contours), plotted over HMI/LOS magnetograms (gray scale).

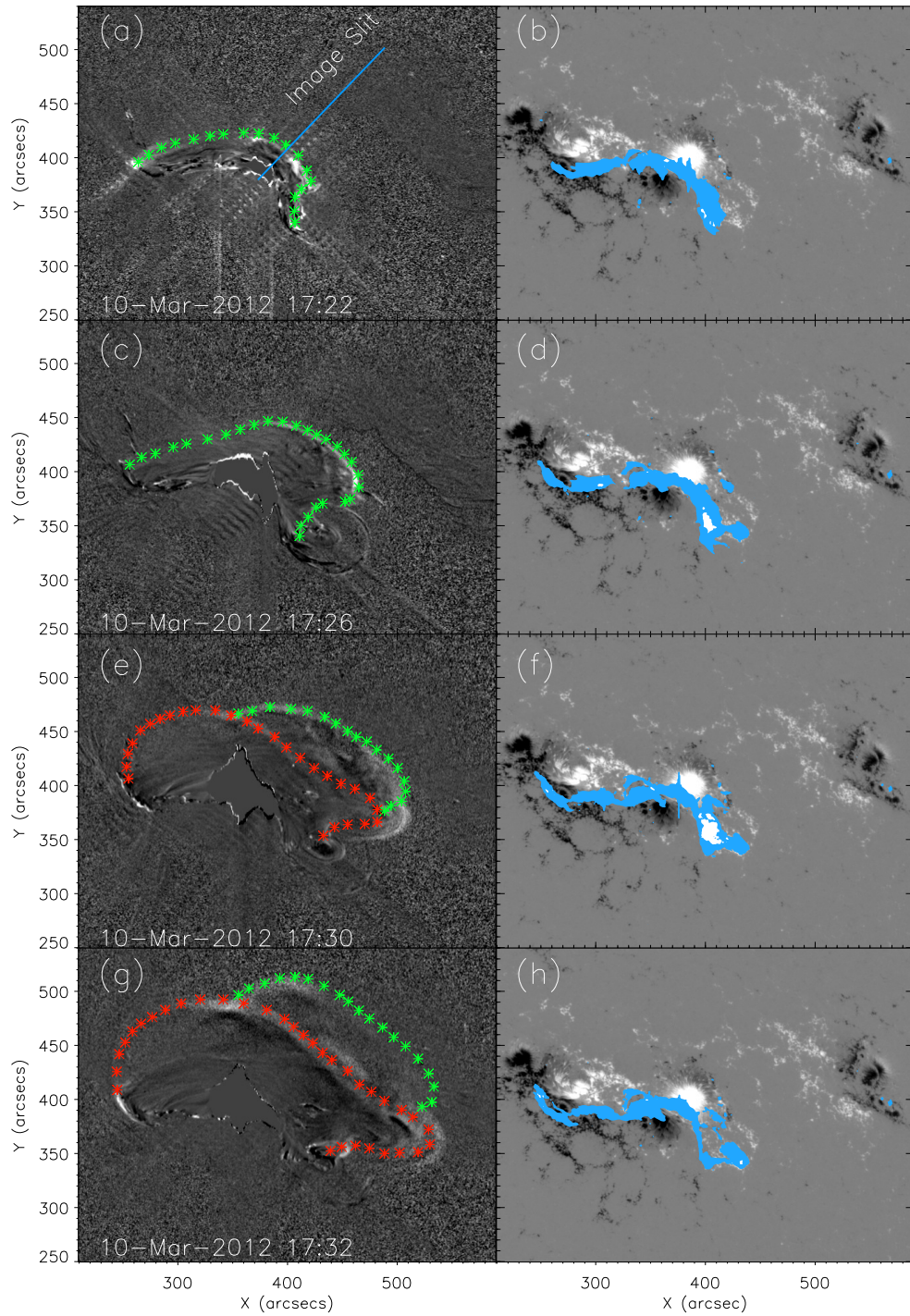


Figure 5.3: Evolution of the compound eruption during the impulsive phase. The left four panels are showing the running difference images for the AIA 131 Å and the right four panels are showing the flare-ribbon evolution, over-plotted over magnetogram, in AIA 1600 Å in blue. The erupting HCSA and HCSB are shown in green and red asterisks respectively. The blue line in panel (a) is the position of the slice used for the study of kinematic evolution of two erupting structures.

to higher heights, accompanied by separation of ribbons seen in 1600 \AA and simultaneously to the rising & writhing of filament-A (an online movie is available for a better view of the evolution). This series of events accompanying the acceleration of HCSA occurred during the first IP-peak in the SXR profile (first black arrow on the left in Figure 5.1).

The HCSB began rising at around 17:23 UT. The fast acceleration of HCSB followed at 17:29 UT as seen in AIA 131 \AA (shown with red asterisks in the Figure 5.3). With the acceleration and rise motion of HCSB, new sets of flare ribbons were observed which were accompanied by the rising filament-B (see online movie showing the filament eruption). The second peak in the SXR profile during IP (second black arrow in Figure 5.1) is associated with the rise of HCSB. The eruption of the two hot-channel structures of DD configuration were separated in time and thus were observed as two peaks in the IP of the SXR profile.

To quantitatively study the rising motion of the erupting structures, we chose an image slit, shown by the blue line in Figure 5.3(a), and made a time-stacking plot along this slit. In the stack-plot (see the Figure 5.4(a)) we can clearly identify the eruption of two hot-channel structures of the DD configuration. The position of the outer edge of HCSA is shown with green asterisks in the plot in Figure 5.4(a). The velocities obtained from these points indicate that the HCSA has undergone two acceleration phases. The first acceleration phase corresponds to the first peak of IP, and HCSA accelerated the second time when HCSB erupted. The interaction between HCSA and HCSB seems to be responsible for the second acceleration phase of HCSA. HCSA had the second acceleration phase around 17:28 UT. The second acceleration phase also coincided with an increase in the normalized intensity of AIA 304 \AA (Figure 5.4(b)). The velocity time profile of the HCSA and the intensity profile of the flux in AIA 304 \AA showed that the fast acceleration of the HCSB started at 17:28 UT, 12 minutes after the fast acceleration of HCSA. Afterwards the two structures appear to be moving with the same velocity. The eruptions of the two structures were observed as a single CME in SOHO LASCO/COR2 coronagraph images (Figure 5.5).

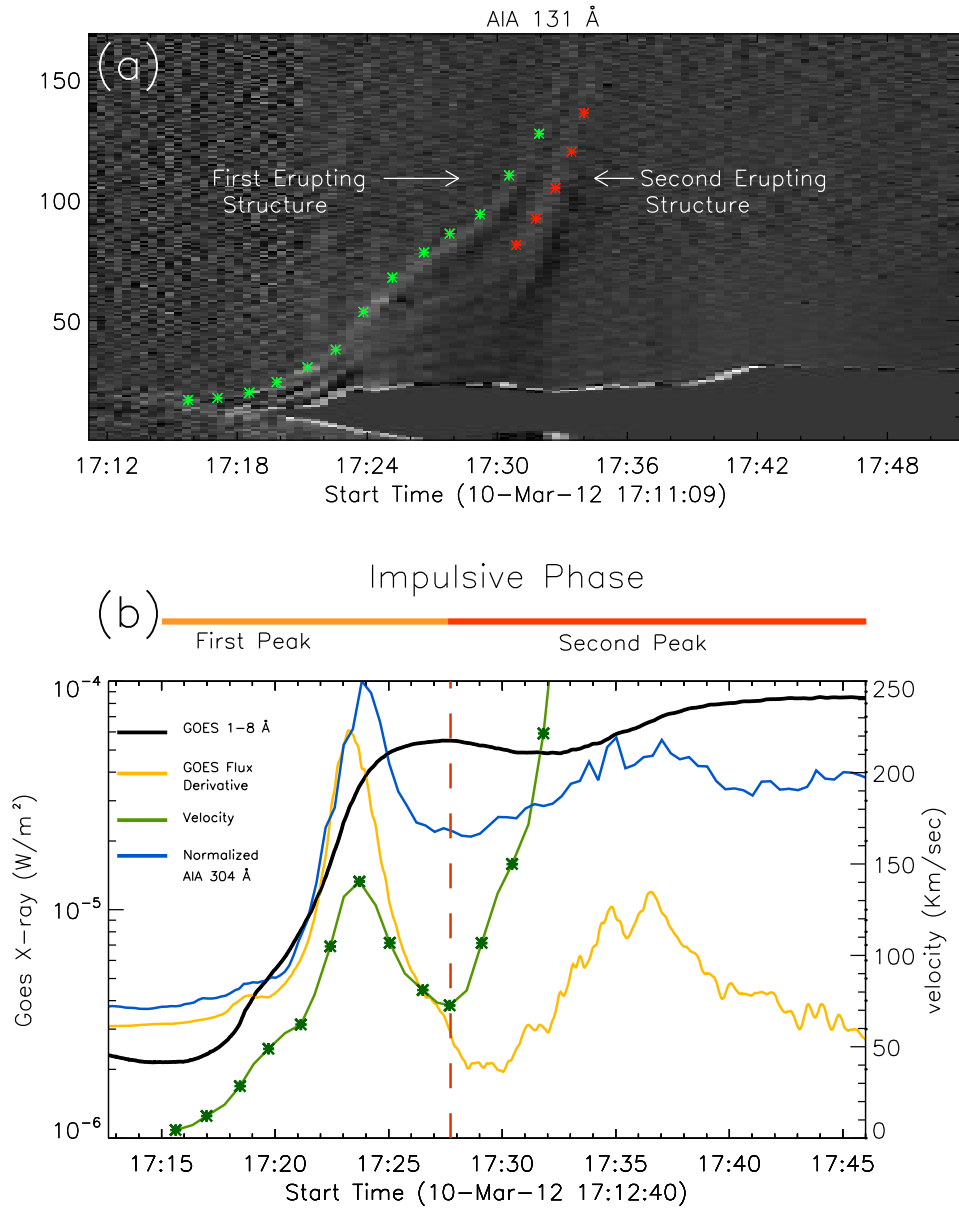


Figure 5.4: Kinematic evolution of erupting structures. (a) The time-stacking plot obtained from the running difference of AIA 131 Å images (the position of the slice is shown in the Figure 5.3(a)). The green asterisks mark the positions of the outer edge of the erupting HCSA and the red asterisks mark the position of the outer edge of the erupting HCSB of DD configuration. The two erupting structures are clearly resolved. (b) The black curve is the GOES SXR profile and blue curve is showing the normalized AIA 304 Å intensity. The green curve is showing the velocity variation of HCSA during the impulsive phase, it has two acceleration phases. The curve in yellow is the derivative of GOES flux. The vertical line is showing the starting time of the second acceleration phase of HCSA and it corresponds to the second increase in the intensity of the AIA 304 Å.

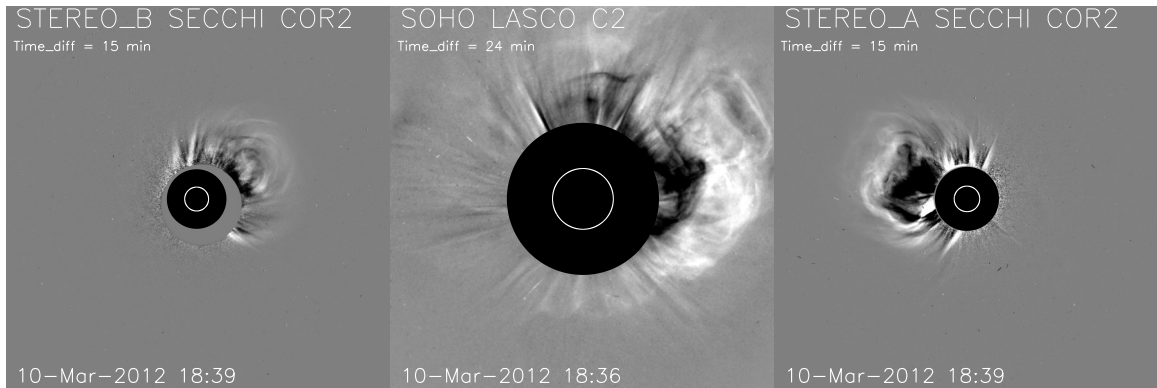


Figure 5.5: The CME resulted from the compound eruption observed from three different points of view. The three panels from left to right show COR2 image from SECCHI/STEREO-B, C2 image from LASCO/SOHO and COR2 images from SECCHI/STEREO-A, respectively.

5.2 Observations of the Pre-Eruption Evolution

The AR 11429 was very active in terms of number and intensity of solar eruptions since it appeared on the eastern limb; it had produced 48 C-class, 15 M-class and 3 X-class flares during its transit across the solar disk. This super-activity seems to be associated with its very complex magnetic configuration; δ -spot and anti-hale configuration (see, Elmhamdi et al. 2014 for the evolution of the magnetic configuration). The following sub-sections describe the pre-eruption evolution and magnetic configuration before the onset of the compound eruption on March 10, 2012.

5.2.1 Evolution of the Photospheric Magnetic Field

To study the evolution of the magnetic configuration of AR 11429 we made use of preprocessed cutouts of the HMI magnetograms. The preprocessing resolves the 180° azimuth ambiguity and remaps helioprojective images into Cylindrical Equal Area (CEA) projection, where each pixel has same surface area (Hoeksema et al. 2014). We focused on the time range between March 9, 04:00 UT to March 10, 19:00 UT. This large and complex AR could be divided into two sub-regions, NE and SW sub-regions (shown with boxes in

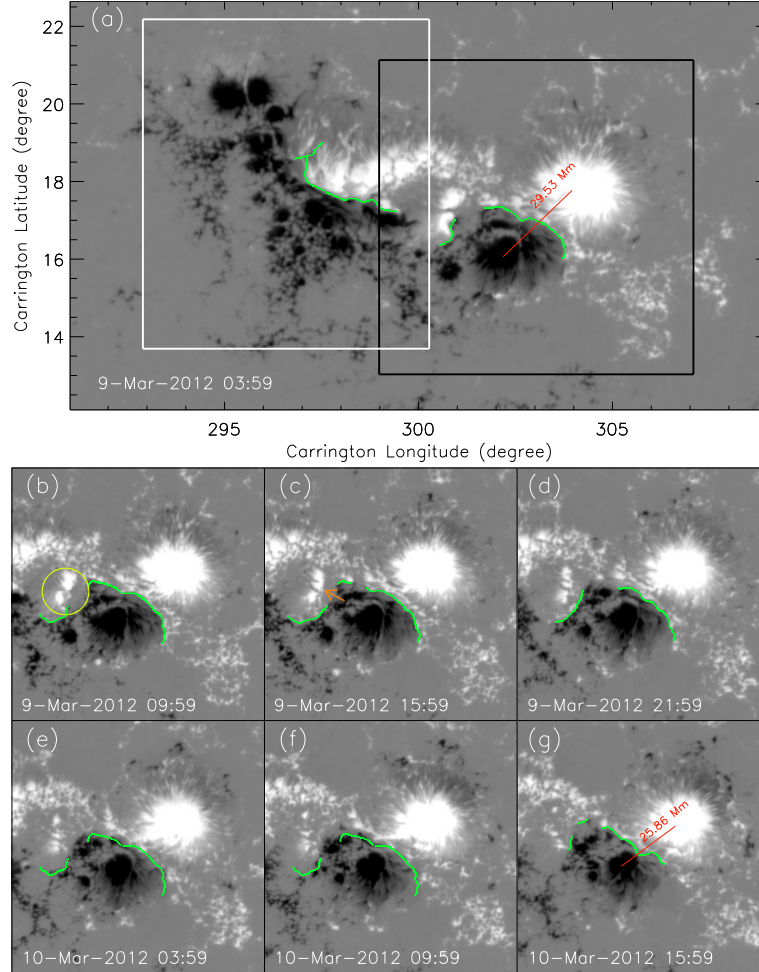


Figure 5.6: Evolution of the photospheric magnetic field in NOAA AR 11429. Images are taken from the LOS magnetograms of SDO/HMI and are shown in CEA heliographic projection. Green lines are the strong-gradient polarity inversion line (PIL). Top panel (a) shows the entire AR, white and black boxes show the NE and SW sub-region respectively. Panels (b)-(g) show the evolution of the magnetic configuration in the SW part of the AR. Red lines, in panel (a) and (g), show the distance between the centroid of two strong bipoles. The yellow circle in panel (b) is the location of prominent flux cancellation. The orange arrow in panel (c) is the direction of motion of negative flux.

Figure 5.6(a)). Both of the sub-regions had contained a long and sharp strong-gradient PIL (shown in green lines in Figure 5.6; obtained from an image gradient operation as detailed in Zhang et al. 2010). The compound-eruption on March 10 happened in the SW sub-region of the AR, whose evolution is shown in the Figure 5.6. The PIL in the SW sub-region was located in between two very strong opposite polarities. We measured the centroid of positive (negative) flux greater (smaller) than 500 G (-500G) in the SW sub-region. During the evolution of AR 11429, the distance between the centroid of the two opposite polarities (shown by red lines in Figure 5.6(a) and (g)) in SW sub-region decreased from ~ 29.53 Mm to ~ 25.86 Mm, indicating the convergence motion of the two poles. The convergence of the two poles was accompanied by fragmentation and diffusion of the magnetic flux, which resulted in further collision and cancellation of opposite flux along the PIL (see movie accompanying the Figure 5.6). Flux cancellation happened along the entire PIL, however it was most noticeable for the chunk of positive flux on the left side of the SW sub-region (shown with a yellow circle in Figure 5.6(b)). The cancellation along the PIL suggests an increase of the free magnetic energy and has been associated with the formation of MFRs (van Ballegoijen & Martens 1989; Green et al. 2011). In addition, we observe shearing motions along the PIL (direction of motion is shown with an orange arrow in Figure 5.6(c)), which seemed to change the semi-circular shape of the PIL to a linear-like shape. Shearing motions are also thought to increase the free magnetic energy (e.g., Cheng et al. 2014) in active regions. Thus, the flux-cancellation and shearing motions suggest an enhancement of the free magnetic energy in the region and created the magnetic structure pending for eruption.

5.2.2 Evolution of the Pre-eruption Structure in the Corona

During our observing period of 39 hours between March 9, 04:00 UT and March 10, 19:00 UT, many small and transient brightenings and confined flares occurred in the AR, including three confined C-class flares. This type of activity was mainly confined to the left side of the SW sub-region. There were also sporadic brightenings at the right-side of the SW sub-region.

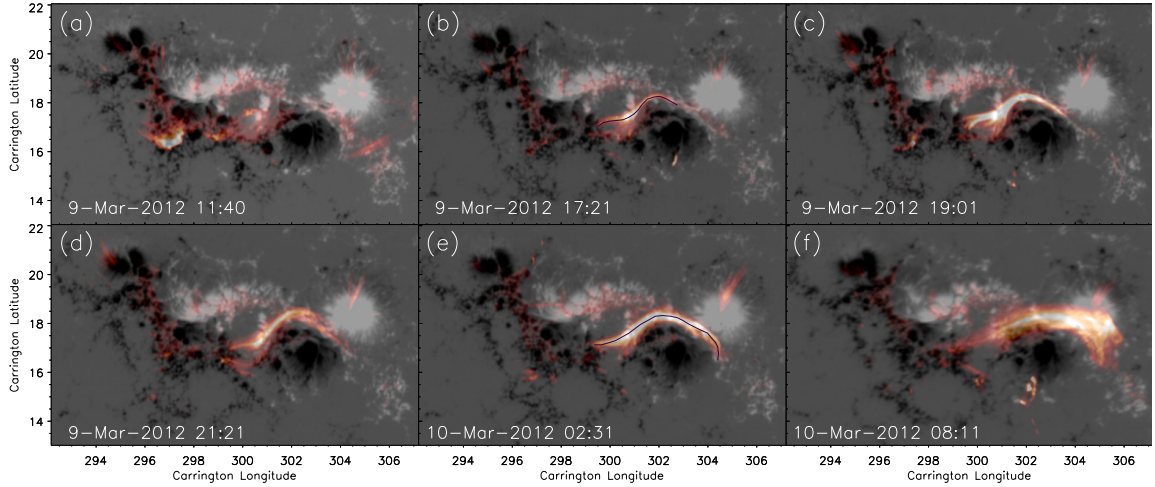


Figure 5.7: Evolution of the coronal hot-structure before the eruption in NOAA AR 11429. AIA 131 \AA passband data are shown in red-white, and the HMI data are shown in white (positive flux) and black (negative flux). In panels (b) and (e) the coronal hot-structures are also traced with dark lines.

Specifically, during that period (see Figure 5.7) we did observe the brightenings of coronal structures lying along the PIL. The intermittent brightenings in the AIA 131 \AA along the PIL indicated the presence of low-lying coherent coronal structures, which brightened up during the small confined flares (see Figure 5.7). As the AR evolved, the length of the hot-structure grew in size. We transformed the helioprojective images to Carrington projection and estimated the length of hot-channel structure. The length was ~ 45 Mm on 2012 March 9, at 17:21 UT and ~ 76 Mm on 2012 March 10, at 02:31 UT (see Figure 5.7(b) and (e)) as revealed by confined flares. In the corona, the length of the non-potential magnetic field lines could increase due to the tether cutting mechanism during small flare events when new connectivity could form. In the SW sub-region of the AR, converging and shearing motions may have facilitated the tether cutting reconnection and thus increase the length of the hot-channel structure. Chintzoglou et al. (2015) observed a similar kind of flare activities, small transient brightenings and confined flares, during the formation of MFRs.

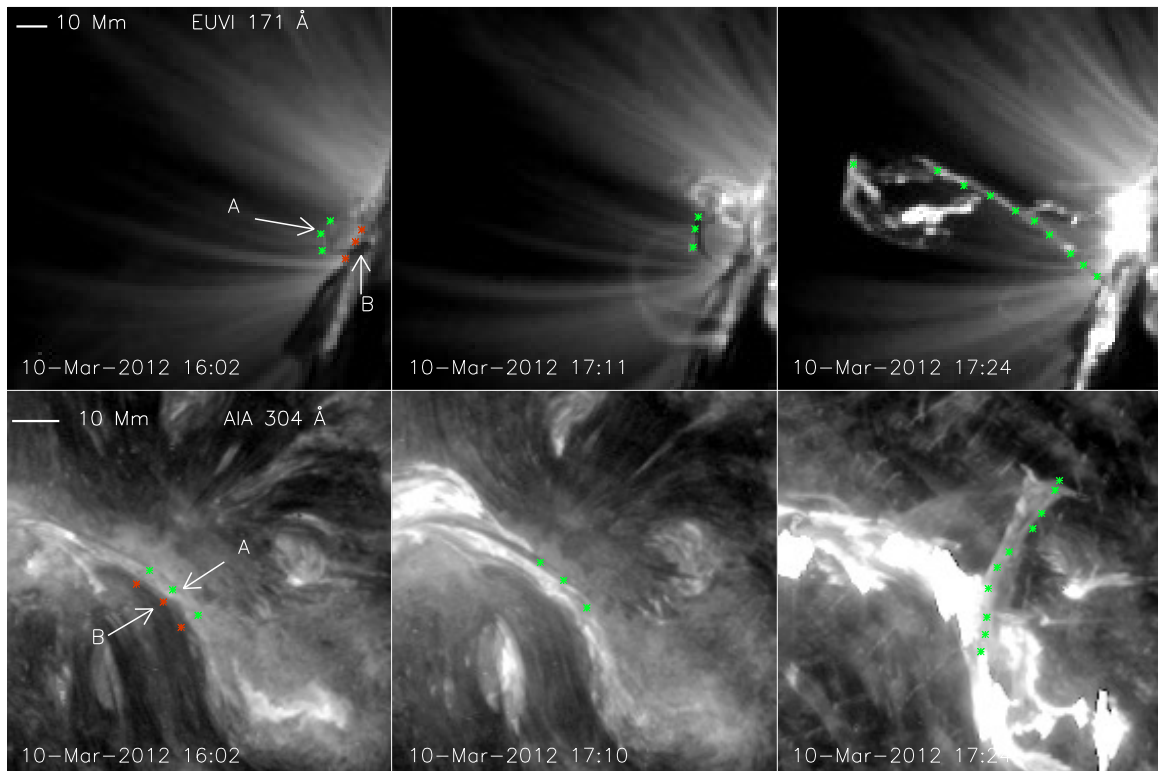


Figure 5.8: Two erupting filaments/prominences in a double-decker configuration. The upper filament (A) is marked with green asterisks and the lower filament (B) with red asterisks. The upper three panels show the filaments at different time in *STEREO-A* EUVI 171 Å. The lower three panels show the two filaments in *SDO* AIA 304 Å.

5.2.3 Observations of the Double-Decker Configuration

Long before the eruption on March 10, an underlying filament seemed to exist along the SW-PIL. It was revealed when the hot post-flare loops, the product of an earlier eruption on March 9, at $\sim 03:30$ UT, faded away. The existence of the filament shortly after the eruption, suggests that the filament either didn't erupt or erupted only partially. Around one hour prior to the compound eruption on March 10, we observed two filaments in the SW part of the AR, clearly seen from the *SDO* point of view (POV) (Figure 5.8). In the *SDO* POV, the two filaments seem to be in very close proximity to each other; one filament (filament-A) was lying slightly off the SW-PIL and the other (filament-B) was lying along the SW-PIL. Coronal structures above the solar disk were observed to deviate more and more from the PIL as they rose higher in the corona (Cheng & Ding, 2016), suggesting that filament-A was probably lying higher in the corona than the other filament-B. To determine the geometry of the two filaments, we made use of the *STEREO-A* observations of the same two filaments. For a specific point in one image, the *sec_measure* IDL routine (available in SolarSoftware Package; Freeland & Handy 1998) calculates the 3-D line of sight as observed by one vantage point (e.g. *SDO*) and then draws the projection of this line into second image (e.g. *STEREO* at an angle of 109.7°). The projected line from the second satellite is known as *epipolar line* (see Inhester 2006). Then the user can identify the location of features selected in the first image (*SDO*) onto the second image (*STEREO*) along this epipolar line. The 3-D positions of the two filaments determined from such multiple viewpoint measurements show that they are indeed in a double-decker configuration (see Figure 5.8). The separation along the vertical direction between the two filament was found to be ~ 12 Mm on 2012 March 10, at 16:02 UT. The study by Liu et al. (2012) had observed similar (~ 13 Mm) separation between the two filaments of DD configuration.

Since there was no apparent flux emergence in the sub-region during the period of our observation, one can refute the idea of emergence of lower magnetic structure below a higher lying magnetic structure to form a DD configuration. Also, both parts of DD

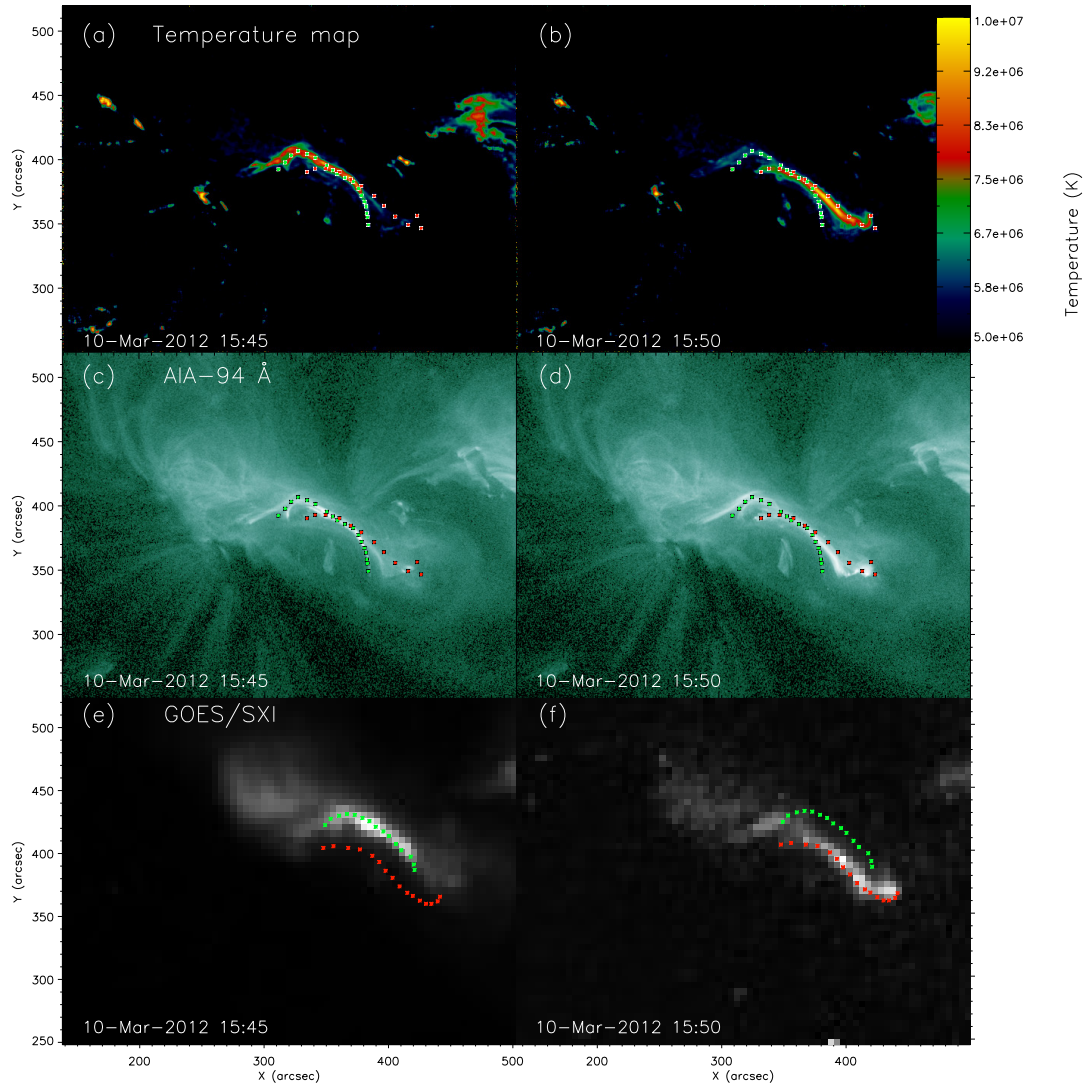


Figure 5.9: Images illustrating the two hot-channel structures of the double-decker configuration in the SW region of the AR 11429. Panels (a) and (b) show the temperature map obtained with a DEM method. Panels (c) and (d) show the images in AIA 94 Å. Panels (e) and (f) show two hot coronal structures in X-ray images from GOES/SXI. The green and red asterisks show the high-lying and low-lying structures respectively.

were visible well before the initiation of the compound eruption, therefore the present case was different from the partial-eruption scenario where a single flux system divides into two parts during the eruption. It is possible that the flux-cancellation and shearing motions have played a role in the formation of the DD structures. Considering the initially stable configuration of the two structures, it is also possible that the axial currents in lower and upper magnetic structures (or branches) flow in the same direction with respect to each other and the interaction between the filaments may be attractive in nature due to the $\mathbf{J} \times \mathbf{B}$ force as suggested by Kliem et al. (2014). Liu et al. (2012) had observed plasma being transferred from lower to the upper filament. This so-called filament-filament interaction, in DD, was also reported in the study by Zhu et al. (2015). Here, we also observed intermittent brightenings between the two filaments in AIA/*SDO*, which may suggest possible interaction between the two flux systems. From the POV of *SDO* the separation between the filaments was so small that any plasma mass transfer could not be discerned easily. However, we speculate that there may be mass transfer between the two structures.

Distinguishing the DD structures clearly in the AIA passbands against the strong on-disk background emission was a very challenging task. However, intermittent brightenings occurring at different times show two different hot-channel structures along the SW PIL (see the Figure 5.9). The temperature map, obtained from the DEM method (following Cheng et al. 2012; see Figure 5.9(a) and (b)), showed that the temperature of these structures was > 7 MK. Hot-channel structures were also visible in SXR images obtained by SXI/GOES (see Figure 5.9(e) and (f)). The foot-points of the two hot-channel structures were in close proximity to each other, however they were clearly different. Comparing the locations of the two hot-channels (AIA 94 Å; Figure 5.9 (c) and (d)) with the two filaments (seen in AIA 304 Å; lower panels in Figure 5.8), we found that the structure marked with green asterisks (Hot-Channel Structure A; HCSA) corresponds well to filament-A and the structure marked with red asterisks (Hot-Channel Structure B; HCSB) corresponds to the lower filament-B.

5.2.4 Coronal Magnetic Field Inferred from NLFFF Extrapolation

Solar eruptions are magnetic in origin so in order to better understand the associated mechanisms, it is crucial to study the magnetic configuration of the ARs (with the aid of modeling). The location of the AR 11429 on the solar disk made it a suitable candidate to study the coronal magnetic field through magnetic field extrapolation. In the solar corona the magnetic pressure is much higher than the plasma pressure and thus we can assume that the magnetic field lines satisfy the force-free field approximation (see Wiegmann & Sakurai 2012), i.e., $\mathbf{J} \parallel \mathbf{B}$ and $\nabla \times \mathbf{B} = \alpha \mathbf{B}$. Here, α is the force-free parameter and is constant along each magnetic field line; however it varies over different field lines in the case of Non-Linear Force-Free Fields (NLFFF). To get the NLFFF extrapolation of coronal magnetic field, we use an optimization numerical approach developed by Wheatland et al. (2000) and later extended by Wiegmann (2004). In this iterative optimization process, a “penalty function” $L = \int_V w(x,y,z) \left[\mathbf{B}^{-2} |(\nabla \times \mathbf{B}) \times \mathbf{B}|^2 + |\nabla \cdot \mathbf{B}|^2 \right] d^3x$ is minimized, where w is a weighting function (Wiegmann, 2004). For the bottom boundary of the domain, we use HMI vector magnetogram cutouts. These data were preprocessed to make them suitable for the force-free condition (Wiegmann et al., 2006). The NLFFF extrapolation was done for the entire area containing AR 11429 at every hour from 2012 March 9, 04:00 UT to 2012 March 10, 17:00 UT.

The horizontal magnetic field in the PIL was aligned along the PIL length, indicating the presence of a strong non-potential shear along the PILs (Figure 5.10(a)). Using the extrapolated 3D cubes and the PARAVIEW 3D visualization tool, we analyzed the evolution of the vector magnetic field in the corona. We found sheared and weakly twisted magnetic field lines above the PILs in the AR. In the NE sub-region, the sheared coronal magnetic field lines remained more or less unchanged throughout the period under study (short sheared lines shown in brown in Figure 5.10(b)). In the SW sub-region, however, there were different groups of sheared and twisted magnetic field lines. With time, a system of long, sheared and twisted magnetic field lines above the PIL appeared in the modeled corona data, before

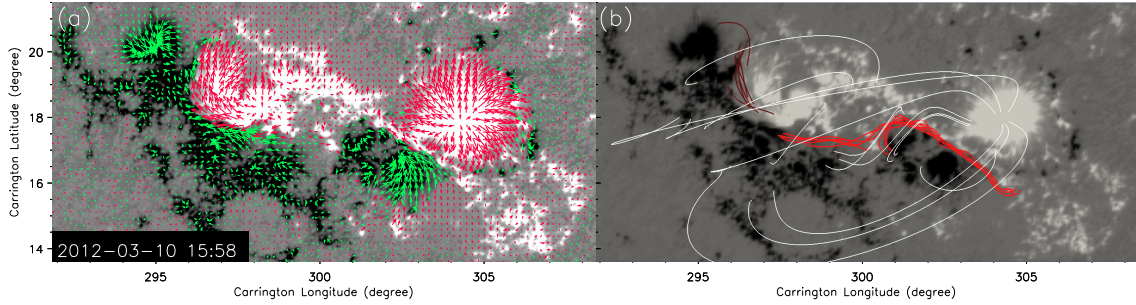


Figure 5.10: Magnetic field configuration in the AR 11429 at 15:58 UT on March-10, 2012, immediately before the eruption. The background shows the B_z component of the vector magnetogram with positive (negative) flux in white (black). Panel (a) also shows the direction of horizontal magnetic field at the photosphere in red and green. Panel (b) shows selected magnetic field lines in the AR above the photosphere obtained from the NLFFF extrapolation. Sheared magnetic field lines along the NE-PIL is shown in brown. The sheared and twisted magnetic field lines, along the SW-PIL, is shown in red. The white lines show the overlying magnetic field in the corona.

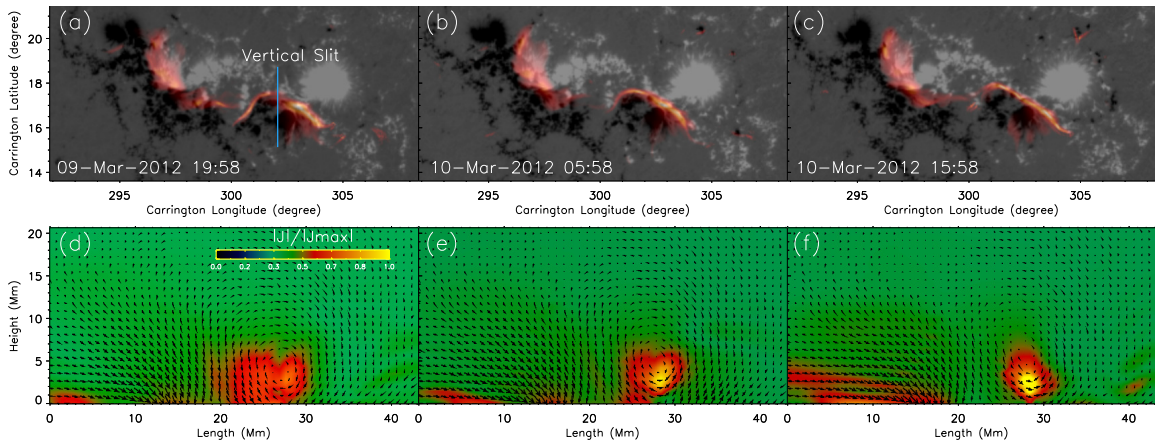


Figure 5.11: Evolution of coronal current density (obtained from the NLFFF extrapolation) in the AR 11429. Panels (a)-(c) show the normalized-integrated current density along the LOS in red-white and the B_z component in the background. Panels (d)-(f) show the vertical slice of the current density along the blue line (top left panel). During the evolution, the current density changed from more diffused to more concentric around the location of the hot channel.

the compound eruption on 2012 March 10 (shown in red in Figure 5.10(b)). The evolution of magnetic field lines was also evident from the evolution of the current density of the AR (more in the following paragraph).

We calculated the current density in the AR as $\mathbf{J} = \nabla \times \mathbf{B}/\mu_o$ for the entire extrapolated domain. Along the PILs we observed very high current density. The presence of current density signifies non-potential magnetic fields. Due to Ohmic heating, regions of higher current density are hotter than the neighbouring regions. These regions are observed as diffuse and sigmoidal structures in the AIA hot-channel passbands. In the NE sub-region, the high current-density region was more diffuse and remained unchanged during the evolution of the AR. In the SW sub-region, on the other hand, the shape of the high current-density region changed significantly over time (see upper panels of Figure 5.11, corresponding to the change in SW-PIL in the Figure 5.6) and also became more concentrated (see lower panels of Figure 5.11). The change of the high current-density region from a more diffuse to more concentrated current distribution indicated the formation of long, sheared and twisted magnetic field lines above the photosphere as displayed in the extrapolation results. This is also seen in Chintzoglou et al. (2015) where the 3D current density before the formation of the MFRs was initially a system of fragmented current channels and over time became a single current channel structure.

The shearing motion and flux cancellation changed the magnetic configuration of the AR 11429. The extrapolation results showed that these changes were favourable for the formation of a long, sheared and twisted magnetic structure at the SW-PIL of the AR. There was one group of sheared and twisted magnetic field lines along the SW-PIL, shown in red in Figure 5.10(b), corresponding to a single concentrated current-density in lower-right panel of Figure 5.11. The DD configuration was not reproduced in the NLFFF extrapolated result. The lack of DD configuration in the extrapolation might be due to the fact that the lower and the upper branch of the DD formed during the temporal evolution. It is also important to note that the NLFFF extrapolation is producing static equilibria from snapshot image (coronal magnetic field for the photospheric boundary condition) of the magnetic

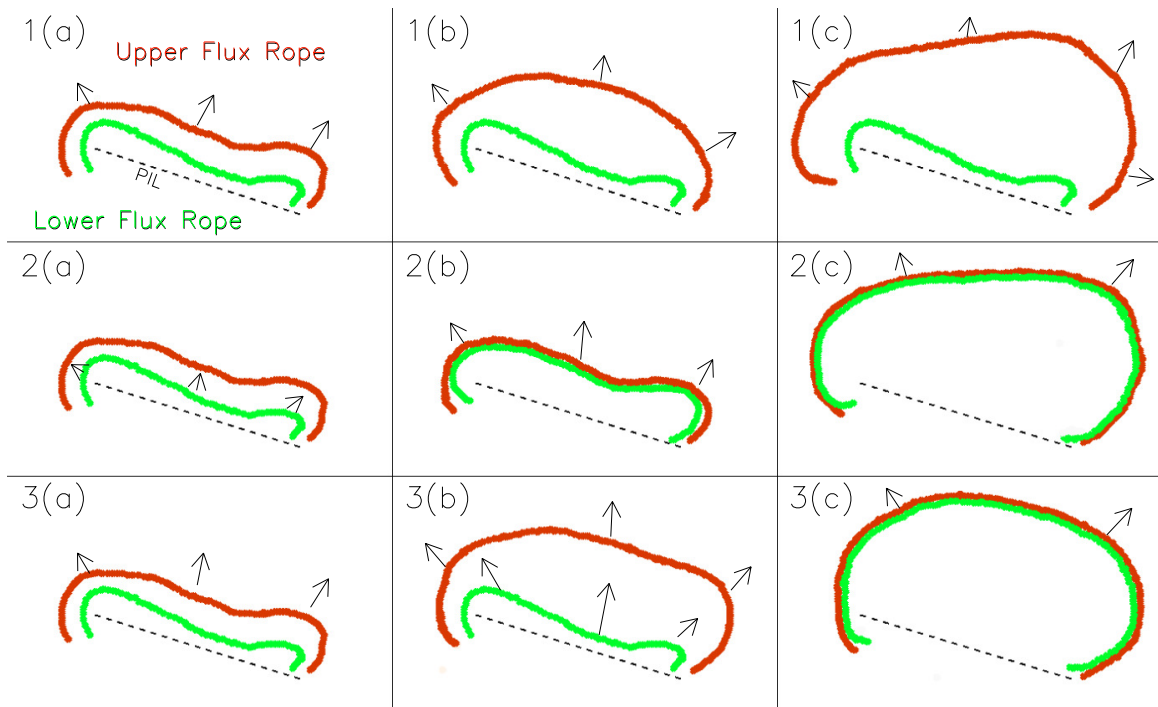


Figure 5.12: The three erupting scenarios of the double-decker (DD) configuration. 1) The upper three panels depict the case where only the upper-branch of the DD erupts. 2) The middle three panels show the merging of the two branches of DD, which erupts together. 3) The lower three panels show the eruption of the two branches of the DD separately and their interaction after the eruption.

field, thus the dynamics are not fully captured. Nevertheless, NLFFF extrapolation helps in understanding the magnetic distribution above the photosphere and slow quasi-static evolution to a first order.

5.3 Discussion and Conclusion

Our primary aim for the present study is to understand and explain the two peaks in the impulsive phase of the solar eruption from AR 11429 on 2012 March 10. It is a compound eruption, since it involves two closely-spaced magnetic flux rope candidates which successively erupted within a short time interval (12 min in this event). The compound eruption was associated with an M-class flare. We carried out a detailed study of the compound

eruption and the evolution of the AR for 39 hours leading to the eruption. Around an hour prior to the compound eruption, we observed two filaments lying along the same PIL on the SW sub-region of the AR.

The main result of the study is that the two peaks in the impulsive phase are caused by the eruption of two hot channel structures (as seen in 131 \AA corresponding to 10 MK plasma emission), which were likely in the form of a flux rope during or even before the eruption. Our analysis suggests that each erupting hot channel structure was preceded by an independent coherent magnetic structure which destabilized and erupted. Here, we call such eruption-capable pre-eruption magnetic structure a flux bundle, which is so named to emphasize its becoming coherent and independent long before (i.e., many hours or more than one day) the eruption, but without specifying whether such structure is a flux rope or not. Thus, both sheared structures and flux ropes can be considered as a flux bundle, as long as it becomes an entity of eruption at a later time. These two flux bundles were lying along the same PIL one above the other in a DD configuration. The instability and fast acceleration started first for the high-lying structure, then was followed by the instability and fast acceleration of the low-lying structure. The velocity of the low-lying structure was greater than the high-lying structure; as a result, the second structure reached the first and both interacted with each other to form a compound eruption. The eruption of the two flux bundles and the magnetic reconnection in the current sheet underneath them was responsible for the double peaks in the impulsive phase of the associated flare.

The present case is different from classical eruptive model where a single flux rope like structure erupts during the solar eruption and a single peak is observed in the SXR profile during the impulsive phase. A few previous studies consider the eruption of DD structures. The study by Liu et al. (2012) observed two filaments lying along the same PIL. They observed the instability and eruption of only the higher lying filament. Zhu et al. (2015) also studied the eruption of DD configuration. In their study the lower filament rose and merged with the upper filament and then the merged filaments erupted together. Unlike the previous studies, in this work, we observed the two components of the DD configuration

that destabilized and erupted at different times and then interacted with each other to form a compound eruption.

Based on the studies mentioned above, we can summarize that there exist three different scenarios for eruptions in a DD configuration (shown in Figure 5.12). They are: 1) Instability and eruption of only the high-lying magnetic structure (this is the partial eruption of DD configuration), 2) Instability and rise of low-lying magnetic structure and merging with the high-lying magnetic structure. Later on the merged structure erupts (this is a case of full eruption of DD configuration), 3) Instability and acceleration first of the high-lying magnetic structure followed by the instability and acceleration of the low-lying magnetic structure. The two erupting structures interact with each other forming a compound structure (this is also the case of full eruption). Cases (1) and (2) would be similar to the eruption of a single flux rope with single peak in IP. Only case (3) would result in two peaks in IP.

Kliem et al. (2014) studied two flux ropes in DD configuration through MHD simulations. Analytically, they found that the DD configuration remained in stable equilibrium if the toroidal component of external sheared field lines, lying above two flux ropes, had strength above a certain threshold value. The decrease in the strength of the toroidal component of the overlying sheared arcade would result in the instability of both of the flux ropes. Usually in such conditions the lower flux rope becomes unstable first and results in two cases: a) merging of two flux ropes and full eruption of the DD structure b) only the upper flux rope erupts and the lower flux rope gets destroyed due to reconnection with the ambient flux. For the case when the toroidal component of the overlying sheared arcade is above the threshold value, an eruption of the upper flux rope is possible if transfer of magnetic flux and current occurs from the lower flux rope to the upper flux rope. Such case also results in the eruption of the upper flux rope only (partial transfer of flux from bottom flux rope). However, in this case the lower one remains in place, possibly because it lost free energy by transferring it to the upper flux rope. In our case the interaction between the lower and the upper filament was observed as brightenings between them. During such interactions

it is possible that plasma, magnetic flux and currents got transferred from the lower to the upper flux rope. Normally, such transfer would have resulted into an eruption of only the upper flux rope, leaving the lower one undisturbed. However, the interaction of the erupting upper flux rope with the overlying sheared arcade might have reduced the toroidal component of the overlying sheared arcade. It is possible that this interaction resulted into the instability of the lower flux rope leading to a sequential eruption. This is one of the possible explanations of the observed eruption of double decker in the present case, but other explanations are also possible and should be addressed in a future study.

Finally, we would like to comment on the formation of DD configuration. The sub-flaring events during the evolution of the AR possibly increased the length of coronal hot-structures and formed flux bundles through magnetic reconnection. Wang & Zhang (2007) found that there is a low probability of having open eruption from the magnetic center of an AR due to strong overlying magnetic pressure. The SW PIL was lying between strong magnetic polarities which implies that there was strong overlying magnetic pressure over the coronal structure above the SW PIL. Due to that strong overlying magnetic pressure it was difficult for the magnetic structures to erupt. Cheng et al. (2014) observed the formation of a new flux rope below the existing flux rope due to shearing, flux cancellation and rotation of the leading magnetic polarity. Continuous shearing and flux cancellation in the AR may have resulted in the formation of a second flux rope which was lying low in the corona. Thus, strong overlying magnetic pressure and continuous shearing and flux cancellation below a higher lying flux bundle might have been responsible for the formation of a second lower lying flux bundle, forming the Double Decker (DD) configuration along the same PIL.

Chapter 6: Summary and Future Plans

6.1 Summary

This dissertation has improved our understanding of solar eruptions. It has addressed four topics. The first topic was understanding of physical processes responsible for multiple intense flares from ARs. The second topic was the quantification of drivers of solar flares using various magnetic field parameters. The third topic was understanding the formation of similar erupting magnetic structures and similar solar eruptions from the same solar region. The final topic was understanding atypical scenarios where multiple magnetic structures form along the same PIL and erupt consecutively. Each topic (with main results) is summarized as follows.

1. In chapter 3, the dissertation presents the analysis and comparison of the evolution of twenty ARs with different flare productivity and sunspot sizes. The study illustrates that magnetic flux emergence alone is not sufficient to produce multiple intense flares. New flux emergence can result in either the interaction of similar or opposite magnetic fluxes of non-conjugate pairs (magnetic poles not emerging together). In the first case, opposite magnetic poles would be far from each other, and the overall magnetic configuration remains simple. In such a scenario, the flare productivity of AR does not change with flux emergence. In the second case, the convergence of opposite magnetic fluxes of non-conjugate pairs results in continuous shearing motion and flux cancellation and a complex magnetic configuration. The study suggests that the long-term shearing motion and flux cancellation, along the PIL of non-conjugate pair, for a long time produces multiple intense flares.

2. In chapter 3, the dissertation also presents the analysis of the magnetic field parameters such as total magnetic flux, net flux, current density, current helicity, degree of current neutralization, lengths of strong-gradient PILs (sgPILs), and R-value to quantify the flare drivers. Our study found the weakest correlation (0.6) between flare index (FI) and total flux content of ARs. This demonstrates that the size of the AR does not necessarily determine the flare productivity. The correlation between the FI and sgPIL/ R-value was the strongest (0.8). Such a high correlation suggests that the ARs having long PIL for a long evolutionary period have a higher probability of producing multiple intense flares. Our study suggests that intense flare productive ARs have $\text{sgPIL} > 50 \text{ Mm}$ (in average) or $\text{R-value} > 4.5$.
3. In chapter 4, the dissertation presents the study of three homologous solar eruptions from NOAA AR 11429 over four days. The successive eruptions had occurred over different evolutionary phases, which provided a unique opportunity to isolate the physical processes responsible for solar eruptions. This study suggests that the shearing motion and magnetic flux cancellation of opposite fluxes are: (1) the dominant factors, irrespective of the evolutionary phases, that contribute to the recurrent homologous eruptions, and (2) the key processes of forming the erupting structure, likely a magnetic flux rope; their long-lasting continuation results in the reformation of identical erupting structures. The study also suggests that similar magnetic topology results in confined flares around the same location. Such flares (during the precursor phase) could help in the eruption by decreasing the constraints of the overlying magnetic field lines.
4. In chapter 5, the dissertation describes a compound solar eruption that was associated with two consecutively erupting magnetic structures, and two distinct peaks during the impulsive phase of an M-class flare. Using multi-viewpoint observations of multiple spacecraft, this study shows that the compound eruption originated from two pre-existing sigmoidal magnetic structures lying along the same PIL. Our study suggests

that long-term shearing motion and flux cancellation formed a new low-lying magnetic structure below the existing high-lying structure. The two magnetic structures were separated by 12 Mm in height and were arranged in a double-decker configuration. The instability and fast rise of the high-lying structure was followed by the instability (within 12 minutes) and fast acceleration of the low-lying magnetic structure. The consecutive eruptions of the magnetic structures were observed to have double peaks during the impulsive phase of the eruptions. The two structures later on interacted and appeared as single coronal mass ejection (CME). The dissertation explains the ways the two branches of a double-decker system can erupt from ARs.

6.2 Future Plans

The contributions presented in this dissertation have great potential in further advancing our understanding on the formation of the pre-eruptive magnetic structure, the 3D magnetic topology of ARs before and after the eruption, the triggering mechanism of eruptions, and the prediction of eruptions. I would extend the present work through the following projects:

1. **Extend the work on the 3D time-stacking method:** The dissertation demonstrated that the interaction between opposite magnetic fluxes of non-conjugate pairs is very important in determining the flare productivity of an AR. Shearing motion and magnetic flux cancellation, along the PIL of such interacting regions, produce multiple solar eruptions. The quantification of these processes would be useful in the prediction of solar eruptions. However, quantification of such processes is not always possible due to the inability to separate the interacting regions. The 3D time-stacking data is very useful to understand the general evolution of ARs and isolate the regions where opposite magnetic fluxes are interacting. Also, it is easy to identify the motion of magnetic poles in these data. The 3D time-stacking method can be extended to quantify the motion between the opposite magnetic poles and magnetic flux cancellation.

2. **Using the upcoming observational data to understand the formation of magnetic structures along the PIL:** Measurements of magnetic field above the photosphere are difficult and are rare due to tenuous plasma density. Solar physicists are using photospheric magnetic field to understand the evolution of magnetic structures in the solar corona. The upcoming data from the Daniel K. Inoue Solar Telescope (DKIST) will fill this gap. DKIST is the world's largest solar telescope, with a 4-meter aperture, and can observe the Sun in visible to near-infrared wavelengths. It has five instruments and can observe the Sun nearly simultaneously in multiple wavelengths. Through the selection of magnetically sensitive lines from different solar atmospheric layers, for the first time, the changes in magnetic structures can be tracked from the photosphere to the corona.

3. **Understanding the origin of solar eruptions through the study of homologous eruptions:** Repetitive eruptions from the same local region (homologous eruptions) of an AR are due to continuation of physical processes, such as shearing motion and magnetic flux cancellation, for a long time. The study of such events is useful to understand the formation of pre-eruptive magnetic structures. Using rich observational data sets and modeling results (constrained by observational data like flux-ropes insertion and/or non-linear-force-free-field methods), the study of homologous eruptions would be useful to understand solar eruptions. Such studies would help to identify the dominant physical mechanisms forming eruptive magnetic structures, track the changes in magnetic topology before and after the successive eruptions, and understand how a pre-existing erupting structure loses its stability and starts to erupt.

Bibliography

- Abramenko, V. I. 2005, , 629, 1141, doi: 10.1086/431732
- Amari, T., Luciani, J. F., Aly, J. J., Mikic, Z., & Linker, J. 2003, , 585, 1073, doi: 10.1086/345501
- Amari, T., Luciani, J. F., Mikic, Z., & Linker, J. 2000, , 529, L49, doi: 10.1086/312444
- Antiochos, S. K., DeVore, C. R., & Klimchuk, J. A. 1999, , 510, 485, doi: 10.1086/306563
- Archontis, V., Moreno-Insertis, F., Galsgaard, K., Hood, A., & O'Shea, E. 2004, , 426, 1047, doi: 10.1051/0004-6361:20035934
- Aulanier, G., Török, T., Démoulin, P., & DeLuca, E. E. 2010, , 708, 314, doi: 10.1088/0004-637X/708/1/314
- Awasthi, A. K., Jain, R., Gadhiya, P. D., et al. 2014, , 437, 2249, doi: 10.1093/mnras/stt2032
- Babcock, H. W. 1961, , 133, 572, doi: 10.1086/147060
- Bao, S. D., Zhang, H. Q., Ai, G. X., & Zhang, M. 1999, , 139, 311, doi: 10.1051/aas:1999396
- Bateman, G. 1978, MHD instabilities
- Biesecker, D. A., & Thompson, B. J. 2000, *Journal of Atmospheric and Solar-Terrestrial Physics*, 62, 1449, doi: 10.1016/S1364-6826(00)00085-7
- Borrero, J. M., & Ichimoto, K. 2011, *Living Reviews in Solar Physics*, 8, 4, doi: 10.12942/lrsp-2011-4

- Bumba, V. 1965, in IAU Symposium, Vol. 22, Stellar and Solar Magnetic Fields, ed. R. Lust, 192
- Carmichael, H. 1964, NASA Special Publication, 50, 451
- Carrington, R. C. 1858, , 19, 1, doi: 10.1093/mnras/19.1.1
- Chatterjee, P., & Fan, Y. 2013, , 778, L8, doi: 10.1088/2041-8205/778/1/L8
- Chen, P. F., Innes, D. E., & Solanki, S. K. 2008, , 484, 487, doi: 10.1051/0004-6361:200809544
- Chen, P. F., & Shibata, K. 2000, , 545, 524, doi: 10.1086/317803
- Cheng, X., & Ding, M. D. 2016, , 225, 16, doi: 10.3847/0067-0049/225/1/16
- Cheng, X., Ding, M. D., Zhang, J., et al. 2014, , 789, 93, doi: 10.1088/0004-637X/789/2/93
- Cheng, X., Zhang, J., Liu, Y., & Ding, M. D. 2011, , 732, L25, doi: 10.1088/2041-8205/732/2/L25
- Cheng, X., Zhang, J., Saar, S. H., & Ding, M. D. 2012, , 761, 62, doi: 10.1088/0004-637X/761/1/62
- Chintzoglou, G., Patsourakos, S., & Vourlidis, A. 2015, , 809, 34, doi: 10.1088/0004-637X/809/1/34
- Chintzoglou, G., & Zhang, J. 2013, , 764, L3, doi: 10.1088/2041-8205/764/1/L3
- Chintzoglou, G., Zhang, J., Cheung, M. C. M., & Kazachenko, M. 2019, , 871, 67, doi: 10.3847/1538-4357/aaef30
- Choudhary, D. P., Ambastha, A., & Ai, G. 1998, , 179, 133, doi: 10.1023/A:1005063609450
- Choudhary, D. P., Gosain, S., Gopalswamy, N., et al. 2013, *Advances in Space Research*, 52, 1561, doi: 10.1016/j.asr.2013.07.009

- Demoulin, P., Bagala, L. G., Mandrini, C. H., Henoux, J. C., & Rovira, M. G. 1997, , 325, 305
- Demoulin, P., Henoux, J. C., Priest, E. R., & Mandrini, C. H. 1996, , 308, 643
- DeVore, C. R., & Antiochos, S. K. 2008, , 680, 740, doi: 10.1086/588011
- Dhakal, S. K., Chintzoglou, G., & Zhang, J. 2018, , 860, 35, doi: 10.3847/1538-4357/aac028
- D'Silva, S., & Choudhuri, A. R. 1993, , 272, 621
- Elmhamdi, A., Romano, P., Kordi, A. S., & Al-trabulsy, H. A. 2014, , 289, 2957, doi: 10.1007/s11207-014-0507-9
- Fan, Y. 2001, , 554, L111, doi: 10.1086/320935
- Fan, Y., & Gibson, S. E. 2003, , 589, L105, doi: 10.1086/375834
- Fan, Y., Zweibel, E. G., Linton, M. G., & Fisher, G. H. 1999, , 521, 460, doi: 10.1086/307533
- Fárník, F., Hudson, H., & Watanabe, T. 1996, , 165, 169, doi: 10.1007/BF00149096
- Fárník, F., & Savy, S. K. 1998, , 183, 339, doi: 10.1023/A:1005092927592
- Fletcher, L., Dennis, B. R., Hudson, H. S., et al. 2011, , 159, 19, doi: 10.1007/s11214-010-9701-8
- Forbes, T. G. 2000, , 105, 23153, doi: 10.1029/2000JA000005
- Freeland, S. L., & Handy, B. N. 1998, , 182, 497, doi: 10.1023/A:1005038224881
- Gibson, S. E., & Fan, Y. 2006, , 637, L65, doi: 10.1086/500452
- Gibson, S. E., Fletcher, L., Del Zanna, G., et al. 2002, , 574, 1021, doi: 10.1086/341090
- Gilbert, H. R., Holzer, T. E., Burkepile, J. T., & Hundhausen, A. J. 2000, , 537, 503, doi: 10.1086/309030

- Gopalswamy, N., Mäkelä, P., Akiyama, S., et al. 2013, , 284, 17, doi: 10.1007/s11207-012-0215-2
- Gopalswamy, N., Mäkelä, P., Yashiro, S., et al. 2019, in Journal of Physics Conference Series, Vol. 1332, Journal of Physics Conference Series, 012004
- Gopalswamy, N., Mikić, Z., Maia, D., et al. 2006, , 123, 303, doi: 10.1007/s11214-006-9020-2
- Gopalswamy, N., Yashiro, S., Akiyama, S., & Xie, H. 2017, , 292, 65, doi: 10.1007/s11207-017-1080-9
- Gopalswamy, N., Yashiro, S., Krucker, S., Stenborg, G., & Howard, R. A. 2004, Journal of Geophysical Research (Space Physics), 109, A12105, doi: 10.1029/2004JA010602
- Gopalswamy, N., Yashiro, S., Michalek, G., et al. 2002, , 572, L103, doi: 10.1086/341601
- Gopalswamy, N., Yashiro, S., Michalek, G., et al. 2005, , 32, L12S09, doi: 10.1029/2004GL021639
- Green, L. M., Kliem, B., Török, T., van Driel-Gesztelyi, L., & Attrill, G. D. R. 2007, , 246, 365, doi: 10.1007/s11207-007-9061-z
- Green, L. M., Kliem, B., & Wallace, A. J. 2011, , 526, A2, doi: 10.1051/0004-6361/201015146
- Hale, G. E. 1908, , 28, 315, doi: 10.1086/141602
- Hale, G. E., Ellerman, F., Nicholson, S. B., & Joy, A. H. 1919, , 49, 153, doi: 10.1086/142452
- Harra, L. K., Matthews, S. A., & Culhane, J. L. 2001, , 549, L245, doi: 10.1086/319163
- Harvey, J. W. 1969, PhD thesis, National Solar Observatory
- Harvey, K., & Harvey, J. 1973, , 28, 61, doi: 10.1007/BF00152912

- Hirayama, T. 1974, , 34, 323, doi: 10.1007/BF00153671
- Hoeksema, J. T., Liu, Y., Hayashi, K., et al. 2014, , 289, 3483, doi: 10.1007/s11207-014-0516-8
- Hudson, H. S. 2011, , 158, 5, doi: 10.1007/s11214-010-9721-4
- Inhester, B. 2006, ArXiv Astrophysics e-prints
- Jacobs, C., Roussev, I. I., Lugaz, N., & Poedts, S. 2009, , 695, L171, doi: 10.1088/0004-637X/695/2/L171
- Joshi, B., Veronig, A. M., Lee, J., et al. 2011, , 743, 195, doi: 10.1088/0004-637X/743/2/195
- Klassen, A., Pohjolainen, S., & Klein, K.-L. 2003, , 218, 197, doi: 10.1023/B:SOLA.0000013034.61996.c4
- Kliem, B., & Török, T. 2006, Physical Review Letters, 96, 255002, doi: 10.1103/PhysRevLett.96.255002
- Kliem, B., Török, T., Titov, V. S., et al. 2014, , 792, 107, doi: 10.1088/0004-637X/792/2/107
- Kopp, R. A., & Pneuman, G. W. 1976, , 50, 85, doi: 10.1007/BF00206193
- Krall, K. R., Smith, Jr., J. B., Hagyard, M. J., West, E. A., & Cummings, N. P. 1982, , 79, 59, doi: 10.1007/BF00146973
- Leake, J. E., Linton, M. G., & Antiochos, S. K. 2014, , 787, 46, doi: 10.1088/0004-637X/787/1/46
- Leake, J. E., Linton, M. G., & Török, T. 2013, , 778, 99, doi: 10.1088/0004-637X/778/2/99
- Leka, K. D., & Barnes, G. 2003, , 595, 1296, doi: 10.1086/377512
- . 2007, , 656, 1173, doi: 10.1086/510282

- Leka, K. D., Canfield, R. C., McClymont, A. N., & van Driel-Gesztelyi, L. 1996, , 462, 547, doi: 10.1086/177171
- Leka, K. D., van Driel-Gesztelyi, L., Nitta, N., et al. 1994, , 155, 301, doi: 10.1007/BF00680598
- Lemen, J. R., Title, A. M., Akin, D. J., et al. 2012, , 275, 17, doi: 10.1007/s11207-011-9776-8
- Li, Y., Lynch, B. J., Welsch, B. T., et al. 2010, , 264, 149, doi: 10.1007/s11207-010-9547-y
- Lites, B. W. 2005, , 622, 1275, doi: 10.1086/428080
- Liu, C., Lee, J., Yurchyshyn, V., et al. 2007, , 669, 1372, doi: 10.1086/521644
- Liu, R., Kliem, B., Török, T., et al. 2012, , 756, 59, doi: 10.1088/0004-637X/756/1/59
- Liu, R., Kliem, B., Titov, V. S., et al. 2016, , 818, 148, doi: 10.3847/0004-637X/818/2/148
- Liu, Y., Su, J., Xu, Z., et al. 2009, , 696, L70, doi: 10.1088/0004-637X/696/1/L70
- Liu, Y., Sun, X., Török, T., Titov, V. S., & Leake, J. E. 2017, , 846, L6, doi: 10.3847/2041-8213/aa861e
- Livingston, W. 2002, , 207, 41, doi: 10.1023/A:1015555000456
- López Ariste, A., Aulanier, G., Schmieder, B., & Sainz Dalda, A. 2006, , 456, 725, doi: 10.1051/0004-6361:20064923
- Lynch, B. J., Antiochos, S. K., DeVore, C. R., Luhmann, J. G., & Zurbuchen, T. H. 2008, , 683, 1192, doi: 10.1086/589738
- Metcalf, T. R. 1994, , 155, 235, doi: 10.1007/BF00680593
- Metcalf, T. R., Leka, K. D., Barnes, G., et al. 2006, , 237, 267, doi: 10.1007/s11207-006-0170-x

- Moore, R. L., Sterling, A. C., Hudson, H. S., & Lemen, J. R. 2001, , 552, 833, doi: 10.1086/320559
- Murray, M. J., Hood, A. W., Moreno-Insertis, F., Galsgaard, K., & Archontis, V. 2006, , 460, 909, doi: 10.1051/0004-6361:20065950
- Nitta, N. V., & Hudson, H. S. 2001, , 28, 3801, doi: 10.1029/2001GL013261
- Parker, E. N. 1955, , 121, 491, doi: 10.1086/146010
- . 1996, , 471, 485, doi: 10.1086/177983
- Patty, S. R., & Hagyard, M. J. 1986, , 103, 111, doi: 10.1007/BF00154862
- Pesnell, W. D., Thompson, B. J., & Chamberlin, P. C. 2012, , 275, 3, doi: 10.1007/s11207-011-9841-3
- Polito, V., Del Zanna, G., Valori, G., et al. 2017, , 601, A39, doi: 10.1051/0004-6361/201629703
- Priest, E. R., Hood, A. W., & Anzer, U. 1989, , 344, 1010, doi: 10.1086/167868
- Ribes, J. C., & Nesme-Ribes, E. 1993, , 276, 549
- Romano, P., Elmhamdi, A., Falco, M., et al. 2018, , 852, L10, doi: 10.3847/2041-8213/aaa1df
- Romano, P., Zuccarello, F., Guglielmino, S. L., et al. 2015, , 582, A55, doi: 10.1051/0004-6361/201525887
- Rust, D. M., & Kumar, A. 1996, , 464, L199, doi: 10.1086/310118
- Ryutova, M., & Hagenaar, H. 2007, , 246, 281, doi: 10.1007/s11207-007-0399-z
- Sammis, I., Tang, F., & Zirin, H. 2000, , 540, 583, doi: 10.1086/309303
- Scherrer, P. H., Schou, J., Bush, R. I., et al. 2012, , 275, 207, doi: 10.1007/s11207-011-9834-2

- Schou, J., Scherrer, P. H., Bush, R. I., et al. 2012, , 275, 229, doi: 10.1007/s11207-011-9842-2
- Schrijver, C. J. 2007, , 655, L117, doi: 10.1086/511857
- Schuck, P. W. 2008, , 683, 1134, doi: 10.1086/589434
- Seehafer, N. 1990, , 125, 219, doi: 10.1007/BF00158402
- Shen, Y.-D., Liu, Y., & Liu, R. 2011, *Research in Astronomy and Astrophysics*, 11, 594
- Shi, Z., & Wang, J. 1994, , 149, 105, doi: 10.1007/BF00645181
- Solanki, S. K. 2003, , 11, 153, doi: 10.1007/s00159-003-0018-4
- Song, H. Q., Zhang, J., Cheng, X., et al. 2014, , 784, 48, doi: 10.1088/0004-637X/784/1/48
- Sturrock, P. A. 1966, , 211, 695, doi: 10.1038/211695a0
- Sun, X., Bobra, M. G., Hoeksema, J. T., et al. 2015, , 804, L28, doi: 10.1088/2041-8205/804/2/L28
- Tanaka, K. 1991, , 136, 133, doi: 10.1007/BF00151700
- Tang, F. 1986, , 105, 399, doi: 10.1007/BF00172056
- Tian, H., McIntosh, S. W., Xia, L., He, J., & Wang, X. 2012, , 748, 106, doi: 10.1088/0004-637X/748/2/106
- Tian, L., Liu, Y., & Wang, H. 2003, , 215, 281, doi: 10.1023/A:1025686305225
- Tian, L., Liu, Y., & Wang, J. 2002, , 209, 361, doi: 10.1023/A:1021270202680
- Titov, V. S., Hornig, G., & Démoulin, P. 2002, *Journal of Geophysical Research (Space Physics)*, 107, 1164, doi: 10.1029/2001JA000278
- Toriumi, S., Iida, Y., Kusano, K., Bamba, Y., & Imada, S. 2014, , 289, 3351, doi: 10.1007/s11207-014-0502-1

- Török, T., & Kliem, B. 2005, , 630, L97, doi: 10.1086/462412
- Török, T., Panasenco, O., Titov, V. S., et al. 2011, , 739, L63, doi: 10.1088/2041-8205/739/2/L63
- Török, T., Leake, J. E., Titov, V. S., et al. 2014, , 782, L10, doi: 10.1088/2041-8205/782/1/L10
- Unno, W. 1956, , 8, 108
- van Ballegooijen, A. A. 1982, , 113, 99
- van Ballegooijen, A. A., & Martens, P. C. H. 1989, , 343, 971, doi: 10.1086/167766
- van Driel-Gesztelyi, L., & Green, L. M. 2015, Living Reviews in Solar Physics, 12, 1, doi: 10.1007/lrsp-2015-1
- Vaquero, J. M. 2007, Advances in Space Research, 40, 929, doi: 10.1016/j.asr.2007.01.087
- Vasantharaju, N., Vemareddy, P., Ravindra, B., & Doddamani, V. H. 2018a, , 860, 58, doi: 10.3847/1538-4357/aac272
- . 2018b, , 860, 58, doi: 10.3847/1538-4357/aac272
- Vemareddy, P. 2015, , 806, 245, doi: 10.1088/0004-637X/806/2/245
- . 2017a, , 845, 59, doi: 10.3847/1538-4357/aa7ff4
- . 2017b, , 851, 3, doi: 10.3847/1538-4357/aa9706
- . 2019a, , 486, 4936, doi: 10.1093/mnras/stz1020
- . 2019b, , 872, 182, doi: 10.3847/1538-4357/ab0200
- Vemareddy, P., Venkatakrisnan, P., & Karthikreddy, S. 2015, Research in Astronomy and Astrophysics, 15, 1547, doi: 10.1088/1674-4527/15/9/011

- Wang, Y., & Zhang, J. 2007, , 665, 1428, doi: 10.1086/519765
- Wang, Y. M., & Sheeley, N. R., J. 1989, , 124, 81, doi: 10.1007/BF00146521
- Wheatland, M. S., Sturrock, P. A., & Roumeliotis, G. 2000, , 540, 1150, doi: 10.1086/309355
- Wiegelmann, T. 2004, , 219, 87, doi: 10.1023/B:SOLA.0000021799.39465.36
- Wiegelmann, T., & Inhester, B. 2010, , 516, A107, doi: 10.1051/0004-6361/201014391
- Wiegelmann, T., Inhester, B., & Sakurai, T. 2006, , 233, 215, doi: 10.1007/s11207-006-2092-z
- Wiegelmann, T., & Sakurai, T. 2012, Living Reviews in Solar Physics, 9, 5, doi: 10.12942/lrsp-2012-5
- Woods, T. N., Eparvier, F. G., Hock, R., et al. 2012, , 275, 115, doi: 10.1007/s11207-009-9487-6
- Yang, Y.-H., Hsieh, M.-S., Yu, H.-S., & Chen, P. F. 2017, , 834, 150, doi: 10.3847/1538-4357/834/2/150
- Zhang, H., Ai, G., Wang, H., Zirin, H., & Patterson, A. 1992, , 140, 307, doi: 10.1007/BF00146315
- Zhang, J., Cheng, X., & Ding, M.-D. 2012, Nature Communications, 3, 747, doi: 10.1038/ncomms1753
- Zhang, J., & Dere, K. P. 2006, , 649, 1100, doi: 10.1086/506903
- Zhang, J., Dere, K. P., Howard, R. A., Kundu, M. R., & White, S. M. 2001, , 559, 452, doi: 10.1086/322405
- Zhang, J., & Wang, J. 2002, , 566, L117, doi: 10.1086/339660
- Zhang, J., Wang, Y., & Liu, Y. 2010, , 723, 1006, doi: 10.1088/0004-637X/723/2/1006

Zhang, Q. M., Ning, Z. J., Guo, Y., et al. 2015, , 805, 4, doi: 10.1088/0004-637X/805/1/4

Zhou, G. P., Zhang, J., & Wang, J. X. 2016, , 823, L19, doi: 10.3847/2041-8205/823/1/L19

Zhu, C., Liu, R., Alexander, D., Sun, X., & McAteer, R. T. J. 2015, , 813, 60, doi: 10.1088/0004-637X/813/1/60

Zirin, H. 1970, , 14, 328, doi: 10.1007/BF00221318

Zirin, H., & Wang, H. 1993, , 363, 426, doi: 10.1038/363426a0

Zwaan, C. 1987, , 25, 83, doi: 10.1146/annurev.aa.25.090187.000503

Curriculum Vitae

Suman Dhakal was born in Dhading, Nepal. He completed his Bachelor degree in Physics in 2007 from Birendra Multiple Campus, Bhartpur, Nepal. In 2013, he completed his Master degree in Physics from Tribhuvan University, Kathmandu, Nepal. In Fall 2013, he enrolled in the Physics and Astronomy graduate program at George Mason University, Fairfax, Virginia. Beginning Fall 2013 he has worked under the supervision of Dr. Jie Zhang in the field of Solar Physics.